Rowan University

Rowan Digital Works

TOWARDS A PRACTICAL METHOD FOR MONITORING KINETIC PROCESSES IN POLYMERS WITH LOW-FREQUENCY RAMAN SPECTROSCOPY

Robert Vito Chimenti
Rowan University

Follow this and additional works at: https://rdw.rowan.edu/etd

Part of the Materials Science and Engineering Commons, and the Physics Commons

TOWARDS A PRACTICAL METHOD FOR MONITORING KINETIC PROCESSES IN POLYMERS WITH LOW-FREQUENCY RAMAN SPECTROSCOPY

by

Robert Vito Chimenti

A Dissertation

Submitted to the
Department of Physics and Astronomy
College of Science and Mathematics
In partial fulfillment of the requirement
For the degree of
Doctor of Philosophy
at
Rowan University
March 26, 2024

Dissertation Chair: Samuel E. Lofland, Ph.D., Professor, Department of Physics and Astronomy

Committee Members:
Joseph F. Stanzione, III, Ph.D., Professor, Department of Chemical Engineering
Vince Z. Beachley, Ph.D., Associate Professor, Department of Biomedical Engineering

Abstract

Robert Vito Chimenti
TOWARDS A PRACTICAL METHOD FOR MONITORING KINETIC PROCESSES
IN POLYMERS WITH LOW-FREQUENCY RAMAN SPECTROSCOPY
2023-2024
Samuel E. Lofland, Ph.D.
Doctor of Philosophy in Materials Science and Engineering

Unlike liquids and crystalline solids, glassy materials exist in a constant state of structural nonequilibrium. Therefore, a comprehensive understanding of material kinetics is critical for understanding the structure-property-processing relationships of polymeric materials. Amorphous materials universally display low-frequency Raman features related to the phonon density of states resulting in a broad disorder band for Raman shifts below 100 cm^{-1}, which is related to the conformational entropy and the modulus. This disorder band is dominated by the Boson peak, a feature due to phonon scattering because of disorder and can be related to the transverse sound velocity of the material, and a well-defined shoulder due to a van Hove singularity. Quasi-elastic Rayleigh scattering also contributes to the signal, particularly in liquid-phase materials. We have demonstrated that we can measure both glass transition and polymerization kinetics by normalizing the disorder band to its shoulder and monitoring its evolution as a function of time and temperature. We also demonstrate a relationship between the chemical and structural kinetics, which appears to relate to the softness of the material, which we verify via rheological analysis. Low-frequency Raman spectroscopy is, therefore, a promising technique for thermo-structural analysis of polymers. Not only is it chemically agnostic and contactless, but it requires neither intensity calibration nor multivariate analysis.

Table of Contents

Table of Contents (Continued)

List of Figures

List of Figures (Continued)

Figure   Page

List of Tables

Chapter 1

Introduction

1.1 Motivation and Background

Both material and chemical kinetics are critical to understanding the structure-property-processing relationships in polymer science and engineering. While there are a wide range of kinetic processes of interest to polymer science, the glass transition and the extent of polymerization are perhaps the two most important for determining material properties and therefore key to optimizing the processing conditions. Today's advanced manufacturing processes not only require advanced knowledge of these parameters but can also greatly benefit from *in situ* monitoring during production [1]. As will be described in detail in Section 1.2.1, the glass transition temperature T_g not only dictates the processing temperature required for molding and extruding, but it also relates to mechanical/viscoelastic properties at typical working temperatures (e.g. room temperature). Similarly, both the rate of polymerization R_p and degree of cure α, also referred to as conversion, are essential for understanding both the optimal processing conditions for cure molding and 3D printing (see Section 1.2.2). Furthermore, as we will show in Section 1.2.3, α also directly relates to T_g.

Differential scanning calorimetry (DSC) has historically been the primary analytical tool used for quantitating both T_g and α of polymers [2-10]. DSC measures heat flow as a function of time and temperature by comparing the sample and reference temperature when heated at the same rate. Since specific heat is directly proportional to heat flow and change in enthalpy is related to the area under the time dependent heat flow curve, DSC is a powerful tool for determining both thermodynamic properties and kinetic

processes [11]. However, DSC is incapable of performing *in situ* analysis since it requires a relatively small sample size ~10-15 mg to be placed into a sealed crucible which is in turn placed into the device's oven. Additionally, as we will discuss in Section 1.2.2, kinetic studies with DSC often rely upon assumptions regarding the ultimate heat of reaction, which is not always straightforward to determine.

Another common approach to determine polymer kinetics is by monitoring changes in viscoelastic properties. For bulk samples this is most often done via dynamic mechanical analysis (DMA), which measures the complex modulus as the material response to a sinusoidally varying stress as a function of temperature. The in-phase component is known as the storage modulus E' and represents the elastic or "solid-like" behavior of the material. By contrast, the out-of-phase response represents the viscous or "liquid-like" behavior of the material and is referred to as the loss modulus E''. For polymer powders, liquids, or films parallel plate rheology can be used to measure the in-phase and out-of-phase shear moduli, G' and G'', respectively, as well as viscosity η. While these methods provide the most direct measurement of the glass transitions, there is no universally accepted definition of the exact value of T_g based on the moduli or η. Additionally, neither of these methodologies is suitable for *in situ* analysis.

Vibrational spectroscopy is often used to measure bond concentration as well as steric effects in a molecule. The underlying physics behind these phenomena will be discussed in great detail in later sections, but it is important to point out that this methodology can allow for a direct measurement of α as well as indirect measurement of T_g. The most commonly used vibrational spectroscopy technique in polymer analysis is attenuated total internal reflection-based Fourier transform infrared (ATR-FTIR)

spectroscopy. Raman spectroscopy also probes the vibrational modes of the molecule and as a laser scattering technique it is ideal for *in situ* analysis. It should be noted that infrared absorbance spectroscopy can also be performed in transmission and diffuse reflectance mode making it more amiable for *in situ* and process measurements. However, neither of these collection methods are as sensitive as ATR and they still require the use of either interferometric spectral analysis or tunable quantum cascade laser sources which exponentially increase the cost and complexity of the system.

In this dissertation we present a novel alternative approach to measure kinetic processes in polymers using the low-frequency region of the Raman spectra. Unlike traditional vibrational spectroscopy which probes the "chemical fingerprint" of a molecule of interest, vibrations in the low-frequency region are a direct result of phonon modes related to the overall structure of the material. Since the phonon population and the density of states in an amorphous material relate to its conformational entropy, low-frequency Raman provides a chemically agnostic measure of changes in the overall disorder of the material. Additionally, the occupancy probability of a given vibrational state increases exponentially as the frequency decreases, and the Raman scattering efficiency is inversely proportional to the vibrational frequency. The combination of these two factors results in far greater signal strength in the low-frequency (structural) region compared to the traditional chemical fingerprint region.

Section 1.2 provides additional background on the kinetic processes which were studied in this dissertation. A detailed review of both the underlying physics and instrumentation requirements of Raman spectroscopy are presented in Section 1.3.

Section 1.4 describes the project strategy and scope in more detail and provides an overview of this dissertation.

1.2 Kinetic Processes Studied

1.2.1 Glass Transition

The melting temperature T_m of crystalline materials results from a clearly defined phase transition detectable by volumetric, enthalpic, and entropic step discontinuities. However, since amorphous solids have no defined long-range structural order, there is no clearly defined T_m [12]. Instead, amorphous solids go through a gradual liquid $\rightleftharpoons$ glass transition whereby, the material slowly becomes less "glassy" and more "rubbery" as the temperature increases. Therefore, the glass transition temperature T_g is instead defined by a change in the slope of volume, enthalpy, or entropy as a function of temperature characteristic of a second-order thermodynamic phase transition [12, 13].

A useful framework for understanding the thermodynamic basis for the terms first- and second-order transition is with reference to the Gibb's free energy relationship

$$G = H - TS = U + pV - TS \tag{1}$$

where G is the Gibb's free energy, H the enthalpy, T the temperature, U the internal energy, p the pressure, and V the volume. Therefore, S and H can be expressed as the first derivative of G and constant p, and V can be expressed as the first derivative of G at constant T. This first derivative relationship with G is why V, H, and S are referred to as first-order thermodynamic properties, and that phase transitions which result in a discontinuity in these properties are known as first-order phase transitions. Properties such as the isobaric heat capacity C_p,

$$C_p = \left(\frac{\partial H}{\partial T}\right)_p = T\left(\frac{\partial S}{\partial T}\right)_p = -T\left(\frac{\partial^2 G}{\partial T^2}\right)_p, \tag{2}$$

the isobaric coefficient of thermal expansion β,

$$\beta = \frac{1}{V}\left(\frac{\partial V}{\partial T}\right)_p = \frac{1}{V}\frac{\partial}{\partial T}\left[\left(\frac{\partial G}{\partial p}\right)_T\right]_p, \tag{3}$$

and the isothermal compressibility κ,

$$\kappa = -\frac{1}{V}\left(\frac{\partial V}{\partial p}\right)_T = -\frac{1}{V}\left(\frac{\partial^2 G}{\partial p^2}\right)_T, \tag{4}$$

are referred to as second-order thermodynamic properties since they are all defined in

terms of a first derivative of V, H, and S, and therefore the second derivative of G.

Because of this differential relationship between first- and second-order thermodynamic

properties, the slope change in V, H, and S at T_g manifests as a discontinuity in C_p, β, and

κ, hence the nomenclature referring to glass transition as a second-order phase change

[13]. Figure 1 shows a schematic representation of both melt and glass transition in terms

of first- and second-order thermodynamic properties.
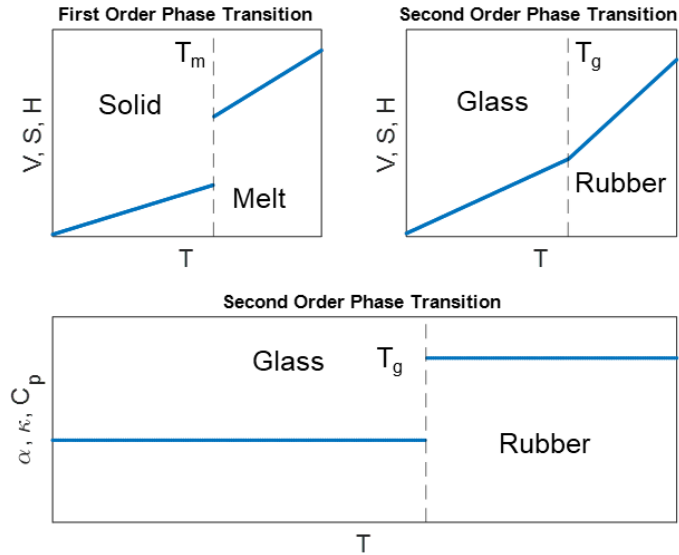
Figure 1. Schematic representation of first- and second-order phase transitions.

Historically the term glass was used only to refer to an amorphous material which is produced through a melt-quenching [12]. While that restrictive nomenclature is typically not adhered to in modern day, it does provide a useful mental framework to consider the glass transition of a material as a rate-dependent phenomenon. In fact, any material can form a glass if cooled from the melt phase fast enough to lock the atoms or molecules into a configuration with a local energy minimum, denying the material sufficient time to find the global minimum in energy and crystallize [12]. This rate dependency clearly demonstrates that glass transition has both a thermodynamic and a kinetic interpretation, or as John Mauro wrote, "it is more accurate to think of the glass transition as a kinetic transition with thermodynamic consequences, rather than a thermodynamic transition [14]." For example, the rate dependency of the phenomena leads to large variations in reported T_g values depending on experimental conditions [11]. Additionally, while the thermodynamic definition of T_g assumes an instantaneous slope

change in V, H, and S, the material kinetics dictate a far more gradual gradient in the slope during the glass transition, adding ambiguity in defining the exact value of T_g [14]. Lastly, not only do the current measurement conditions (e.g. temperature ramp rate) factor into the T_g, so do the conditions upon which the material has been previously processed, known as its "thermal history [11]."

While the kinetic nature of glass transition is conceptually straightforward, its implications can often lead to confusion since the typical nomenclature used to describe the process originates from the thermodynamic interpretation. One such example of this confusing nomenclature is the adoption of an alternative definition of T_g in the glass industry – the temperature at which the viscosity η is equal to 10^{12} Pa·s [14]. This terminology arises from the fact that from a practical perspective that this is the temperature at which the glass is considered to be fully annealed and can no longer be bent, shaped, or flowed. While this terminology is useful for glass processing, it does not change the fact that the measured slope (or step) change in first- (or second-) order thermodynamic properties is highly variable. Therefore, in the glass industry the term fictive temperature T_f is introduced to represent the temperature at which there is a kink in the slope of V, H, and S [14]. Throughout the bulk of this dissertation we will be sticking with the thermodynamic definition of T_g since it is the predominantly used nomenclature in polymer science and engineering. However, for the remainder of this section we will temporarily use glass industry notation for T_g and T_f, as it makes it slightly easier to examine the kinetic behavior of a material through the glass transition region primarily because most of the formalization of glass transition kinetics was originally set forth in service of the glass industry.

As a means of characterizing the kinetics during glass transition, Austen Angell proposed the concept of liquid fragility as a measure of how quickly a material transitions between liquid ⇌ glass [15]. In this formulation, "strong" liquids exhibit a small change in intrinsic properties as they transition to the glassy phase, whereby a "fragile" material exbibits a large change therefore providing a measure of how sharp the kink in V, H, and S will be through the glass transition. The fragility index m of a liquid is defined as [14]

$$m \equiv \frac{\partial \log_{10} \eta}{\partial (T_g/T)}\bigg|_{T=T_g}. \tag{5}$$

Inorganic glasses such as silica tend to behave as strong liquids with values of m as low as 20, but as the complexity of the molecular structure increases so too does the fragility [16]. Polymers commonly have values of m over 100 and can approach values of 200 at higher molecular weights; for example Dalle-Ferrier et $al.$ reported that as the molecular weight of polystyrene was increased from 580 g/mol to 5,100 g/mol the m increased from 68 to 124 [16].
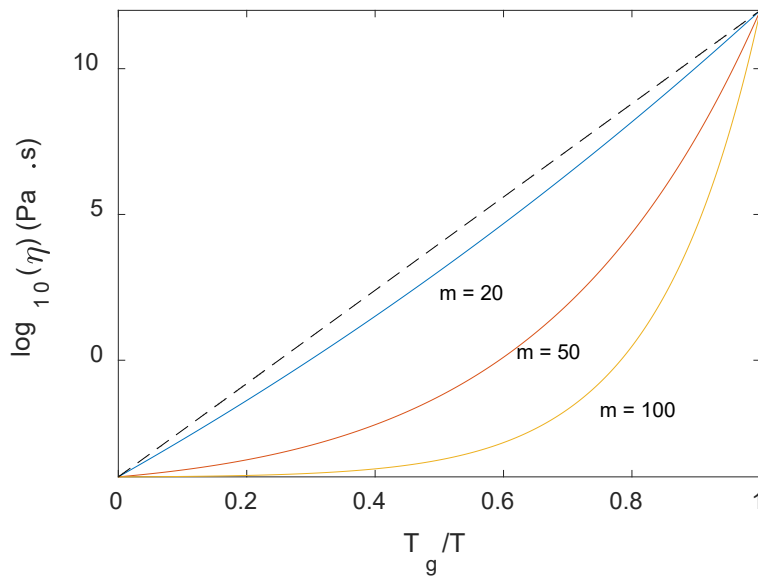
Figure 2. Schematic representation of an Angell diagram adapted from [17].

8

Figure 2 shows a representative Angell diagram ($\log_{10} \eta$ vs $\frac{T_g}{T}$) for $m = 20, 50,$ and 100, which was generated from the Mauro-Yue-Ellison-Gupta-Allan (MYEGA) equation for viscosity:

$$\log_{10} \eta = \log_{10} \eta_\infty + \frac{K}{T} e^{\frac{C}{T}}. \tag{6}$$

where η_∞ is the infinite temperature limit of viscosity and K and C are fitting parameters [14]. For Figure 2 η_∞ was set to 10^{-4} Pa·s and $\eta(T_g)$ was defined as 10^{12} Pa·s allowing for Equation 6 to be re-written as [14]

$$\log_{10} \eta = 16 \frac{T_g}{T} e^{\left[\left(\frac{m}{16}-1\right)\left(\frac{T_g}{T}-1\right)\right]} - 4. \tag{7}$$

It is important to note that the MYEGA equation is only applicable in the liquid phase where the system is in thermal equilibrium. To expand this model into the nonequilibrium viscosity η_{ne} of the glass phase one can use the Mauro-Allan-Potuzak (MAP) model which can be expressed as

$$\log_{10} \eta_{ne} = A + \frac{\Delta H}{k_B T \ln 10} - \frac{S_f}{k_B \ln 10} e^{-\frac{T_g}{T_f}\left(\frac{m}{12-\log_{10} \eta_\infty}-1\right)} \tag{8}$$

where ΔH is the energy barrier for the glass transition, S_f the entropy of the liquid at T_f, and k_B Boltzmann's constant while A relates to η_∞ as $\frac{1}{T} \to 0$ and $\frac{T_g}{T_f} \to 0$ [14]. The MAP model clearly demonstrates that glass transition has both an Arrhenius-like component dependent on T as well as a component which is independent of T but highly dependent on the entropy of the liquid at the time the glass was formed. The final term in Equation 8 clearly demonstrates the effects of both the thermal history showing the dependence on the number of possible states as the glass was formed as well as dependence on m which is itself a cooling/heating rate dependent parameter.

Both the effects of thermal history and heating/cooling rate can be clearly seen in Figure 3 which shows the heat flow ($\propto C_p$) from 0 to 220 °C for 210,000 g/mol molecular weight atactic polystyrene (CAS# 9003-53-6, Scientific Polymer Products, Inc) at 1 °C/min and 10 °C/min heating/cooling rates. The measurements were conducted under nitrogen with a 50 mL/min flow rate with 5−10 mg samples sealed in aluminum pans with hermetic lids with a TA Instruments Discovery Series DSC 2500. The thermograms were smoothed with a Gaussian window function in MATLAB. In both cases the samples were analyzed with a heat-cool-heat method, which are represented by the blue, red, and yellow thermograms respectively in Figure 3. From these results, it is clear that the relatively high fragility of the sample results in a fairly shallow "step discontinuity" at T_g (or T_f depending on nomenclature) in all six measurements, strongly varying with heating rate. Additionally, there is a large variation in between the first and the second heating ramps for each measurement. This is because the act of heating and cooling the sample "erases" the previous thermal history imparting a new "known" thermal history.
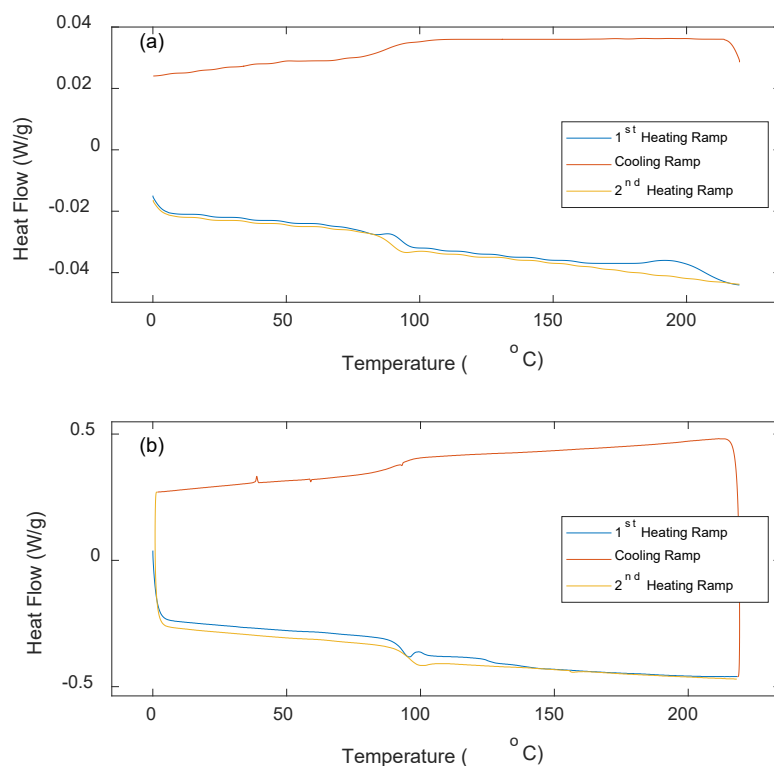
Figure 3. DSC thermogram of polystyrene measured at temperature ramp rates of (a) 1 °C/min and (b) 10 °C/min.

1.2.2 Polymerization

Polymerization reactions can be roughly sorted into two main categories – step- and chain-growth. Step-growth polymerization, also referred to as condensation polymerization, is a parallel process where monomers and chains react with each other, simultaneously forming longer and longer molecules [13]. Whereas chain-growth polymerization, also referred to as addition polymerization, is a series process initiated by the presence of a free radical, anion, or cation breaking a double bond within the monomer and forcing a chain reaction [13]. While the chemical pathways under which

11

materials polymerize are rather diverse, one factor they all have in common is a repeat

reaction consuming one or more functional groups in the process.
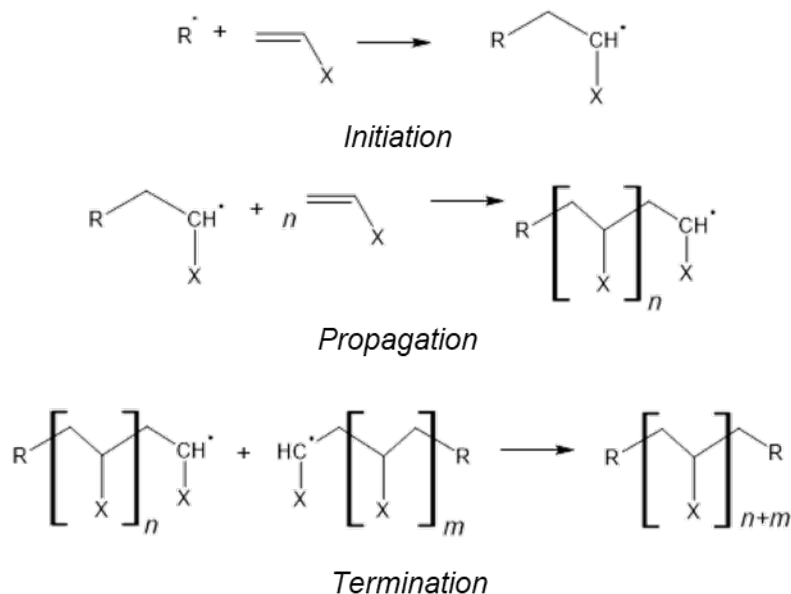
Figure 4. Schematic representation of addition polymerization, adapted from [13].

Figure 4 shows a simplified schematic diagram of a polymerization process

whereby an alkene (C=C) functional group is systematically converted to an aliphatic

chain (-C-C-) through a free radical chain-growth reaction. After the initial free radical is

generated, it then triggers the breaking of the π-bond between the two carbon atoms,

forming a more energetically favorable σ-bond. This in return creates a new free radical

and the process repeats forming a longer and longer chain until either terminating with

another chain (bimolecular termination) or being trapped due to vitrification into the

glassy state (unimolecular termination). While greatly simplified this monofunctional

polymerization example illustrates that we can quantitate α for any polymerization

reaction by ratioing the number of reacted functional groups to the number of initial functional groups.

Vibrational spectroscopy is the most direct way to measure α since the bond concentration is directly proportional to the infrared (IR) absorbance and the Raman scattering intensity (see Section 1.3 for more details). This is typically accomplished by first normalizing the spectra to a reference band associated with an unreactive functional group I_{ref}, and then measuring the change in absorbance or scattering intensity of the reactive band of interest I_{var} with the following relationship [18, 19]:

$$\alpha = 1 - \frac{\left(\frac{I_{var}}{I_{ref}}\right)_{reacted}}{\left(\frac{I_{var}}{I_{ref}}\right)_{unreacted}}. \tag{9}$$

A common alternative methodology is to measure the heat released $H^*(t)$ during the reaction and ratio it with a known ultimate heat of reaction for a fully reacted resin H_u [20]

$$\alpha = \frac{H^*(t)}{H_u}. \tag{10}$$

While this methodology can be advantageous in some circumstances, it often overpredicts the ultimate conversion α_u due to ambiguities in determining H_u because 100% conversion is rarely achieved in practice.

In addition to the linear polymerization process shown in Figure 4, crosslinking can also occur between polymer chains forming a covalently bound polymer network. The earliest known application of polymer crosslinking was the vulcanization of polyisoprene (natural rubber) by Charles Goodyear in 1839 [21]. This was accomplished by combining polyisoprene and cyclooctasulfur and heating it to ~150 °C with white lead

as a catalyst. This caused the sulfur rings to cleave and bond with some of the double-bond carbon atoms within the polymer backbone, resulting in the formation of a single "infinitely large" molecule spanning the entire bulk of the material. While using additional crosslinking agents to chemically connect linear polymer chains is still used today, it is also common to utilize individual monomers containing more than one reactive functional group to achieve crosslinking during the initial polymerization process itself. For example, bifunctional monomers such as triethylene glycol dimethacrylate (TEGDMA) and poly(ethylene glycol) diglycidyl ether (PEGDE) are both commonly used in high performance resin formulations, and both bi- and trifunctional amines are commonly used as curing agents in two-part epoxies.

When conceptualizing multifunctional monomer polymerization, it is often advantageous to use a random-bond percolation model, as shown schematically in Figure 5 for two dimensions. Using the two-dimensional Bethe lattice model one can show that the percolation threshold α_t is inversely proportional to $f - 1$ where f is the monomer functionality [22]. As shown in Figure 5, α_t corresponds to the point at which the very first polymer chain has grown to a sufficient length as to span the entire material as a single molecule. Once α_t has been reached the material is no longer able to freely flow, and as such this is known as the onset of gelation or simply as the gel point [22]. While there are no exact solutions for α_t for non-Bethe lattice systems (e.g. three dimensions), this formulation is quite useful for gaining an intuitive understanding of polymer crosslinking and gelation. Carothers theory of gelation attempts to present a generalized approximation in three dimensions by defining $\alpha_t = \frac{2}{f_{av}}$ where f_{av} is the number averaged functionality, but this often leads to over predictions of α_t [23].
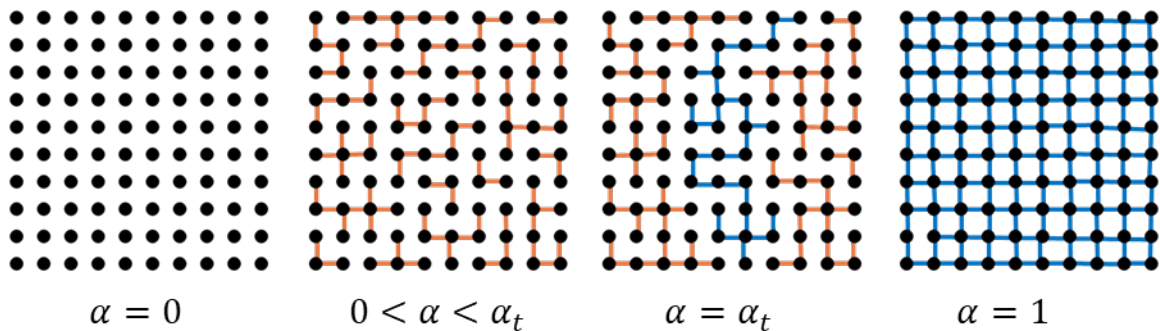
Figure 5. Percolation model of gelation, adapted from [22].

Several numerical models have been developed for percolation in d dimensions, such as the Fisher exponent [22]. However, since α_t is fairly easy to experimentally measure, these first-principles predictive models are of limited utility, providing little insight beyond the functionality dependence already illustrated by the Bethe lattice model and Carothers theory. The most commonly accepted experimental method for determining α_t is the Winter-Chambon criterion which assumes that G' and G'' are equal at the gel point [24]. While this has been shown as equivalent to the percolation threshold definition for rheologically simple resins, this fails to predict the gel point for resin formulations containing filling agents such as fumed silica since the storage modulus is already greater than the loss modulus prior to polymerization [25]. An example of this effect is highlighted in Chapter 4. Several alternative rheological methods for determining α_t have been explored such as detecting a sudden increase in G' [20, 26] or critical strain rate [25].

1.2.3 Impact of T_g and α on Material Properties

As previously discussed, no single value has more of an impact on the overall material properties of a polymer than T_g; however, the impact of α should not be understated either. In fact, all polymers can be characterized into one of three categories depending on T_g and crosslinking – thermoplastics, elastomers, and thermosets. Thermoplastics are linear chain polymers (not crosslinked) which are brittle at low temperatures, plastically deform at moderate temperatures, and become rubbery above T_g. It is important to note that while most thermoplastics are amorphous, they can in some cases form semicrystalline structures consisting of crystal lamella embedded in an amorphous matrix. Two common examples of thermoplastic materials are polystyrene and polylactic acid (PLA), having T_g values of ~90 ºC and ~60 ºC respectively. This makes them easily processable at moderately elevated temperatures but mechanically stable at room temperature.

Both elastomers and thermosets are categories of crosslinked polymers which are differentiated primarily based on their T_g and degree of crosslinking. Elastomers have a low degree of crosslinking and low T_g values, making them rubbery at room temperature while simultaneously allowing them to be stretched without plastic deformation. Thermosets on the other hand have an extremely high degree of crosslinking and a correspondingly high T_g, providing high structural strength but making them relatively brittle. Unlike thermoplastics, neither elastomers nor thermosets can form crystal lamella due to the lack of polymer chain mobility of the crosslinked network. Figure 6 shows a schematic representation of modulus as a function of temperature illustrating the

differences between thermoplastics (linear chain polymers) and elastomers and thermosets (crosslinked polymers).
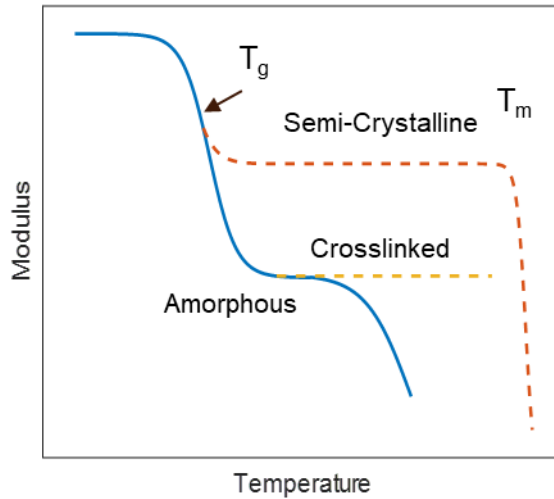
Figure 6. Schematic representation of modulus as a function of temperature for various types of polymers.

Embedded in the definitions of elastomers and thermosets is an implicit relationship between α and T_g since a high crosslink density necessitates a higher α. Ivankovic *et al.* clearly demonstrated this fact by measuring $T_g(\alpha)$ for an epoxy/anhydride system and showing that it could be modeled as a second-order polynomial where the y intercept T_{g0} is the T_g of the uncured resin [27]. In the same study they also developed a chemorheological model showing that the viscosity of the resin was not only dependent on T_g as shown in the MAP model (Equation 8) but also dependent on α and α_t,

$$\eta(T, \alpha) = \eta_g \left(\frac{\alpha_t}{\alpha_t - \alpha}\right)^n e^{-\frac{C_1(T-T_{g0})}{C_2+T+T_{g0}}} \tag{11}$$

where η_g is the viscosity at T_g and C_1, C_2, and n are experimentally determined fitting factors [27]. While Equation 11 is only valid for the isothermal viscosity, as it diverges to infinity at α_t, it clearly demonstrates the importance of both glass transition and polymerization on material properties.

1.3 Fundamentals of Raman Spectroscopy

The inelastic scattering of light by a molecule was first demonstrated by Raman and Krishnan in 1928 [28, 29]. This discovery was immediately recognized as a major achievement in physics, earning C.V. Raman the 1930 Nobel prize in physics. During the award ceremony Pleijel, the chairman of the Nobel committee for physics, was quoted saying "… the Raman effect has already yielded important results concerning the chemical constitution of substances; and it is to foresee that the extremely valuable tool that the Raman effect has placed in our hands will in the immediate future bring with it a deepening of our knowledge of the structure of matter [30]." However, it was not until the invention of the laser in 1960 by Theodore Maiman [31] that the Raman effect could be of any practical use for materials characterization.

Since the Raman effect manifests as a change in photon energy and hence a frequency shift, having precise control of the excitation wavelength is critical for accurate quantitation [32]. Prior to the 1960s, Raman spectra were recorded with mercury lamps and prisms, which made it impractical for most applications, aside from basic physics research. However, only three years after Maiman first demonstrated the laser, PerkinElmer announced the release of the first "laser Raman spectrometer" at the 1964

Ohio State University International Symposium on Molecular Spectroscopy [33]. Over the past 60 years since that announcement, Raman spectroscopy has evolved into an invaluable analytical tool living up to the potential laid out in Pleijel's 1930 speech.

In the following sections we will provide a brief overview of the Raman effect. Section 1.3.1 will provide a semi-classical overview of Raman scattering by analyzing variations in polarizability during dipolar radiation. Section 1.3.2 expands this analysis to bulk vibrational modes by looking at photon-phonon interactions, which are the dominant contributors to low-frequency Raman spectra. Section 1.3.3 will provide an overview of the instrumentation requirements, with a particular focus on aspects critical to the work in this dissertation. It should be noted that the following sections are intended to provide a conceptual framework for the work of this dissertation and are not intended as a comprehensive review of Raman spectroscopy. Lewis and Edwards [34] and Weber and Merlin [35] both provide a far more detailed overview of the subject.

1.3.1 Semi-Classical Model

The Raman effect can be described through both a quantum and classical interpretation. In the quantum interpretation, one can take a particle-based approach analogous to the Compton effect. From this perspective, when a photon collides with a molecule, a portion of the photon's energy is transferred to molecular vibrations or rotation causing the scattered photon to shift to a lower energy or longer wavelength. The decrease in energy of the scatter photon is known as a Stokes shift. Alternatively, if a molecule is already in an excited vibrational or rotational state, energy can be transferred to the scattered photon resulting in a shift to a shorter wavelength, known as an anti-Stokes shift. One can understand the quantum interpretation more generally in terms of

annihilation and creation operators. In the case of Stokes-shifted Raman scattering, the initial photon is annihilated upon impact, creating a photon and phonon whose combined energy is equal to that of the original photon. For anti-Stokes Raman scattering, both the incident photon and a phonon are annihilated, creating a new photon with their combined energy. In the classical interpretation, Raman scattering can be viewed as a nonlinear optical phenomenon resulting from perturbations in dipolar radiation due to changes in the polarizability α of a molecule. This concept can be generalized macroscopically as changes in the electric susceptibility χ_{ij}. When combined with group theory formulations, this simple phenomenological approach can be used to derive a set of Raman tensors R_{ij} which can be used to relate the structure of the material to the polarization dependence of the Raman scatter.

It should be noted throughout this dissertation that α will be used predominantly to represent polymerization extent of cure, but to maintain consistency with traditional nomenclature it will be used exclusively in this section to represent polarizability.

1.3.1.1 Diatomic Harmonic Oscillator. To gain insight into the vibrational modes of a molecule, we start by modeling a diatomic harmonic oscillator as two masses m_1 and m_2, representing the covalent bond as a spring with constant K (see Figure 7). Using Hooke's law, we can then model this system as

$$\frac{m_1 m_2}{m_1 + m_2}\left(\frac{d^2 x_1}{dt^2} + \frac{d^2 x_2}{dt^2}\right) = -K(x_1 + x_2) \tag{12}$$

where x_1 and x_2 are the magnitudes of the displacement vectors for the two atoms. By defining the total displacement vector $\vec{q} = \vec{x}_1 + \vec{x}_2$ and the reduced mass $M = \frac{m_1 m_2}{m_1 + m_2}$ Equation 12 can be rewritten as

$$\frac{d^2q}{dt^2} - \frac{K}{M}q = 0, \tag{13}$$

and solved to find that $q = q_0 \cos(2\pi\nu_m t)$ where, q_0 is the displacement amplitude and $\nu_m = \frac{1}{2\pi}\sqrt{\frac{K}{M}}$ is the vibrational frequency of the molecule.
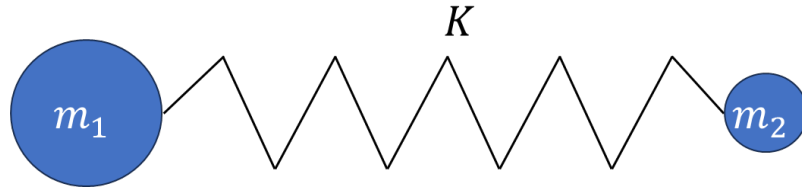
Figure 7. Schematic representation of diatomic molecule as two masses on a spring.

We can also use this model to show that the potential energy U is a parabolic function of q,

$$U = -\int \vec{F} \cdot d\vec{q} = \frac{1}{2}Kq^2 \tag{14}$$

where $\vec{F}$ is the molecular restoring force. This simple harmonic oscillator model can be easily quantized by substituting Equation 14 into the Schrödinger equation,

$$-\frac{h}{4\pi M}\frac{d^2\Psi}{dq^2} + \left(\frac{Kq^2}{2} - E\right)\Psi = 0, \tag{15}$$

where h is Plank's constant, Ψ the wavefunction, and E the energy. Solving for E under the condition that $\Psi \to 0$ as $q \to \pm\infty$ results in

$$E_v = \left(v + \frac{1}{2}\right)h\nu_m \tag{16}$$

where v is the vibrational quantum number [36].

This simple harmonic model has profound implications. It demonstrates that a molecule can only vibrate at discrete frequencies which are directly proportional to the bond strength and inversely proportional to the masses of the two atoms. However, it has one major flaw which limits its applicability to small values of v near the bottom of the potential well. The harmonic potential derived in Equation 14 assumes that $\vec{q}$ can range in value from 0 to ∞, when in reality the molecule can only be stretched so far before the bond will break, causing dissociation of the two atoms. A more accurate representation of the anharmonic potential was developed by Morse [37],

$$U = D_e\left(1 - e^{-\xi(r-r_e)}\right)^2 \tag{17}$$

where r is the instantaneous distance between the two atoms, r_e the equilibrium distance between the two atoms, D_e the dissociation energy, and $\xi = \sqrt{\frac{K}{2D_e}}$ which determines the width of the potential well. Substituting the Morse potential into the Schrödinger equation and solving for E results in

$$E_v = \left(v + \frac{1}{2}\right)h\nu_m - x_m\left(v + \frac{1}{2}\right)^2 h\nu_m \tag{18}$$

where x_m is the Morse anharmonicity constant [37]. Equation 18 more accurately models the observed phenomena whereby vibrational energy level spacing decrease as v increases (see Figure 8).
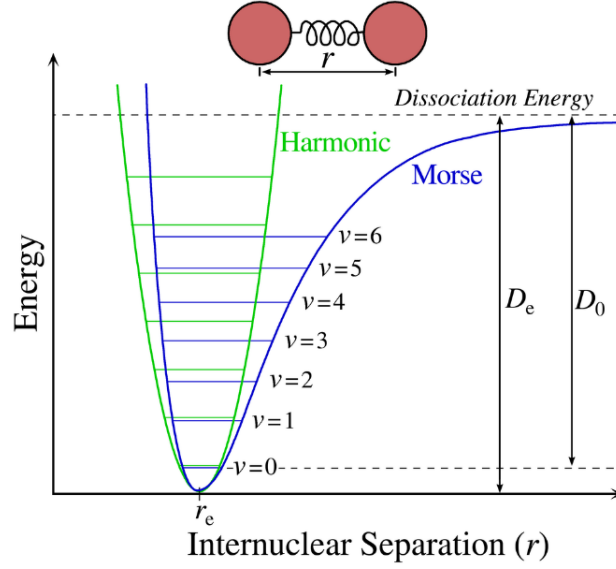
Figure 8. Vibrational energy level diagram for both harmonic (green) and anharmonic (blue) potentials. Reproduced in accordance with creative commons license agreement CC BY-SA 3.0. [38]

1.3.1.2 Scattering as Dipolar Radiation. The intensity of the radiation I of dipolar radiation is typically expressed by the time-averaged Poynting vector $\langle \vec{S} \rangle$ [39] given by

$$\langle \vec{S} \rangle = \left[\frac{\pi^2 p_0^2 \nu^4 \mu_0}{2c} \left(\frac{\sin \theta}{r} \right)^2 \right] \hat{r} \tag{19}$$

where p_0 is the magnitude of the dipole moment $\vec{p}$, ν the frequency of the dipole oscillation, c the speed of light, and θ and r the azimuthal and radial coordinates, respectively. In this classical model it is assumed that $p = p_0 \cos(2\pi \nu t)$ where ν is determined solely by the driving force of the dipole oscillation independently of dipolar resonance.

23

However, in the case of light scattering by molecules, we cannot ignore the impact of v_m. The induced dipole moment of a diatomic molecule is defined as $\vec{p} = \alpha(q) \, E_0 \cos(2\pi v_0 t) \, \hat{e}$, where E_0 and v_0 are the amplitude and frequency of the incident light waves electric field, and $\hat{e}$ the polarization [40]. The functional dependence of q on α is a consequence of the molecules ability to deform (polarize) being directly related to the distance between the two atoms. Assuming the small amplitude approximation, we can use the Maclaurin series to express α as

$$\alpha \approx \alpha_0 + q \left(\frac{\partial \alpha}{\partial q} \right)_{q=0} \tag{20}$$

where α_0 is the initial polarizability at $q = 0$. Using this approximation, we can therefore express the magnitude p as

$$p = \alpha_0 E_0 \cos(2\pi v_0 t) + \left(\frac{\partial \alpha}{\partial q} \right)_{q=0} q_0 \cos(2\pi v_m t) \, E_0 \cos(2\pi v_0 t) \tag{21}$$

which can be rearranged using the cosine product identity as

$$p = \alpha_0 E_0 \cos(2\pi v_0 t)$$
$$+ \frac{q_0 \, E_0}{2} \left(\frac{\partial \alpha}{\partial q} \right)_{q=0} \{\cos[2\pi(v_0 - v_m)t] + \cos[2\pi(v_0 + v_m)t]\} \tag{22}$$

From Equation 22 we can clearly see that the induced dipole moment is a superposition of three different oscillatory components. The first term in Equation 22 is responsible for the elastically scattered portion of the wave known as Rayleigh scattering and the latter two terms represent inelastic Raman scattering. There are several important observations from this simple phenomenological model. First it is important to note that

$$\frac{q_0}{2} \left(\frac{\partial \alpha}{\partial q} \right)_{q=0} \ll \alpha_0, \tag{23}$$

which indicates that the Raman scattered component will be far weaker than the Rayleigh

scattered component. Secondly, Equation 22 clearly shows that there are components to

the Raman scattered light at the Stokes frequency $v_S = v_0 - v_m$ and the anti-Stokes

frequency $v_{AS} = v_0 + v_m$. For completeness, it should be noted that v_m can also

correspond to rotational frequency for gas phase samples [41]. However, it is important

to point out that this model falsely predicts that the Stoke's and anti-Stokes components

will have the same amplitude.

1.3.1.3 Occupancy Probability. To properly predict the relationship between the

Stokes and anti-Stokes shifted scattering, it is necessary to return to the quantized

vibrational energy levels introduced in Section 1.3.1.2. Figure 9 shows a simplified

energy level diagram, also known as a Jablonski diagram, for the scattering demonstrated

in Equation 22. In this interpretation, an incident photon of energy hv_0 excites the

material to a virtual energy level, corresponding to an energy level which is too high to

excite a vibrational mode and too low to excite an electronic mode. Since this transition is

not quantum mechanically allowed, it must immediately relax back down to an allowed

state. In Rayleigh scattering the material relaxes back to the original state, whereas in

Raman scattering it relaxes to a different vibrational energy level. In the case of Stokes-

shifted Raman scattering the material relaxes to a higher vibrational state corresponding

to a decrease in the scattered photon energy $hv_S = hv_o - hv_m$. In the anti-Stokes case,

the material relaxes to a lower vibrational energy state corresponding to an increase in

photon energy $hv_{AS} = hv_0 + hv_m$.
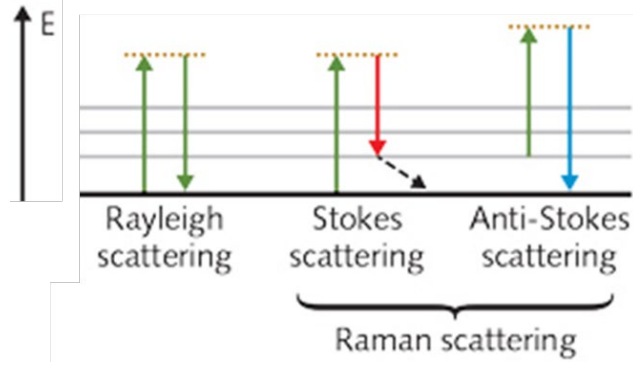
Figure 9. Jablonski diagram for scattering phenomena.

By modeling the vibrational energy levels as phonons (bosonic quasiparticles) it can be shown that for thermal equilibrium,

$$\langle Q_v(t') | Q_v(t' + t) \rangle = \frac{h}{2v_v} \left[n(v_v, T)e^{i2\pi v_v t} + (n(v_v, T) + 1)e^{-i2\pi v_v t} \right] \quad (24)$$

where $\vec{Q}_v$ corresponds to the complex representation of $\vec{q}$ for the vth quantum number and the phonon population follows the Bose-Einstein occupancy $n(v, T) = (e^{hv/k_B T} - 1)^{-1}$, where v is the phonon frequency [42]. Phonons will be described in more detail in Section 1.3.2. When coupled with Equation 22, Equation 24 clearly demonstrates that the intensity of the Stokes scattered photons $I_S \propto n(v, T) + 1$ and the intensity of the anti-Stokes shifted photons $I_{AS} \propto n(v, T)$. Combining these proportionalities with the quartic frequency dependence of dipolar radiation shown in Equation 19 produces the following relationship

$$\frac{I_{AS}}{I_S} = \left(\frac{v_0 + v_m}{v_0 - v_m} \right)^4 e^{-\frac{hv_m}{k_B T}}. \quad (25)$$

Equation 25 leads to the rather straightforward interpretation that the intensity of the anti-Stokes-shifted Raman scattering should always be less than that of the Stokes-shifted Raman scattering due to the Boltzmann probability that the lower energy state is

26

always more likely to be occupied than the higher state. Figure 10 shows a schematic

representation of the scattered intensities, as a function of Raman shift $(\nu - \nu_0)$ measured

in wavenumbers (cm^{-1}).
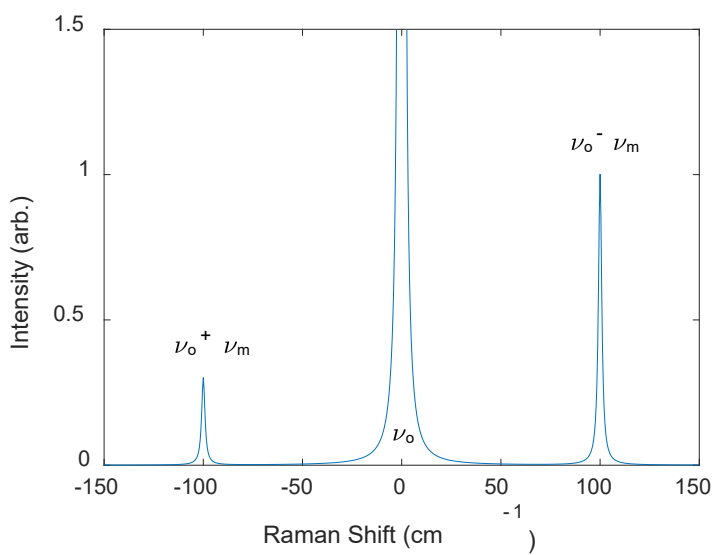
Figure 10. Schematic representation of Raman spectra demonstrating the relative

intensities of the Rayleigh scatter at 0 cm^{-1}, Stokes shifted Raman scatter at 100 cm^{-1}, and

anti-Stokes shifted Raman scatter at -100 cm^{-1}.

1.3.1.4 Vibrational Modes in Multiatomic Molecules. For more complex

molecules it becomes impractical to model every possible vibrational frequency

independently; however, we can use a group-theory approach to take advantage of

molecular symmetries to determine the allowed vibrational modes using character tables.

A detailed review of group theoretic concepts is beyond the scope of this section; Powell

[43] as well as McQuarrie and Simon [44] are excellent resources for additional insight.

To illustrate the power of this approach we will examine cyclooctasulfur shown in Figure

11 which can be described by the D_{4d} point group. The proceeding analysis has been reproduced in part based on the application note titled "Raman vs. Infrared Spectroscopy Measurement of Octasulfur" [45] with permission from Avantes Inc.
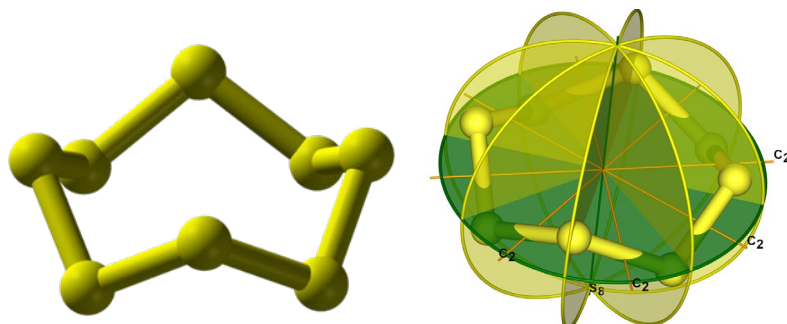
Figure 11. Chemical structure of cylooctasulfur; with some of the symmetry operations in the D_{4d} point group. Reproduced with permission of Avantes Inc. [45].

Table 1

D_{4d} Character Table

D_{4d}	E	$2S_8$	$2C_4$	$2S_8^3$	C_2	$4C_2'$	$4\sigma_d$		
A_1	1	1	1	1	1	1	1		$x^2 + y^2, z^2$
A_2	1	1	1	1	1	-1	-1	R_z	
B_1	1	-1	1	-1	1	1	-1		
B_2	1	-1	1	-1	1	-1	1	z	
E_1	2	$\sqrt{2}$	0	$-\sqrt{2}$	-2	0	0	(x, y)	
E_2	2	0	-2	0	2	0	0		$(x^2 - y^2, xy)$
E_3	2	$-\sqrt{2}$	0	$\sqrt{2}$	-2	0	0	(R_x, R_y)	(xz, yx)

The D_{4d} character table is shown in Table 1, where the possible symmetry operations are listed in the first row, the letters in the first column of the character table are the Mulliken symbols for the irreducible representations, and the right two columns contain the basis coordinates of each representation. Using Table 1, along with a visual inspection of the molecule to determine the total number of unaffected atoms under each symmetry operation, one can determine the total number of vibrational modes for the molecule. In the case of cyclooctasulfur, there are two A_1, one B_1, one B_2, two E_1, three E_2, and two E_3 vibrational modes. While all of these vibrational modes are allowable, not all of them will be Raman active. Since Raman scattering is a nonlinear process dependent on the derivative of the polarizability, only modes with nonlinear basis coordinates will couple to Equation 22. Therefore, only the vibrational modes corresponding to A_1, E_2, and E_3 are Raman active. The modes corresponding to B_2 and E_1 are accessible via infrared spectroscopy since absorbance is linearly related to the dipole moment. The vibrational mode corresponding to B_1 is considered a silent mode since there is no corresponding basis coordinate for that symmetry, and therefore it is not excitable via absorption or scattering.

The Raman active modes can be further divided in two subgroupings corresponding to higher frequency stretching and lower frequency bending modes of the molecule. Only one of each of the A_1, E_2, and E_3 modes is radially symmetric in curvilinear coordinates; therefore, we can classify those as stretching modes. The remaining one A_1, two E_2, and one E_3 modes are then denoted as bending modes. For a more detailed description of this analysis see reference [45].

1.3.1.5 Raman Scattering in Bulk Materials. The analysis presented in the previous section can be generalized to a bulk material through the polarization density field $\vec{P}$, which is defined as the vector sum of induced dipole moments per unit volume and is related to the incident electric field through χ_{ij}. Therefore, χ_{ij} can be viewed as the macroscopic representation of α, allowing for the Stokes-shifted portion of $\vec{P}$ to be expressed as follows [35],

$$P_i(v_S) = \sum \delta\chi_{ij}E_j(v_0) \tag{26}$$

where $\delta\chi_{ij}$ is the modulated Raman susceptibility, which is analogous to the second term in Equation 20. However, since we are now concerned with the three-dimensional structure of the material, it is necessary to use tensor notation to account for the polarization of both the incident $\vec{E}$ field and resulting $\vec{P}$ which will not necessarily be aligned. Since $I \propto |\vec{p}|^2$ (see Equation 19), we can therefore express bulk Raman scattering as $I \propto \left|\hat{e}_S \cdot \delta\chi_{ij} \cdot \hat{e}_0\right|^2$ where $\hat{e}_S$ and $\hat{e}_0$ are the polarization of the scattering and incident fields respectively [35].

Representing bulk material vibrations as phonon modes with displacement vector $\vec{Q}_v$, we can write

$$\delta\chi_{ij} = \sum R_{ij}^v Q_v + \cdots \tag{27}$$

where R_{ij}^v is the first-order Raman tensor corresponding to the vth phonon mode in the material. Similarly, as in Section 1.3.1.2 we can take advantage of crystal symmetries to determine both the Raman active phonon modes as well as their corresponding tensors. For example, at room temperature cyclooctasulfur has an orthorhombic crystal structure

corresponding to the D_{2h} point group, which has four Raman active modes A_g, B_{1g}, B_{2g},

and B_{3g} corresponding to $R_{ij} = \begin{bmatrix} r_{xx} & 0 & 0 \\ 0 & r_{yy} & 0 \\ 0 & 0 & r_{zz} \end{bmatrix}, \begin{bmatrix} 0 & r_{xy} & 0 \\ r_{xy} & 0 & 0 \\ 0 & 0 & 0 \end{bmatrix}, \begin{bmatrix} 0 & 0 & r_{xz} \\ 0 & 0 & 0 \\ r_{xz} & 0 & 0 \end{bmatrix}$, and

$\begin{bmatrix} 0 & 0 & 0 \\ 0 & 0 & r_{yz} \\ 0 & r_{yz} & 0 \end{bmatrix}$, respectively.

Since these phonon modes represent long-range cooperative vibrations across the entire crystal structure (see Section 1.3.3), they tend to manifest at lower frequencies than those of the molecular bending or stretching modes described in the previous section. Figure 12 shows the Raman spectra of room temperature cyclooctasulfur powder from -550 cm^{-1} to 550 cm^{-1} measured with a 785-nm CleanLine laser and TR-PROBE from Coherent, fiber-coupled to a HORIBA LabRAM HR Evolution spectrometer. This spectrum clearly demonstrates three groupings of peaks symmetrically around 0 cm^{-1}. It is important to note that both the excitation and collection light were randomly polarized, and since the sample was in powder form, all possible vibrational modes were simultaneously excited. A more detailed band assignment for cyclooctasulfur has been performed by Becucci *et al.* using polarized Raman spectroscopy at both room and cryogenic temperatures [46].
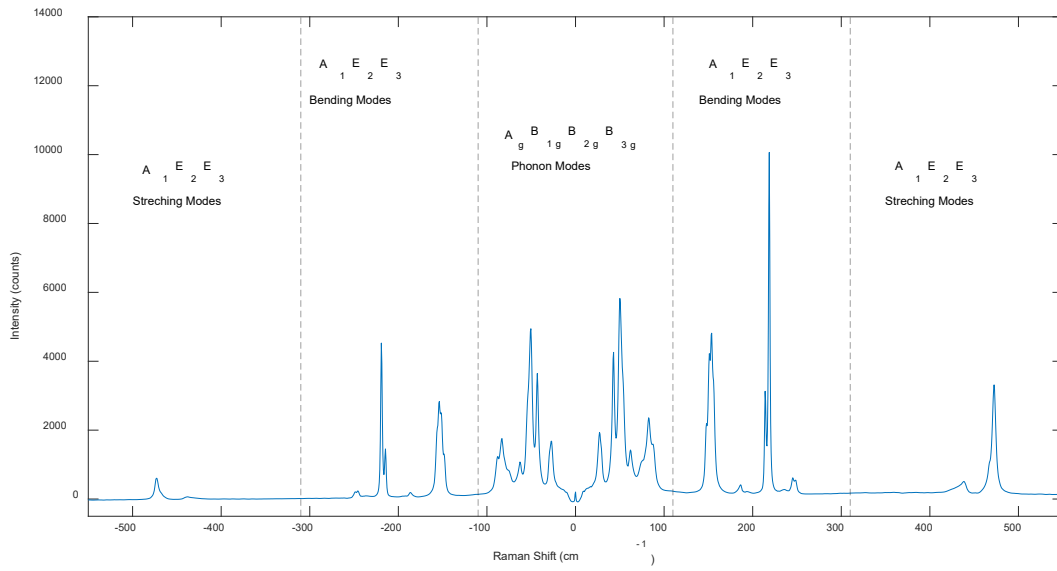
Figure 12. Raman spectrum of cyclooctasulfur at room temperature with phonon, bending, and stretching regions labeled.

When heated above 95.3 °C the structure of cyclooctasulfur transforms to a monoclinic form now having only two active phonon modes corresponding to the A_g and

B_g irreducible representations where $R_{ij} = \begin{bmatrix} r_{xx} & 0 & 0 \\ 0 & r_{yy} & 0 \\ 0 & 0 & r_{zz} \end{bmatrix}$ and $\begin{bmatrix} 0 & r_{xy} & 0 \\ r_{xy} & 0 & 0 \\ 0 & 0 & 0 \end{bmatrix}$,

respectively. When further heated past its melting point (~113 °C), cyclooctasulfur loses all long-range order and can no longer be treated group theoretically for the determination of its phonon modes. Phonon modes in amorphous materials will be examined in great detail in Section 1.3.3, but for now it is important to know that they form a continuous distribution which can only be described by a vibrational density of states $g(\nu)$.
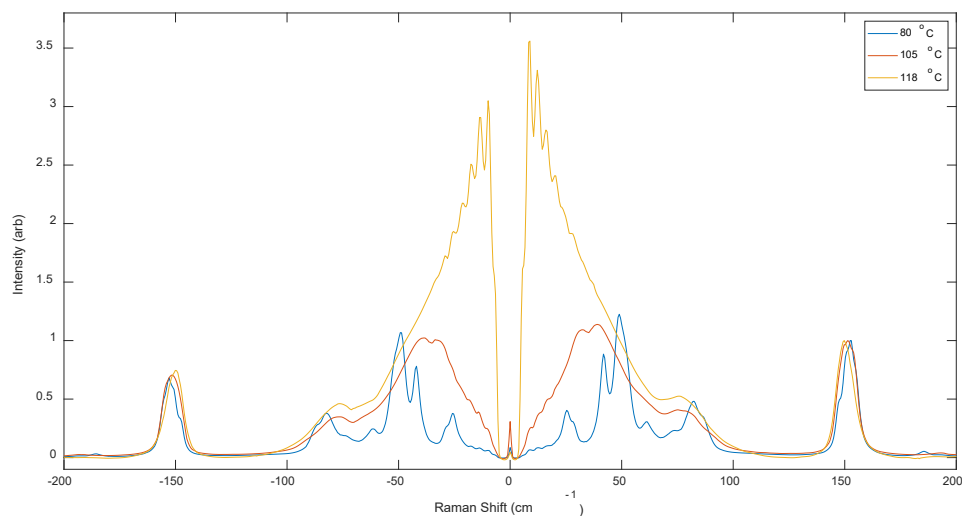
Figure 13. Raman spectrum of cyclooctasulfur at (blue) 80 °C, (red) 105 °C, and (yellow) 118 °C normalized to the ~150 cm⁻¹ molecular bending mode. The low-frequency oscillations in the spectrum at 118 °C are likely due to etaloning.

Figure 13 shows the Raman spectra of cyclooctasulfur at 80 °C , 105 °C , and 118 °C which correspond to the orthorhombic, monoclinic, and liquid phases, respectively. These spectra clearly demonstrate the evolution of the phonon modes as the material structure changes. All three spectra in Figure 13 were normalized to the molecular bending mode at ~150 cm⁻¹ since intramolecular vibrations are relatively stable under structural changes. Small changes in the molecular bending modes are also present due to changes in steric conditions, however not nearly to the same extent as in the phonon modes.

1.3.2 Phonons

As stated in the previous section vibrational modes can be treated as bosonic quasiparticles known as phonons. Phonons are generally described as quantized acoustic waves analogous to how photons are used to describe quantized electromagnetic waves. [47] However, unlike photons which can exist without a host medium, phonons cannot exist independently. Phonons are also commonly referred to as quantized particles of heat as it can be shown that the Fourier law and thermal conductivity are a direct result of phonon scattering in insulators. [47, 48] As this dissertation is primarily focused on low-frequency Raman spectroscopy which is directly related to photon-phonon interactions, it is important to provide a brief overview of phonons.

1.3.2.1 Phonon Dispersion. The most simplistic way to consider phonon modes is by expanding the harmonic oscillator model presented in Section 1.3.1.1 to a one-dimensional lattice consisting of N atoms separated by a constant lattice spacing a, all having an equal restoring force constant K. This model allows us to represent the displacement as a traveling plane wave across the lattice: $Q = A \sum e^{-i(2\pi v - kja)}$ where A is the amplitude, a the distance between neighboring atoms, and k the magnitude of the wavevector [48]. Assuming the lattice is monoatomic consisting of atoms with mass m and using the same Hooke's law-based derivation as before, we can show that

$$v = \frac{1}{\pi}\sqrt{\frac{K}{m}}\left|\sin\frac{ka}{2}\right|,$$

(28)

and

$$k = \frac{2\pi}{aN}l$$

(29)

where $l = 0, \pm1, \pm2, ...$ is an integer relating to the phonon mode number [48]. It can also be easily shown through the use of a periodic potential well that the phonon energy can be similarly quantized as in Equations 16 and 18. The maximum phonon wavelength is $2a$ since each neighboring atom in the lattice limits k to $-\frac{N}{2} \leq l \leq \frac{N}{2}$. Furthermore, as $l \rightarrow \frac{N}{2}$, $k \rightarrow \frac{\pi}{a}$ corresponding to the edge of the unit cell in reciprocal space, known as the first Brillouin zone. Therefore, we can easily generalize this model to three-dimensions where the phonon energy increases sinusoidally from the Brillouin zone center, reaching a maximum at the critical points along the edges.

When the lattice model is expanded to allow for more than one atom to be located at each lattice point, we now must consider phonon modes associated with out-of-phase vibrations. A detailed derivation of out-of-phase phonon modes is beyond the scope of this dissertation, but it can be shown that $v \propto 1 + \sqrt{\cos(ka)}$ for the out of phase component [47]. Therefore, the out-of-phase phonons have an inverse dispersion relationship with the highest energy at the zone center decreasing towards the edge and will always have higher energy than in-phase phonons. Since these higher energy phonons generally oscillate at the same frequency as infrared light, they are referred to as optical branch phonons and the lower energy phonons are referred to as acoustic branch phonons. Figure 14 shows a schematic representation of the corresponding dispersion relationships for both the acoustic and optical branches.
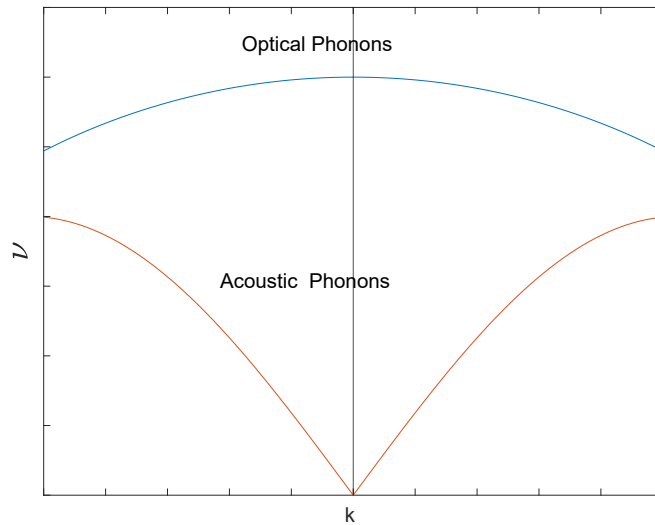
Figure 14. Schematic representation of optical and acoustic phonon dispersion relationships.

For completeness it should be noted that the approximations used in this model are only valid at relatively low frequencies and do not account for the phonon polarization which can split each branch into three different sub-bands. Additionally, Figure 14 assumes that the phonon modes are symmetric throughout the Brillouin zone, which is typically not a correct assumption. These effects on the phonon dispersion relationships are clearly seen in Figure 15, where Adessi *et al.* determined the phonon dispersion relationships for a two-dimensional monolayer of MoS_2 [49]. In Figure 15, Γ represents the Brillouin zone center and K and M are critical points at the edge of the first Brillouin zone. The polarizations of the acoustic phonons are labeled ZA, TA, and LA which corresponds to the out-of-plane, in-plane, and longitudinal vibrational components. For the optical branch, the authors chose to label the phonons by their irreducible

36

representation; however, they note that A_2'' and A_1 correspond to out-of-plane ZO polarizations and E' and E'' correspond to in plane TO polarizations.
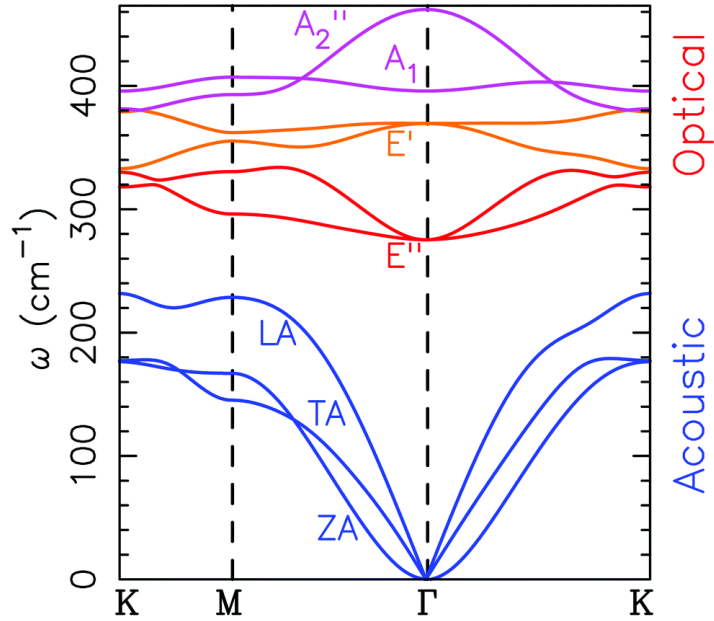
Figure 15. Phonon mode dispersion on 2D MoS₂. Reproduced in accordance with creative commons CC BY-NC 3.0 DEED [49].

1.3.1.2 Phonon Density of States. Since Raman scattering is produced by the creation or annihilation of a phonon, a proper accounting of the total phonon degeneracy is critical for predicting the relative intensities of the scattered photons. This is done through the density of states $g(v)$, which is defined as

$$g(v) = \frac{1}{V}\frac{d\Omega}{dv} \tag{30}$$

where Ω is the total number of possible phonon states [48]. From the Debye model, which assumes the acoustic phonon dispersion is a linear function where the slope is approximated as the speed of sound v_D, $g(v)$ can be approximated as [48]

$$g(v) = \begin{cases} \dfrac{6\,v^2}{v_D^3} & v < v_D \\ 0 & v > v_D \end{cases} \tag{31}$$

where v_D is the Debye frequency. This is equivalent to stating that the material is isotropic with a maximum phonon wavevector k_D and frequency v_D. For the optical branch phonons, the Einstein model is typically employed to approximate the phonon dispersion as a flat line at frequency v_E, and the corresponding $g(v) \to \delta(v - v_E)$. While useful approximations, both the Debye and Einstein models break down at the critical points where discontinuities in the phonon dispersion lead to spikes in $g(v)$ known as van Hove singularities. Figure 16 shows a schematic representation comparing $g(v)$ in both an "ideal" and a "real" material.
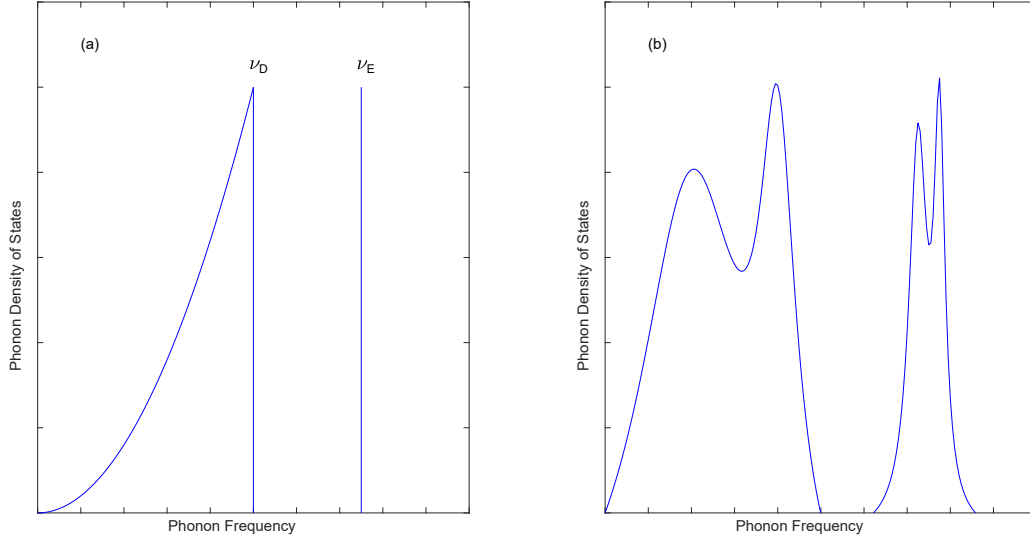
Figure 16. Schematic representation of phonon density of states (a) from the Debye and

Einstein models and (b) for a real material adapted from [48].

It is important to point out that $g(v)$ only provides information about the total

number of possible phonon states; to determine the total number of phonons, one must

factor in the Bose-Einstein occupancy $n(v, T)$. However, once accounted for we now

have a powerful tool for not only determining the relative intensity of the Raman

scattered photons but also for relating $g(v)$ to the classical thermodynamic properties

introduced in Section 1.2.1. Since each phonon represents a quantum of vibrational

energy, the total internal thermodynamic energy U of a material can be determined by

$$U = h \int v \, n(v, T) g(v) dv. \tag{32}$$

Equation 32 is often used to determine the isochoric heat capacity $C_V = \frac{\partial U}{\partial T}$ which

can be combined with the Debye and Einstein models to show $C_V \propto T^3$ at low

temperatures and is constant at high temperatures in an electrically insulating solid [47, 48]. An alternative interpretation which we make use of in the following chapter allows for $g(v)$ to also be related to the entropy:

$$S = -k_B \int g(v) \left[\ln \left(1 - e^{-\frac{hv}{k_B T}} \right) + \frac{hv}{kT \left(1 - e^{\frac{hv}{k_B T}} \right)} \right] dv. \tag{33}$$

1.3.1.3 Phonons in Amorphous Materials. As the structure of a material becomes less ordered, $g(v)$ simultaneously broadens and red shifts. For example, crystalline silicon has a narrow Raman active optical phonon at ~520 cm⁻¹; however as the material becomes more amorphous the band broadens and shifts to ~480 cm⁻¹ [50]. Figure 17 shows an example of crystalline and semi-crystalline Raman spectra collected with a HORIBA LabRAM HR Evolution spectrometer and a 532-nm excitation laser. A second common example is the ~1590 cm⁻¹ optical phonon present in graphitic materials and the corresponding disorder band at ~1354 cm⁻¹ [51].
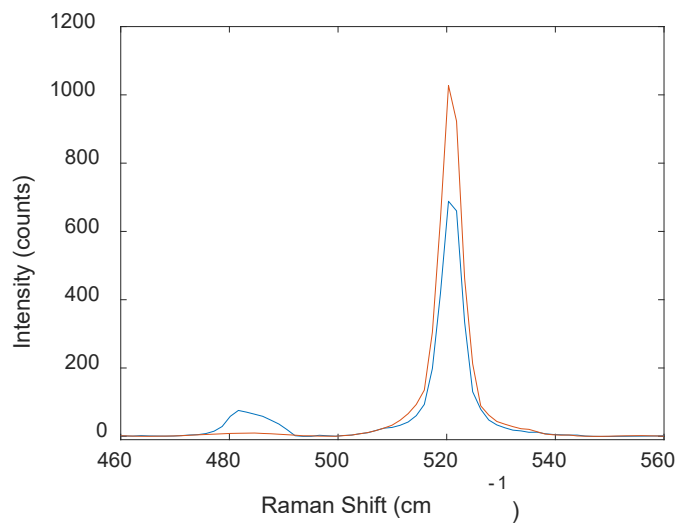
Figure 17. Raman spectra of crystalline silicon (red) and semicrystalline silicon (blue).

Typically, optical phonons cannot be supported in amorphous materials due to the lack of long range order; however, low-frequency acoustic phonon modes are still present [52]. This results in a broad continuous function for $g(v)$, which when normalized by the Debye frequency dependency $\frac{g(v)}{v^2}$, has a characteristic log-normal distribution not seen in crystalline materials [53]. The maximum of $\frac{g(v)}{v^2}$ is known as the Boson peak and has been studied extensively in disordered solids [54-56] and biomolecules [57-59]. The exact origins of the Boson peak in $g(v)$ are often debated [60]; however, there is ample experimental evidence linking the Boson peak amplitude and position to sound velocity [61], correlation length [55], and modulus [62].

Baggioli and Zaccone recently developed a relatively simple Green's function for modeling $g(v)$ in hard amorphous materials [63], which was shown to match previously reported experiments by both Chumakov *et al.* [64] and Kamitakahara *et al.* [65]. In their model they used a pseudo-Brillouin zone boundary approach to modify the propagation term with quartic damping. The corresponding damping coefficient A_λ was determined by the associated wavevector magnitude at the van Hove singularity $k_{VH,\lambda} \equiv \frac{v_\lambda}{\sqrt{2A_\lambda}}$ where the subscript λ indicates the longitudinal (L) or transverse (T) polarization [63]. Using their model, Baggioli and Zaccone showed that $g(v)$ was dominated by the transverse phonons, and therefore the longitudinal phonons could be effectively ignored when analyzing the Boson peak. Figure 18, which was reproduced from [63], clearly demonstrated the effects of v_T on the height and position of the Boson and van Hove peaks. The Boson peak intensity decreases as v_T increases, which is consistent with the dependence of S on $g(v)$, as discussed in the previous section. The van Hove peak is also

slightly affected by the change in v_T, however to a much smaller extent than the Boson peak. As we will demonstrate in Chapters 2 and 3, the high sensitivity of the Boson peak and relative insensitivity of the van Hove peak is foundational to the results of this dissertation. Additionally, Figure 18 shows that there is a direct linear relationship between the Boson peak position and v_T, and as Baggioli and Zaccone point out in their analysis, v_T is proportional to the square root of the shear modulus G [63]. In Chapter 4 we experimentally demonstrate this relationship by comparing low-frequency Raman spectroscopy to shear rheology.
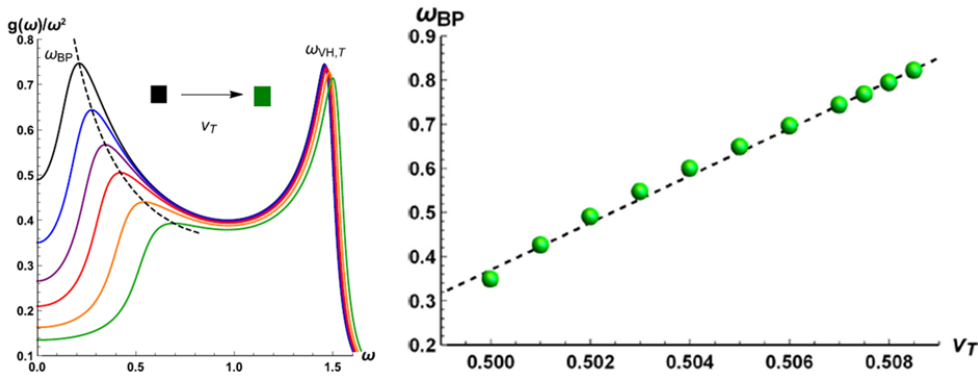
Figure 18. Effect of increasing transverse speed v_T of sound on $g(v)$. Reproduced in accordance with CC BY-NC 4.0 DEED [63].

      The two most common methodologies for studying $g(v)$ are inelastic neutron scattering (INS) and Raman scattering. INS allows for direct measurement of $g(v)$ but the facilities requirements for operating a neutron source and spectrometer are prohibitive, making Raman the preferred approach for applied sciences. The Stokes-shifted Raman scattering intensity $I_R(v)$ can be related to $g(v)$ by

$$I_R(v) = \frac{C(v)g(v)}{v}[n(T,v) + 1] \qquad (34)$$

where $C(v)$ is the coupling coefficient [66]. INS data is typically presented as $\frac{g(v)}{v^2}$; therefore the most common way to determined $C(v)$ is by comparing INS data to the renormalized Raman spectrum $\frac{I_R(v)}{v[n(T,v)+1]}$ [66, 67]. In this dissertation we are not concerned with the exact value of $C(v)$ although we do use the general form of this relationship in Chapter 2 to develop a model to determine the acoustic phonon contribution to the low-frequency Raman spectra.

1.3.3 Raman Instrumentation

Modern Raman spectrometers can be roughly grouped into three main categories – portable/handheld [68], fiber-optic probes [69], and microscopes [70]. However, regardless of the categorization, all Raman spectrometers contain three main components – a laser, a spectrometer, and collection optics. In this section we will exclusively focus on fiber-optic probe-based systems since the work in this dissertation is conducted with a TR-PROBE from Coherent. However, it is important to note the basic instrumentation, designs, and concepts are easily generalized to the other two categories.

1.3.3.1 Laser. Raman spectroscopy measures the change in wavelength while simultaneously providing additional degrees of freedom and constraints not present in other spectroscopies [32]. As discussed in Section 1.3.1.2, the Raman shift is defined as $v = v_s - v_0$ where v_0 is the frequency of the excitation source and v_s is the frequency of the scattered light. Therefore, having precise control over the starting wavelength is critical, which is why lasers are used exclusively as the excitation source in modern Raman instrumentation.

The spectral linewidth and stability of the laser have a direct impact on the overall quality of the Raman spectrum. For example, a Raman peak with a spectral linewidth of 1 cm^{-1} is equivalent to a width of 0.04 nm at 632.8 nm. Therefore, gas lasers such as HeNe and Ar-ion lasers were rapidly adopted as they naturally possess a narrow linewidth and exhibit little to no mode instability. However, gas lasers have several inherent drawbacks: relatively large size, low output power, and a short lifetime. As solid-state laser technology rapidly advanced throughout the 1990s, narrow-linewidth, frequency-doubled, diode-pumped solid-state (DPSS) lasers began to overtake gas lasers since they could provide similar spectral performance with longer lifetimes and less power consumption in a compact form factor. However, frequency-doubled DPSS laser (typically Nd:YAG or Nd:YVO$_4$) sources were still less than ideal for many applications since they were limited to visible wavelengths (typically 532 nm). While at first glance shorter wavelengths appear to be more advantageous for Raman scattering due to the ν^4 dipolar radiation frequency dependence, in practicality short-wave infrared (typically 785 nm) excitation is preferred in most cases. This is because in most organic materials the band gap energy between the highest occupied and lowest unoccupied molecular orbitals typically correspond to ultraviolet and visible photon energies. Therefore, visible lasers can excite the sample to a higher electronic energy level and induce photoluminescence, also known as autofluorescence. This results in spectral interference and in some cases completely overpowers the Raman spectrum.

During the 1990s diode lasers became one of the most widely produced laser sources, particularly at ~780 nm due to their use in compact disk (CD) players. While these laser sources were at the ideal wavelength for Raman spectroscopy, they were far

44

too unstable and broadband to be of practical use at the time. External-cavity diode lasers based on either the Littrow or Littman-Metcaff optical designs have long been used to spectrally narrow and tune diode lasers [71, 72]. However, these laser sources are too expensive for integration into most Raman instrumentation. Distributed feedback (DFB) and distributed Bragg reflector (DBR) laser sources integrate a grating directly into the diode itself to narrow the linewidth [73]. DFB and DBR lasers are low cost, low-power consumption, and monolithic, and they were critical to the rapid development of the telecom industry throughout the late 1990s and early 2000s. However, these laser sources were never designed to be operated at higher power and are extremely sensitive to temperature and drive current limiting their deployment in commercial Raman instrumentation.

In 1999 Efimov, Glebov *et al.* demonstrated the ability to produce a volumetric Bragg grating (VBG) in photothermorefractive glass [74]. This development not only led to a revolution in laser sources for Raman spectroscopy, but as we will discuss in Section 1.3.3.3, provided the technological foundation for the entirety of the work in this dissertation. The ability to use holographic techniques to produce high efficiency VBGs in glass enabled external cavity diode lasers to be shrunk down small enough to fit into a 14-pin butterfly package or a 5.6 mm diameter TO-can. This compact form factor combined with the high power (100s mW) and high temperature stability rapidly made VBG-based laser didoes the predominant laser source for Raman instrumentation [75-77]. All the work in this dissertation was conducted with CleanLine VBG stabilized diode lasers from Coherent Inc. at either 808 nm or 785 nm.

1.3.3.2 Spectrometer. Since Raman spectroscopy is typically performed in the visible or near-infrared region of the spectrum, the spectrometer requirements are relatively straightforward. In this section we only provide a brief overview of spectrometer requirements and designs commonly used in Raman spectroscopy. Lewis and Edwards is an excellent resource for a more comprehensive review of the subject [34]. The most common spectrograph design used in Raman spectroscopy is the crossed Czerny-Turner optical design. A Czerny-Turner spectrograph consists of an entrance slit, which controls the amount of light allowed into the device and serves as the "object" in the imaging system. The light from the entrance slit is then collimated with a concave mirror and directed to a reflective grating which can either be at a fixed position or have an adjustable angle. The diffracted light is then imaged to the detector plane with a second concave mirror which results in a plurality of monochromatic images of the original polychromatic entrance slit. A one- or two-dimensional array photodetector is then used to measure the photon flux and each pixel is correlated to a wavelength based on calibration with an emission standard.

Czerny-Turner spectrographs are highly configurable, and since they are purely reflective, they are insensitive to chromatic aberration. However, they do suffer from one major drawback. All mirror-based optical designs are inherently highly off axis, leading to an abundance of coma and astigmatism. Coma manifests as a variation in magnification as a function of exit pupil height, and astigmatism results in a separation of the focal points in the horizontal and vertical axes. Of these two aberrations, coma is by far the biggest detriment to spectral resolution, since spectral features typically only require resolution in one dimension. Applying the thin-lens approximation, it can be

shown that coma is inversely proportional to the f-number squared [78]. Therefore, most Czerny-Turner spectrographs are designed with relatively high f-numbers to minimize the effects of coma. However, as the f-number of an optical design increases, the collection efficiency decreases, leading to an inevitable tradeoff between efficiency and resolution.

On-axis refractive-based transmission spectrographs offer far greater collection efficiency since they can be designed at much lower f-numbers. However, the use of refractive optics introduces chromatic aberration and does not allow for grating tunability. For many Raman applications, this tradeoff is more than acceptable since the total wavelength range of interest is typically small and a single laser wavelength is generally employed. Therefore, with the aid of compound lenses made from materials with different indexes of refraction and dispersion curves chromatic aberration can be minimized over the wavelength range of interest. In this case, low f-number transmission spectrographs can provide similar resolution to Czerny-Turner spectrographs with much higher collection efficiencies. In this dissertation we used both types of spectrometers depending on the application. In Chapter 2 we utilized the HORIBA LabRAM HR Evolution rotating-grating crossed Czerny-Turner spectrometer and in Chapters 3 and 4 we used the Ibsen Photonics EAGLE Raman-S high-throughput transmission spectrometer. Both spectrometers used a high detectivity thermoelectrically (TE) deep-cooled, back-thinned, back-illuminated, charge coupled device (BT-CCD) detector. It should be noted, however, that a detector of this quality was somewhat overkill for the work presented in this dissertation; a front-illuminated, single-stage, TE-cooled CCD would have likely been sufficient.

1.3.3.3 Collection Optics. As stated previously, we exclusively made use of fiber optic probe-based Raman collection optics in this dissertation. Fiber optic Raman probes are available in a wide range of optical designs [79-82], but for the most part they follow the same basic structure as shown in Figure 19. The laser light is coupled into the probe via an excitation fiber and collimated with an aspheric lens. The light is then passed through an edge or a notch filter, often referred to as a laser-line filter, to remove amplified spontaneous emission (ASE) from the laser source. The ASE is typically 40 dB below the laser line; however, since the Raman scattering is extremely weak ~60-70 dB lower than the Rayleigh scattering, ASE can overwhelm the Raman signal if not properly filtered out. Next the light goes to a dichroic mirror which either reflects or transmits the laser wavelength and is then focused on the sample via another lens. The same lens that focuses the laser light onto the sample also collects and collimates the backscattered light. The scattered light is then sent back through the same dichroic mirror which blocks the Rayleigh-scattered light and passes the Raman-scattered light. However, since most dichroic mirrors have a blocking efficiency of ~20 dB, a fair amount of Rayleigh-scattered light passes through relative to the Raman-scattered light. Therefore, an additional edge or notch filter is used to further reduce the Rayleigh-scattered light before the light is focused into the collection fiber and sent to the spectrometer.
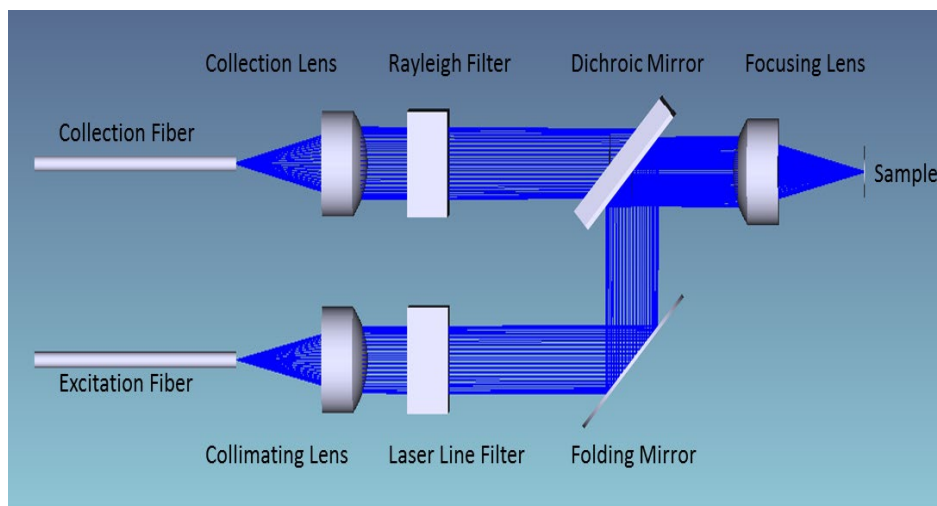
Figure 19. Typical optical design for a fiber optic Raman probe.

Traditional thin-film-based optical filters can pass the Raman scattered light with a cut-on of ~ 100 cm^{-1}, which is more than sufficient to measure Raman spectra of molecular vibrations but does not permit the measurement of most acoustic phonon modes (see Figure 12). Historically, for experiments requiring sub-100 cm^{-1} spectral information, double or triple monochromators were needed to efficiently filter out the Rayleigh scattering while passing the low-frequency Raman scattering. This was accomplished by coupling two or more Czerny-Turner spectrographs in tandem where the entrance slit of the second spectrograph was placed at the detector plane of the first. While highly effective, this approach is rather large and expensive, making it impractical for widespread commercial applications. Carriere, Glebov, Heyler and others have demonstrated that similar filtration is achievable by using two VBGs to simulate a double monochromator [83-85].

49
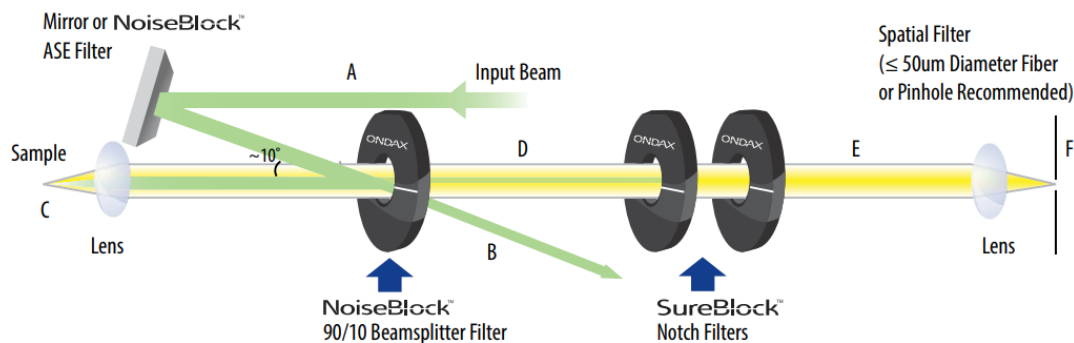
Figure 20. Low-frequency fiber-optic Raman probe design. Reproduced with permission from Coherent Inc.

To illustrate the blocking efficacy and cut-on of the probe TR-PROBE from Coherent (which used the optical design shown in Figure 20), we sent a broadband white light source into the probe and measured the spectrum using the HORIBA LabRAM HR Evolution spectrometer. The results shown in Figure 21 clearly show that the probe was able to narrowly filter out the light to within ± 7 cm^{-1} of the Rayleigh line, which is indicated by the black dashed lines. This allows for not only the measurement of low-frequency acoustic phonon modes but also for the collection of anti-Stoke scattering as well. Having access to the anti-Stokes signal permits the temperature to be determined via Equation 25. More importantly, it provides an internal reference in the low-frequency region to verify that the measured signal is in fact Raman and not autofluorescence or ASE since the Raman features are symmetric around 0 cm^{-1} while the other signals are not.
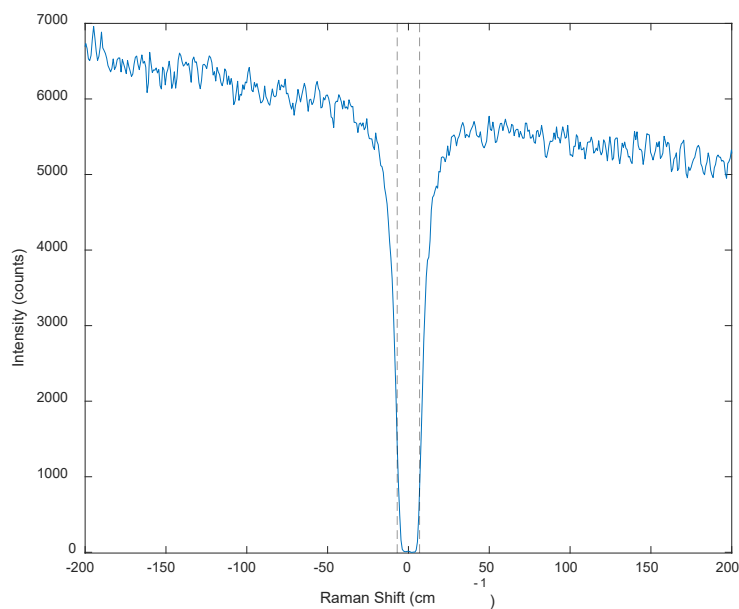
Figure 21. Filter response of TR-PROBE.

1.4 Dissertation Summary

In this work we leveraged the flexibility of fiber optic Raman probes based on the dual-VBG optical designs to develop practical methods for *in situ* monitoring of kinetic processes in polymers. Since the low-frequency Raman spectra of polymers is directly related to the phonon density of states as shown in Equation 34, we have been able to correlate the low-frequency spectrum with structural changes. In Chapter 2, we demonstrate the ability to determine glass transition kinetics using the low-frequency Raman probe despite the filter roll off below ~15 cm^{-1} (see Figure 21) by normalizing the low-frequency Raman peak to the shoulder of the feature which is attributed to the van Hove singularity. We also developed a first-principles peak-fitting model which allowed us to decouple the contributions of the quasi-elastic Rayleigh scattering, the Boson peak,

51

and the van Hove peak. Chapter 3 demonstrates the ability to use the same normalization method to monitor polymerization since the low-frequency region of the Raman spectrum is directly related to conformational entropy and the modulus of amorphous materials, both of which change as the resin polymerizes. By comparing the "structural" conversion determined from the low-frequency region to the chemical conversion determined using the chemical fingerprint region we were able to demonstrate a direct linear relationship with a few notable exceptions. In Chapter 4 we expand on the work of Chapter 3 by comparing two chemically identical yet rheologically different resin systems, to better understand the transient discrepancies between chemical and structural conversion observed in Chapter 3. Using photorheology, we demonstrate a correlation between structural conversion and storage modulus, which is not present in chemical conversion. However, we are still able to produce master cure kinetics curves with comparable kinetic constants using both the chemical and structural conversion methodologies. We also present a semi-empirical model for parametric analysis of the structural conversion, chemical conversion, and photorheological (shear modulus) conversion, which has the potential to allow for non-contact modulus determination via low-frequency Raman. In Chapter 5 we provide overall conclusions for Chapters 2, 3, and 4 as well as a discussion regarding potential future work.

Chapter 2

Practical Method for Measuring Glass Transition in Polymers with Low-Frequency

Raman Spectroscopy

2.1 Abstract

Glass transition temperature is one of the most important characteristics to describe the behavior of polymeric materials. When a material goes through glass transition, conformational entropy increases, which affects the phonon density of states. Amorphous materials invariably display low-frequency Raman features related to the phonon density of states resulting in a broad disorder band below 100 cm^{-1}. This band includes the Boson peak and a shoulder, which is dominated by the van Hove peak, and quasi-elastic Rayleigh scattering also contributes to the signal. The temperature dependence of the ratio of the integrated intensity in proximity of the Boson peak to that of the van Hove peak shows a kink near the glass transition temperature as determined by differential scanning calorimetry. Careful analysis of the Raman spectra confirms that this is related to a change in the phonon density of states at the transition temperature. This makes low-frequency Raman a promising technique for thermal characterization of polymers because not only is this technique chemically agnostic and contactless, but it requires neither intensity calibration, nor deconvolution, nor chemometric analysis.

2.2 Introduction

The glass transition is loosely defined by the temperature at which an amorphous material gains enough internal energy to overcome vitrification and begins to flow as a viscous liquid. As a result, the glass transition temperature T_g is one of the most important parameters when analyzing the structure-property-processing relationships in polymer science and engineering. As discussed in Chapter 1, while the melting point temperature of crystalline materials, at constant pressure, results from a clearly defined phase transition detectable by a discontinuity in extensive properties such as volume, enthalpy, and entropy, the glass transition is a gradual process whereby the material slowly becomes less "glassy" and more "rubbery" as the temperature increases. Therefore, T_g is characterized as a rate-dependent quasi second-order thermodynamic phase transition which can be identified by a change in the slope of volume, enthalpy, or entropy as a function of temperature [13]. Since it is challenging to directly measure these extensive quantities in the laboratory, T_g is traditionally measured indirectly by techniques such as differential scanning calorimetry (DSC) and dynamic mechanical analysis (DMA).

The simpler of these two approaches is DSC, which measures the heat capacity (or heat flow) of a material as a function of temperature T. Since heat capacity is equal to the derivative of the enthalpy with respect to T, holding composition and pressure or volume, a step change in the DSC curves can correlate to a glass transition. By contrast, DMA probes viscoelasticity by measuring the storage and loss moduli as functions of temperature. While DMA provides a more direct measurement of the "glassy" to "rubbery" transition, there is no universally accepted definition of the exact transition

point, be it the onset temperature of the decrease in storage modulus E', the temperature of the maximum in the loss modulus E'', or the temperature of the peak of the loss tangent $\frac{E'}{E''}$. Furthermore, there is rarely agreement among any of these various methods for determining T_g. For instance, one study reported T_g values for polystyrene measured at 2 °C/min ranging from 84.7 to 89.3 °C when determined from DSC measurements and ranging from 89.4 to 111.5 °C when ascertained from DMA results [11].

Both infrared and Raman spectroscopies have been explored as potential alternative methodologies for detecting the glass transitions in polymers [86-89]. Raman spectroscopy is of particular interest due to the high spatial resolution and inherent non-contact nature of laser-based techniques. However, most Raman-based approaches to measuring T_g have focused on detecting relatively small changes in either the intensity or position of peaks of bending or stretching modes which arise at T_g due to changes in steric hindrances [88, 90]. Low-frequency Raman has been used to investigate the effects of aging and thermal history on amorphous polymers [91], and as a normalization factor for determination of glass transition kinetics via quasi-elastic Rayleigh scattering (QERS) [92, 93]. Still, there seems to be no discussion in the literature around the direct use of low-frequency Raman to measure glass transition kinetics. Furthermore, previous studies in this area relied upon complex multi-grating monochromators and polarization sensitive collection optics.

In this work, we present a methodology which uses low-frequency Raman spectroscopy for determining T_g of polymers by using only a double volume-holographic-grating-based fiber optic Raman probe, with an unpolarized laser source and collection optics. The use of two gratings as a Rayleigh filter in a fiber optic Raman

probe has been well demonstrated as a means of simulating a double monochromator providing access to low-frequency vibrational modes [84, 94, 95], but there is still significant filter roll-off below ~15 cm^{-1}, which can often make quantitation rather challenging. Here we demonstrate the ability to determine T_g directly from the low-frequency Raman spectra, irrespective of the filter roll-off, and support this with first principles modeling. This technique permits direct investigation of thermal-structural properties, in a contactless, non-destructive manner and is inherently well suited for *in situ* or high spatial resolution applications. Furthermore, the high scattering efficiency in this region of the spectrum permits studies of relatively fast kinetics.

Traditional Raman spectroscopy provides a chemical fingerprint by probing the various vibrational modes of a molecule [96], but it is also sensitive to phonon modes which provide insight into the overall structure of the material [84]. Two common examples are the presence of c-Si (~520 cm^{-1}) and a-Si (~480 cm^{-1}) bands [50] as well as the *g* (~1582 cm^{-1}) and *d* (~1380 cm^{-1}) bands in graphene [51], which are examples of optical phonons due to vibrations along a crystal axis. Raman spectroscopy is also sensitive to acoustic phonons, which arise from in-phase lattice vibrations, but due to their extremely low energy, their modes are incredibly close to the Rayleigh line. Until recently, this made it challenging to measure them without the use of a double or triple monochromator [97-105].

In highly ordered crystalline materials, acoustic phonon modes produce sharp bands corresponding to the crystallographic axes. As the material becomes less ordered, the acoustic phonon modes tend to simultaneously broaden and redshift. In the case of amorphous materials, the phonon density of states $g(\nu)$ is dominated by two main

features – the Boson and van Hove peaks [63, 95, 106-114]. Therefore, in soft amorphous materials, the Raman scattering intensity $I_R(\nu)$ can be directly related to $g(\nu)$ by

$$I_R(\nu) = \frac{C(\nu)g(\nu)}{|\nu|}[n(\nu,T) + H(\nu)] \tag{35}$$

where ν is the frequency of the Raman shift, $C(\nu)$ the coupling coefficient and $n(\nu,T) = (e^{h\nu/kT} - 1)^{-1}$ the Bose-Einstein distribution function [42, 99, 115-117]. The Heaviside function $H(\nu) = 1$ for $\nu \geq 0$, 0 otherwise, accounts for the difference in the probability between the Stokes and anti-Stokes shifted photons.

The tendency of phonon modes to redshift and broaden is a universal feature of amorphous materials. Therefore, $I_R(\nu)$ can be considered as the disorder band of the polymer, analogous to the a-Si band or the d band in graphene. The primary difference is that the extremely soft nature of polymers shifts the disorder band into the low-frequency region of the Raman spectrum. We propose a method of using this disorder band to monitor the change in the phonon density of states as a function of temperature to determine T_g of a polymer.

2.3 Experimental Methods and Procedures

2.2.1 Materials

We utilized polystyrene pellets (CAS# 9003-53-6) with an approximate molecular weight of 210,000 g/mol purchased from Scientific Polymer Products, Inc. We also used polylactic acid (PLA) pellets (CAS# 26100-51-6) with an approximate molecular weight of 160,000 g/mol purchased from IC3D Industries, and poly(methyl methacrylate) (PMMA) pellets (CAS# 9011-14-7) with unknown manufacturer and molecular weight.

2.2.2 Raman Measurements

The samples were placed in a THMS600 temperature-controlled microscope stage from Linkam, allowing T to be controlled with an accuracy of < 0.01°C. The stage was sealed, and measurements were taken through the lid window. No extra efforts were taken to control the internal environment. Liquid nitrogen was utilized to stabilize the heating rate even though the samples were never cooled below 20 °C. The Raman measurements were made with an 808-nm CleanLine laser and TR-PROBE from Coherent coupled with an 8-mm working distance focusing lens. The TR-PROBE is a fiber-coupled Raman probe capable of measuring both Stokes and anti-Stokes Raman scattering to within approximately ±7 cm^{-1} of the Rayleigh line. The scattered light was then fiber coupled directly into a HORIBA LabRAM HR Evolution spectrometer. It is important to note that a fixed grating modular spectrometer would have provided sufficient sensitivity and resolution, but the LabRAM HR Evolution was used because it interfaced with the THMS600 temperature stage.

All Raman spectra were analyzed with custom MATLAB code. No averaging or baseline correction were used for this dataset. Cosmic rays and other anomalous spikes in the spectra were removed with a custom 6-sigma algorithm. The normalized intensity of the disorder band $\zeta_D(T)$

$$\zeta_D(T) = \frac{\left(\dfrac{\int_D I_R(v,T)dv}{\int_S I_R(v,T)dv}\right)}{\left(\dfrac{\int_D I_R(v,T_0)dv}{\int_S I_R(v,T_0)dv}\right)} \tag{36}$$

where T_0 is the temperature of the initial measurement and the regions D and S are bound by ±7 cm-1 of the peak (~15 cm^{-1}) and shoulder (~65 cm^{-1}) of the disorder band,

58

respectively. Linear interpolations for the two regions (above and below T_g) were performed with MATLAB. When performing Raman spectral band fitting, the data were corrected for filter and spectrometer roll-off by calibration with a broadband white light source in the region between ± 300 cm^{-1}. Then the data were normalized for Stokes scattering and fitted with the default nonlinear least squares method from the MATLAB curve fitting toolbox.

2.2.2 Differential Scanning Calorimetry (DSC) Measurements

Heat flow measurements were conducted by DSC with a TA Instruments Discovery Series DSC 2500; 5−10 mg samples were sealed in aluminum pans with hermetic lids and heated at various temperature rates. All DSC measurements were conducted under nitrogen with a 50 mL/min flow rate. All DSC thermograms were smoothed with a Gaussian window function and scaled with MATLAB. The T_g values were determined by the built-in analysis function in the TA Instruments TRIOS software package to determine the midpoint temperature. Typically heat-cool-heat experiments are used, which erase the thermal history of the sample with an initial heating ramp, impart a known thermal history with a cooling ramp, and heat the sample again with the result from the second heating ramp being reported. However, because the spectral analysis was performed with a single temperature ramp, we only focused on the initial DSC ramp. Polystyrene and PMMA were measured at a 10 °C/min heating rate, and PLA was measured at a 5 °C/min heating rate.

2.3 Results and Discussion

2.3.1 Normalized Disorder Band Intensity

Initially, we measured the Raman spectra of polystyrene using a 600 lines/mm diffraction grating and a 5-s integration time from -1100 to 1700 cm^{-1} with a total measurement time of 30 s per spectrum. The sample was heated from 70 to 150 °C with a 2 °C step size, and accounting for spectral acquisition time, this corresponded to an average ramp rate of ~4 °C/min. Figure 22 a shows an overlay of the 41 spectra acquired over the temperature range, with the inset highlighting the disorder band increase as a function of *T*. Figures 22 b and c show the normalized intensity of the Stokes and anti-Stokes shifted disorder band, $\zeta_D(T)$ with a clear change in slope at ~92 °C. Next, we measured polystyrene over a spectral range of -1060 to 1060 cm^{-1} with an 1800 lines/mm grating and an integration time of 30 s, resulting in a total acquisition time of 457 s per spectrum. The sample was heated from 20 to 198 °C with a 2 °C step size. Accounting for spectral acquisition time, this corresponded to an average ramp rate of ~0.25 °C/min. This provided an increase in both spectral and temperature resolution. The results shown in Figure 23 a and b again demonstrate an apparent change in slope in $\zeta_D(T)$ around ~90 °C, which correlates with the T_g midpoint of ~91 °C found by DSC (Figure 23 c).
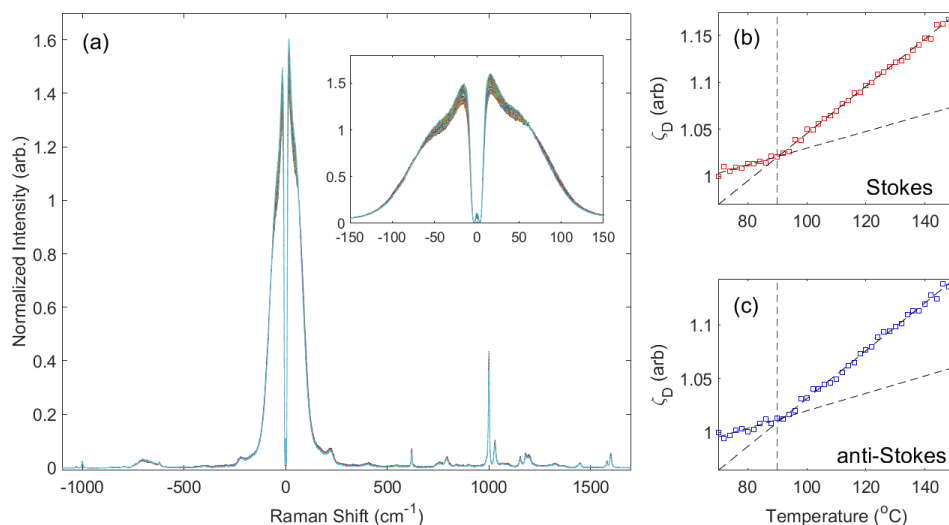
Figure 22. (a) Normalized Raman spectra of polystyrene from 70-150 °C with inset showing the low-frequency region. Temperature dependence of the normalized disorder band intensity for (b) Stokes and (c) anti-Stokes shifted Raman scattering.

To demonstrate the broad applicability of this method we also studied two additional polymers, PLA and PMMA. For PLA, we used a spectral range of -300 to 300 cm^{-1}, and an 1800 lines/mm grating with a 30-s integration time with a total measurement time of 129 s per spectrum, leading to an average ramp rate of ~0.32 °C/min for 1 °C step size. There is a kink in $\zeta_D(T)$ at ~62 °C (Figure 23 d and e). This correlates with the PLA T_g midpoint of ~62 °C found by DSC (Figure 23 f). For the PMMA sample, we used a spectral range of -330 to 330 cm^{-1}, an 1800 line/mm grating with a 60-s integration time, resulting in a total measurement time of 312 s per spectrum, with an average ramp rate of ~0.18 °C/min. The PMMA did not exhibit a strong kink in $\zeta_D(T)$ as observed in the other samples, but there is still a discernable change in slope at ~101 °C, as seen in Figures 23 g and h. This agrees with the PMMA T_g midpoint of ~101 °C determined by DSC (Figure

61

23 i). It is interesting to note that the relatively weak inflection in $\zeta_D(T)$ coincides with the DSC results where the transition is so weak that it was undetectable for heating rates below 10 °C/min.
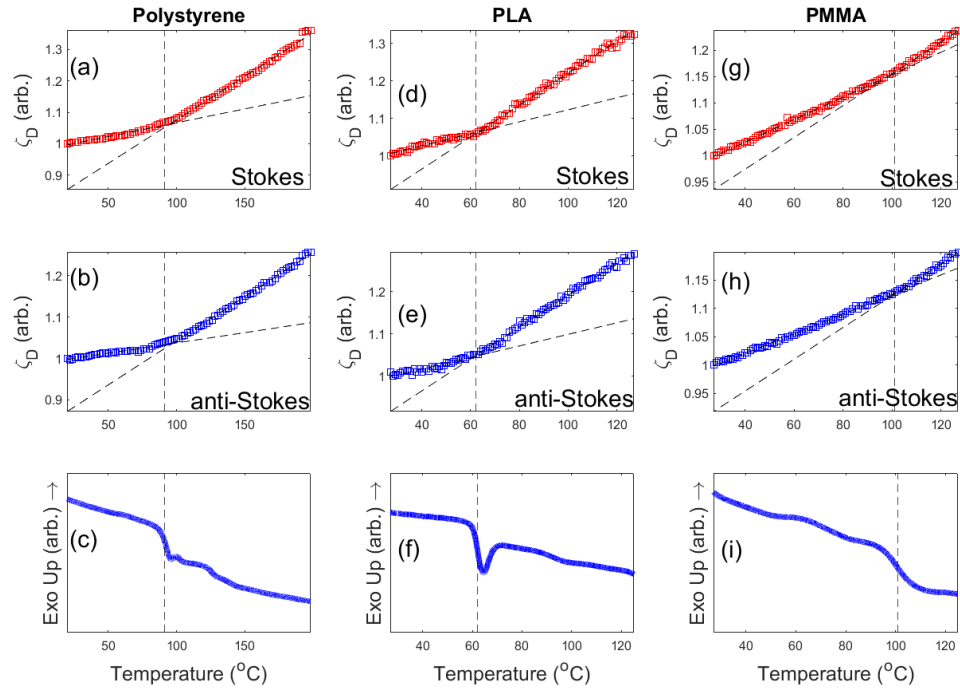
Figure 23. Temperature dependence of the normalized disorder band intensity for (a), (d), & (g) Stokes and (b), (e), and (h) anti-Stokes shifted Raman scattering and the DSC thermogram (c), (f), and (i) of polystyrene, PLA, and PMMA respectively.

2.3.2 Acoustic Phonon Contribution to Disorder Band

2.3.2.1 First Principles Peak Fitting Model. The Boson peak is defined as the maxima of the normalized phonon density of states, $\frac{g(v)}{v^2}$. While the origins of this feature are still debated in the community, extensive experimental evidence and more recent modeling have shown this feature to be extremely sensitive to sound velocity [60, 63,

118-123]. The van Hove peak in $g(\nu)$ originates from singularities that arrive at critical points in the Brillouin zone and is far less sensitive to sound velocity changes than the Boson peak [63, 97, 124, 125]. In addition to the pure Raman signal, there is also an additional contribution in the disorder band due to QERS [126]. The QERS arises from the translational energy associated with the molecules in the sample, resulting in a broadening of the Rayleigh band and can be modeled as a Lorentzian function centered at 0 cm^{-1}.

    All these factors combined contribute to the overall shape of the disorder band resulting in its broad asymmetric shape and well-defined shoulder. To investigate the relative contributions of these various physical phenomena to understand the correlation between the kink in the temperature dependence of $\zeta_D(T)$ and T_g, we modeled the spectral intensity $I(\nu)$ based on previous work comparing low-frequency Raman scattering and inelastic neutron scattering [67, 117].

$$I(\nu) = \frac{I_{QERS}}{2\pi} \frac{\Delta\nu_{QERS}}{\nu^2 + \left(\frac{\Delta\nu_{QERS}}{2}\right)^2}$$

$$+ \left\{ \frac{\gamma I_{BP}}{2\sqrt{\pi}\xi_{BP}} e^{-\left[\frac{1}{4\gamma^2} + \left(\frac{\gamma \log|\nu|}{\xi_{BP}}\right)^2\right]} + \frac{I_{NM}}{2\sqrt{\pi}\Delta\xi_{NM}} e^{-\left(\frac{\nu - |\xi_{NM}|}{2\Delta\xi_{NM}}\right)^2} \right.$$

$$\left. + \frac{I_\delta}{2\sqrt{\pi}\Delta\xi_\delta} e^{-\left(\frac{\nu - |\xi_\delta|}{2\Delta\xi_\delta}\right)^2} \right\} \left[H(\nu) + H(-\nu) \left(\frac{\nu_0 - \nu}{\nu_0 + \nu}\right)^3 e^{\left(\frac{h\nu}{kT}\right)} \right]. \tag{37}$$

where I is the integrated intensity of the mode, ν_0 the frequency of the incident radiation, $\Delta\nu$ the full width half maximum, and ξ the peak position, with the subscripts *QERS*, *BP*, *NM*, and δ denoting the four different contributions to the fit, namely QERS, Boson peak, normal modes, and bending mode, respectively, while γ is a constant relating to the skew

of the Boson peak. Consistent with previously published inelastic neutron scattering results [67], the normal modes arise from $g(v)$, including the van Hove peak in addition to any modes other than those due to the Boson peak. For this analysis, we are limiting our scope to polystyrene which has a skeletal deformation (bending) mode within the tail of the disorder band at ~220 cm^{-1}. It is important to note that contributions from skeletal deformation modes will vary by material as the location and number of deformation modes are not only polymer specific, but they can also vary with molecular weight and tacticity [102]. The relative strength of the Stokes and anti-Stokes shifted scattering signals is accounted for by the Boltzmann distribution due to thermal phonon populations and a cubic term in frequency due to the dipolar radiation. It should be noted that the radiative term is raised to the third power and not the fourth power because the signal from the camera in the spectrometer is proportional to the photon flux and not the absolute intensity [127].

Based on an observed Rayleigh filter cut-on of ± 7 cm^{-1} after intensity correction, we digitally applied a notch filter to both the measured spectrum and intensity fitting function (Equation 37). Since most of the QERS is contained within ± 7 cm^{-1}, fitting its contribution outside this region is inherently difficult so the upper bound of Δv_{QERS} was set to 0.5 cm^{-1} to ensure physically relevant results. The γ term was also bound between 0.5 and 2. All other fit parameters were unconstrained. Four representative fitted spectra of polystyrene (two measured below and two above T_g) are shown in Figure 24, with Boson peak positions of 11.7, 11.5, 9.8, and 8.7 cm^{-1} at 50, 60, 120, and 130 °C, respectively.
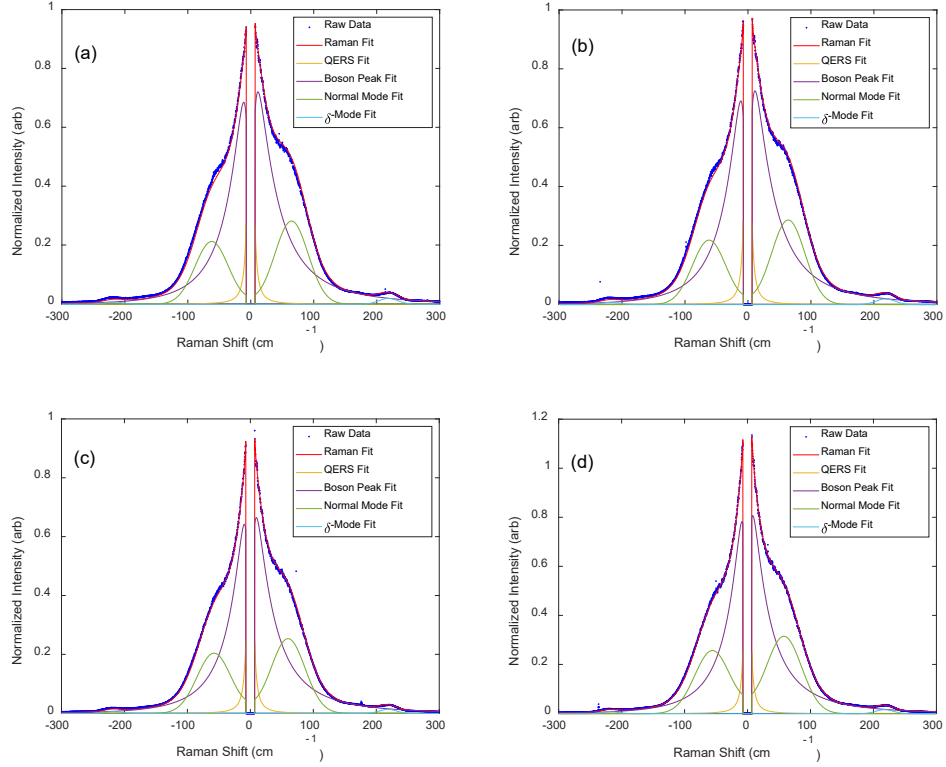
Figure 24. Intensity corrected Raman spectra (blue) fitted to the total intensity (red) as well as the associated QERS (yellow), Boson peak (purple), normal mode (green) and bending mode (cyan) contributions at (a) 50, (b) 60, (c) 120 and (d) 130 °C.

2.3.2.2 Photon Density of States. By summing the fitted contributions from the Boson peak and normal modes, we can isolate the spectral contribution from just $g(\nu)$. Using Equation 35, we can then re-normalize as follows,

$$\frac{I_{BP}(\nu) + I_{NM}(\nu)}{|\nu| \, [n(\nu, T) + H(\nu)]} \propto \frac{C(\nu)g(\nu)}{\nu^2}. \tag{38}$$

Studies have shown that $C(\nu)$ is a weakly varying function of ν.

Figure 25 shows the renormalized density of states, which remained relatively constant below T_g, and the average value Boson peak position over that range was 12 ± 0.2 cm^{-1}, in good agreement with the reported value of 11.5 cm^{-1} by Surovtsev and

Sokolov [99]. Above T_g, there is a redshift in the Boson peak, as expected with the decreased sound velocity. In addition, there is increased intensity from the renormalized density of states, which combines with the increased QERS from the softer material to produce the kink in $\zeta_D(T)$ at T_g.
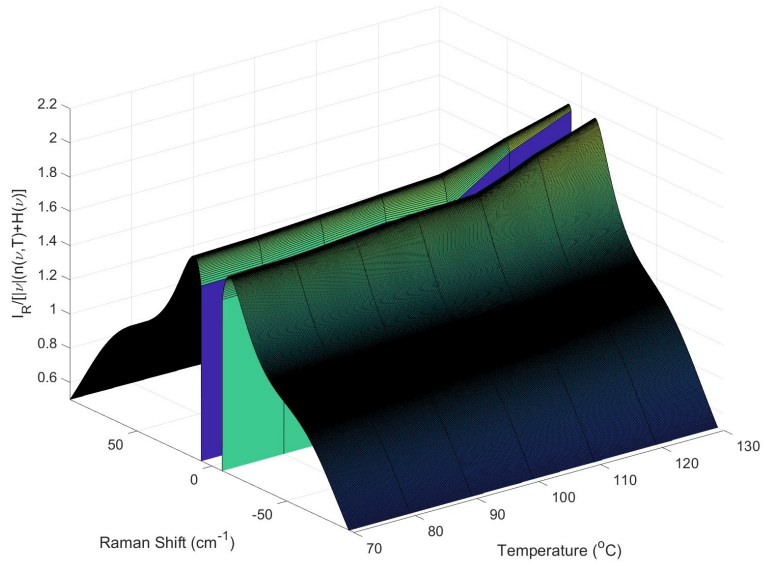
Figure 25. Temperature dependence of the re-normalized acoustic phonon contribution to polystyrene disorder band.

2.4 Conclusions

The disorder band feature in Raman spectra of amorphous materials is a combination of QERS and the Boson peak. While it is known that this disorder band increases as a material softens, we have demonstrated the ability to use this phenomenon to directly measure glass transition behavior using a compact fiber-coupled Raman probe without the need for advanced spectral processing. Rigorous analysis of the temperature dependent spectra can accurately identify T_g of polymers, but so too can simply

monitoring the temperature dependence of the integrated intensity near the apparent spectral peak ($\sim$15 cm^{-1}) normalized to that of the shoulder ($\sim$65 cm^{-1}).

The improved signal-to-noise in the low-frequency region of the Raman spectrum makes it far more promising for mainstream polymer characterization applications compared to conventional Raman focused on the chemical fingerprint region. Furthermore, the non-contact and high spatial resolution nature of Raman spectroscopy make this technique ideal for both micro-analysis and *in situ* process control applications. This is in stark contrast to DSC and DMA, neither of which are particularly suited for in-line process measurements or analysis of fibers and films. While this methodology produces similar results as those previously shown by Novikov *et al.* who monitored the intensity of the QERS normalized to the low-frequency Raman scatter [92], the use of the shoulder of the disorder band as a normalization for the low-frequency scattering greatly simplifies the instrumentation requirements, representing a major step toward widespread implementation of the technique.

Chapter 3

Method for Determining Resin Cure Kinetics with Low-Frequency Raman Spectroscopy

3.1 Abstract

Characterizing resin extent of cure kinetics is critical to understanding the structure-property-processing relationships of polymers. The disorder band present in the low-frequency region of the Raman spectrum is directly related to conformational entropy and the modulus of amorphous materials, both of which change as the resin polymerizes. Normalizing the disorder band to its shoulder (~85 cm^{-1}) provides structural conversion kinetics, which we can directly correlate to chemical conversion kinetics for methacrylate and epoxy-amine-based resin systems. In addition to fitting both the structural and chemical conversion data to a phenomenological kinetic rate equation, we also demonstrate a relationship between the chemical and structural kinetics, which appears to relate to the softness of the material. Lastly, we use the method to investigate a methacrylate/epoxy interpenetrating polymer network resin system. We find that the structural and chemical conversions occur simultaneously during the formation of the primary (methacrylate) network, but there is a lag between the two during the formation of the secondary (epoxy-amine) network.

3.2 Introduction

Resin kinetics inform polymerization extent of cure and processing conditions, which are central to polymer network formation. How the polymer network is formed influences the final physical and mechanical properties of the material, and insufficient curing can be detrimental to the material's performance [27, 128-131]. Thus, characterization of the kinetics is important for understanding the structure-property-processing relationships of polymers, which is essential for industrial process development and quality control [2]. Additionally, ensuring sufficient curing mitigates safety risks as unreacted monomers and other low molecular weight components could diffuse out of the material, causing adverse health effects. Cure kinetics are also important for determining adequate manufacturing times and establishing safe processing and storage conditions, especially in formulations that contain multicomponent reagents and initiators [3]. Because of the complexity of multicomponent resin systems, there is a need for chemically independent techniques that can be implemented *in situ* into manufacturing processes.

Many experimental techniques are used to monitor resin cure kinetics including changes in refractive index [132-134], rheology [135, 136], and dielectric analysis [137-139] although differential scanning calorimetry (DSC) and Fourier transform infrared (FTIR) spectroscopy are perhaps the most widely implemented. DSC exposes a sample to a thermal profile and measures the heat flow during the curing process [6-10]. Monitoring kinetics with DSC assumes that the heat evolved is proportional to the extent of cure of reactive groups and that the reaction rate is proportional to the measured heat flow [7]. Similarly, photo-DSC monitors the heat release of photocurable resins after being

irradiated with UV or visible light [2-5]. In both DSC and photo-DSC, factors such as the

method of sample preparation, the heating rate of the DSC test, and specificity of

temperature integral approximation can have effects on the calculations and results [7,

140]. Photo-DSC is also limited by the relatively long delay times due to the required

low-intensity light [2].

FTIR is used for monitoring the kinetics of both thermal and photocurable

systems and provides chemical information about the resin as the absorption band is

proportional to the bond concentration [2, 3, 141]. In many cases, FTIR involves

attenuated total reflection (ATR), which requires direct sample contact [131, 142-144].

This technique is useful for surface measurements but cannot provide information of a

sample's interior nor is it suitable for *in situ* monitoring applications. Alternatively,

conversion of the bulk polymer can be monitored in the near-IR range through

transmission measurements, which can be adapted for in-line process monitoring [145-

148]. While effective for monitoring both physical and chemical properties of polymers,

near-IR spectra contain overlapping overtones and combinations of bands from the mid-

IR that often require nontrivial post-processing and chemometric data analysis [149,

150].

Raman spectroscopy has been used to study the real-time kinetics of different

polymerization reactions such as those of microemulsions and epoxy resin systems [130,

151-153]. Raman is a sensitive probe of nonpolar molecules, and as a noncontact, non-

destructive technique, it is suitable for *in situ* monitoring of cure kinetics. Raman spectra

can be subdivided into three main regions known as the stretch region (>2000 cm^{-1}), the

chemical fingerprint region (~500 cm^{-1} – ~2000 cm^{-1}), and the structural region (<500

cm^{-1}). However, thus far, Raman-based polymerization kinetics studies have focused

exclusively on signals in the chemical fingerprint region [130, 151, 152], such as the

methacrylate (C=C) band at ~1640 cm^{-1} and the epoxy band (CH-O-CH$_2$) at ~1250 cm^{-1}.

Raman scattering in the low-frequency (terahertz) region, which is contained within the

structural region, is directly related to the phonon density of states $g(v)$ [99, 108, 117,

154]. In highly ordered crystalline materials, acoustic phonon modes produce sharp bands

in the Raman spectrum, but as the material becomes less ordered, these modes tend to

broaden and redshift simultaneously. For soft amorphous materials, $g(v)$ is dominated by

two main features – the Boson and van Hove peaks [63, 95, 106-114]. In amorphous

polymers, the Raman scattering intensity $I_R(v)$ can be directly related to $g(v)$ by

Equation 35 [42, 99, 115-117, 154].

In the previous chapter we have previously shown that these phonon modes result

in a broad (~150 cm^{-1} wide) disorder band in polymers with an apparent peak near 15

cm^{-1} and a well-defined shoulder dominated by the Boson and van Hove peaks,

respectively [154]. In that work, we showed that by normalizing the disorder band to the

shoulder, the integrated intensity near the peak of the disorder band could be used to

measure the effective change in conformational entropy as a polymer goes through the

glass transition, without the need for advanced spectral processing or peak fitting.

In this chapter, we describe how this same methodology can be applied to

measure polymerization kinetics by monitoring the decrease in the normalized disorder

band as a resin polymerizes. Since the disorder band in soft amorphous materials is a

universal feature, this approach benefits from combining the "chemically agnostic"

nature of traditional thermal-mechanical analysis methods with the non-contact, non-

destructive nature of laser-based vibrational spectroscopy. Herein, we demonstrate the universality of this technique by detecting transient structural changes during the curing process of methacrylate, epoxy-amine, and dual-cure methacrylate/epoxy interpenetrating polymer network (IPN) resins.

3.3 Materials and Methods

3.3.1 Materials and Sample Preparation

Three resins were formulated for this study to represent a wide array of materials: fully methacrylate, epoxy-amine, and methacrylate/epoxy. Resins were prepared such that the methacrylate functionalities polymerized via photoinitiated free radical polymerization, and the epoxy-amine components cured thermally. Figure 26 shows the components of each resin formulation. All components were used as received in this study.
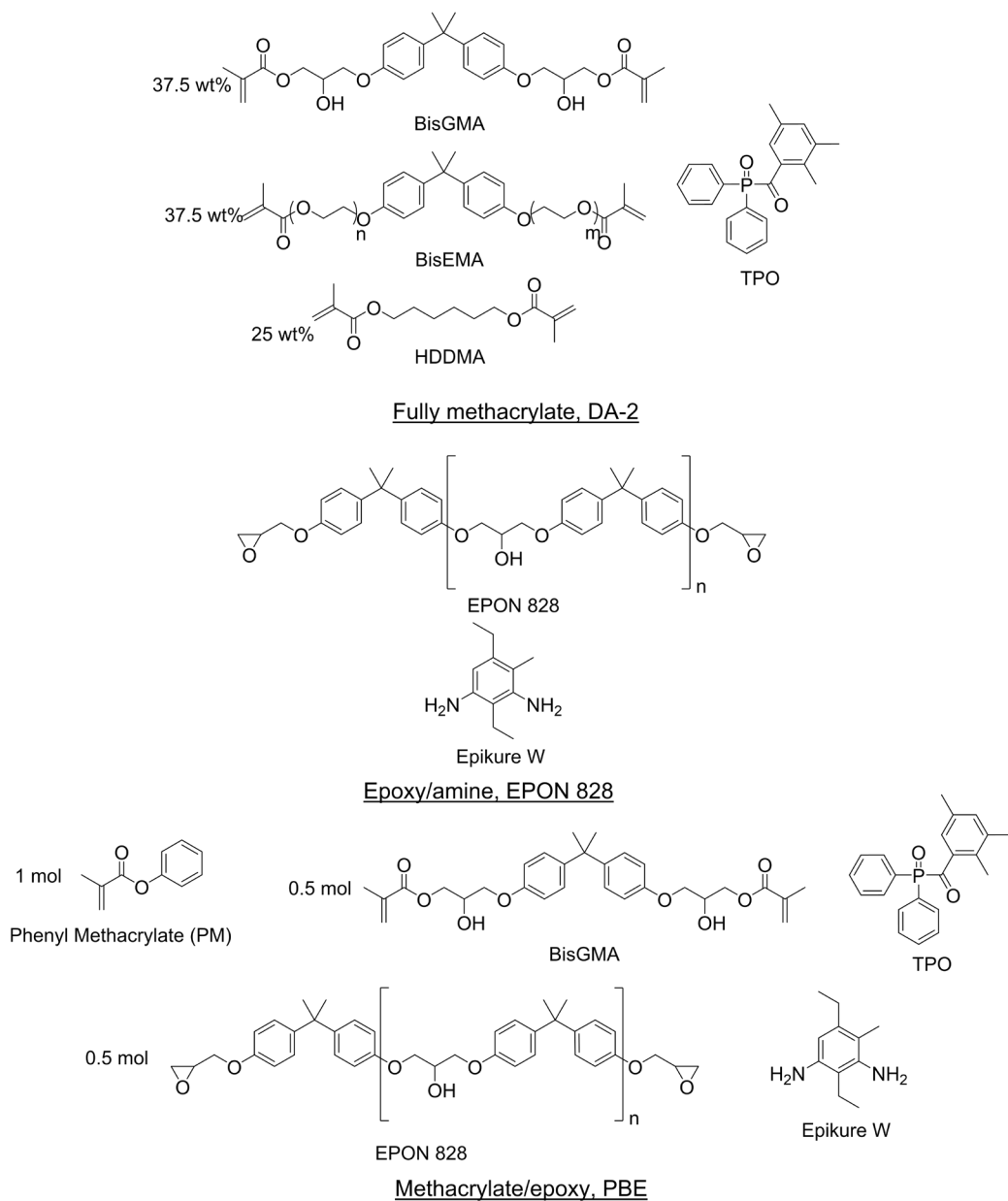
Figure 26. Structures of resin formulations.

A fully methacrylate resin (DA-2) was prepared from 37.5 wt% bisphenol A glycerolate dimethacrylate (BisGMA, Esstech), 37.5 wt% ethoxylated bisphenol A dimethacrylate (BisEMA, Esstech), and 25 wt% 1,6-hexanediol (HDDMA, Esstech)

73

according to Tu *et al.* [18]. Diphenyl(2,4,6-trimethylbenzoyl)phosphine oxide (TPO, TCI America) was added as a photoinitiator at 2 wt% based on the total mass of resin.

An epoxy-amine resin was prepared from a diglycidyl ether of bisphenol A resin (EPON 828, Hexion) and a diethylmethylbenzenediamine resin (Epikure W, Hexion). The epoxy equivalent weight (EEW) for EPON 828 was 186.1 g/eq and the amine hydrogen equivalent weight (AHEW) of Epikure W was 44.6 g/eq. These components were formulated with 1:1 equivalents of epoxide to amine hydrogen. The epoxy-amine resin is herein referred to as EPON 828.

A dual-cure methacrylate/epoxy IPN resin was prepared by combining methacrylate and epoxy-amine resin components. The epoxy-amine component was prepared with EPON 828 and Epikure W with 1:1 equivalents of epoxide to amine hydrogen. Phenyl methacrylate (inhibited with 100 ppm of hydroquinone, Scientific Polymer Products), BisGMA, and the epoxy-amine were formulated based on 1:0.5:0.5 molar equivalents, respectively. This resin formulation is denoted as PBE. TPO was added as the photoinitiator at 2 wt% based on the total resin.

All resin formulations were mixed with an ARE-310 planetary mixer (Thinky) programmed for 10 min at 2000 rpm to mix and 5 min at 2200 rpm to defoam. This mixing cycle was repeated until all components were fully dispersed homogenously (2-3 cycles). After mixing a given formulation, resin was applied onto a $4 \times 6 \times 0.020$ in^3 steel test panel and spread with an adjustable film coater set to a thickness of 500 μm. A $25 \times 25 \times 0.15$ mm^3 glass cover slip was then placed on top of the resin to mitigate oxygen inhibition at the surface, and the excess resin was removed.

3.3.2 Experimental Setup

The experimental setup, shown schematically in Figure 27, enabled *in situ* real-time polymerization kinetics monitoring of photo, thermal, and sequential photo-thermal cure. This was accomplished with a 0.25-in thick aluminum plate with an embedded thermocouple seated on top of a hot plate as the sample platform. Light from an Omnicure Series 2000 high-power mercury vapor source (Excelitas Technologies) was passed through a 365-nm bandpass filter, fiber-coupled to a large core "light pipe" and then collimated directly above the sample platform to allow for relatively uniform illumination of the resins. The Raman scattering measurements were done with a 785-nm CleanLine laser and TR-PROBE from Coherent Inc. with a 37.5-mm focal length aspheric lens for both excitation and collection. The TR-PROBE can filter both Stokes and anti-Stokes Raman scattering to within approximately ± 7 cm^{-1} of the Rayleigh line. The scattered light was then fiber-coupled directly into an EAGLE Raman-S (Ibsen Photonics) high-throughput transmission (f/1.6) spectrograph. Raman scattered light was collected with a deep depleted back-illuminated thermoelectrically cooled (-60 °C) CCD camera (Andor Instruments) with a 950-ms integration time. The UV illumination intensity was controlled by a combination of lamp settings and adjustments to the height between the collimating lens and the sample platform, and the light intensities were measured with a Thorlabs power meter.
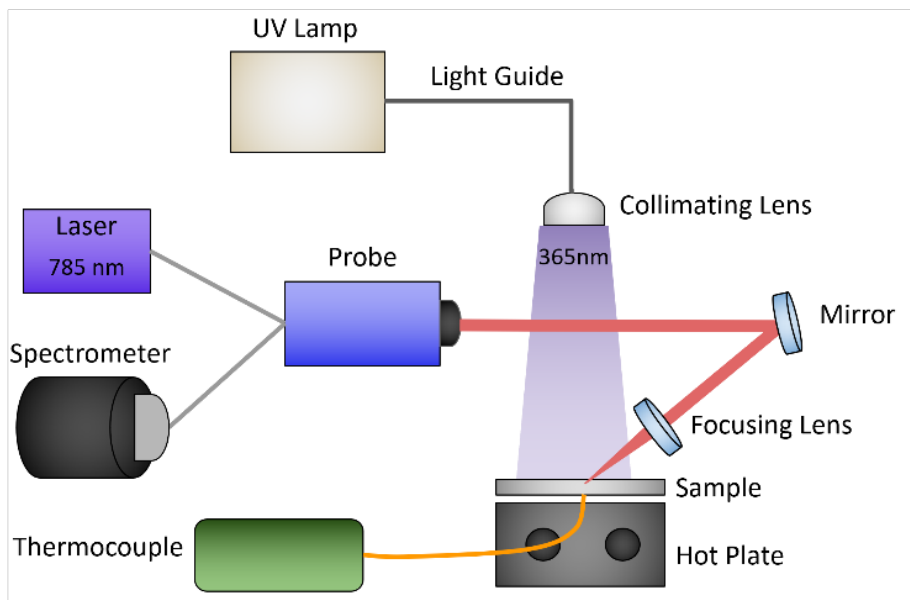
Figure 27. Schematic representation of Raman kinetics experimental setup.

3.3.3 Data Processing and Analysis

All Raman spectra were analyzed with custom MATLAB code, which included an adaptive, iteratively reweighted Penalized Least Squares algorithm for baseline correction for data in the chemical fingerprint region. No baseline correction was needed in the structural region. Cosmic rays and other anomalous spikes in the spectra were removed with a custom 6-sigma algorithm. The conversion α was calculated from the following relationship,

$$\alpha = \frac{\left(\frac{I_{var}}{I_{ref}}\right)_{unreacted} - \left(\frac{I_{var}}{I_{ref}}\right)_{reacted}}{\left(\frac{I_{var}}{I_{ref}}\right)_{unreacted}} \tag{39}$$

where the regions I_{var} and I_{ref} are the integrated intensities of the variable and reference peaks respectively. For structural "conversion", the variable and reference peaks were chosen to be the peak ($\sim$14 cm^{-1}) and shoulder ($\sim$85 cm^{-1}) of the disorder band,

76

respectively. For the fingerprint region, the variable and reference peaks varied according to the polymer. For methacrylate kinetics, the variable and reference peaks were the aromatic CCH quadrant stretch (~1605 cm^{-1}) and the C=C stretch (~1637 cm^{-1}), respectively [90]. For epoxy-amine kinetics, the variable and reference peaks were the epoxy ring breathing mode (~1250 cm^{-1}) and the phenyl band (~1109 cm^{-1}), respectively [152]. All integrated intensities were determined with bounds of ±7 cm^{-1} of the line center.

Conversion data were fit with linear least squares regression to the integrated form of the following kinetic rate equation:

$$\frac{d\alpha}{dt} = k(\alpha_u - \alpha)^n \tag{40}$$

where α_u is the ultimate conversion, k is the rate constant, and n is the reaction order. [131] While the authors acknowledge that there are more comprehensive kinetic rate equations for epoxy-amine resin systems [155], our purpose is to show the applicability of the method and not to provide a detailed physical description of the cure itself. Therefore, we have chosen to use this relatively simple phenomenological model in this study.

When performing Raman spectral band fitting, the data were corrected for filter and spectrometer roll-off by calibration with a broadband white light source in the region between ±200 cm^{-1}. Then the data were normalized for Stokes scattering and fitted to Equation 37, with $I_\delta \to 0$ since there were no observable bending modes in the region of interest. The fit was done with the default nonlinear least squares method from the MATLAB curve fitting toolbox.

3.4 Results and Discussion

3.4.1 UV Cured Methacrylate Resin

First, we chose to look at the cure kinetics of the DA-2 formulation since it had

been previously studied with ATR-FTIR by Tu *et al*. [131]. Figure 3(a) shows the

methacrylate conversion based on the Raman results from the chemical region for

measurements done with a 365-nm light source with an illumination intensity of 0.76

mW/cm^2. An unconstrained fit of the chemical conversion data resulted in $\alpha_u = 0.79$,

$k = 0.09$, and $n = 4.3$ with a sum square error, *SSE*, of 0.59. The previous FTIR analysis

of DA-2 with 0.7 wt% phenylbis(2,4,6-trimethylbenzoyl)phosphine oxide as the

photoinitiator, under various illumination intensities at a wavelength of 405-nm yielded

$\alpha_u = 0.74$ and $n = 4.4$. The k values cannot be directly compared as the previous

analysis modified the rate constant by including an intensity dependent prefactor in the

kinetic rate equation: $\frac{d\alpha}{dt} = I_E^{\omega} \, k(\alpha_u - \alpha)^n$, where I_E is the light intensity and ω the dose

rate exponent with a reported value of 0.71. [131]
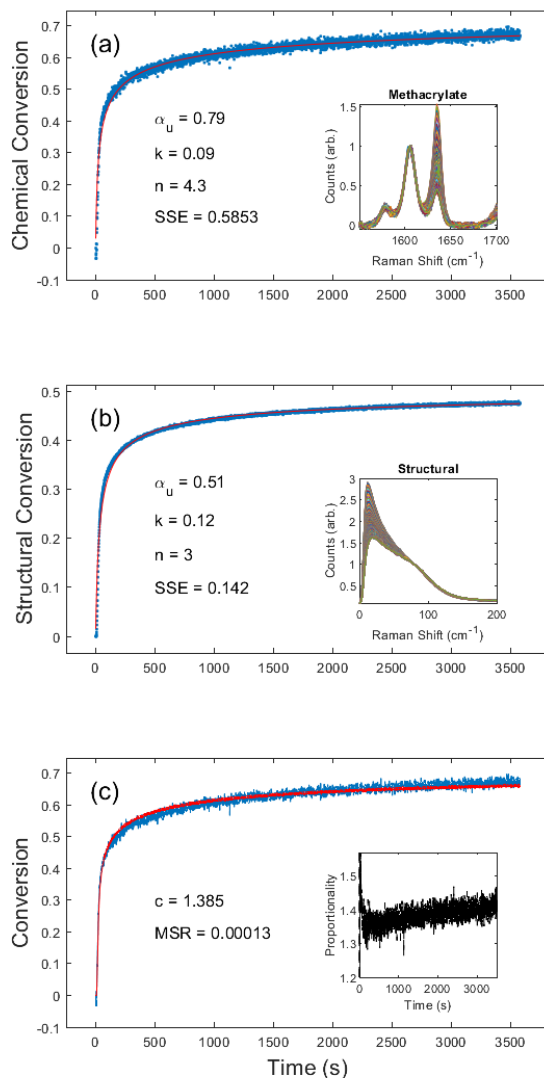
Figure 28. DA-2 photocure kinetics obtained from (a) the chemical region of the Raman spectrum with inset showing the methacrylate (variable) and phenyl (reference) peak and (b) the structural region with inset showing the normalized disorder band. (c) displays an overlay of the chemical conversion kinetics and the structural kinetics scaled by $c = 1.39$, with the inset showing the proportionality across the entire cure. In (a) and (b) the blue dots represent measured values and the red line the fitted curve. In (c) the blue line represents the methacrylate chemical conversion, and the red line represents the proportionality corrected structural conversion.

Visual inspection of the structural kinetics data (Figure 28b) clearly shows the same general shape of the curve, with an improved signal-to-noise ratio. It should be noted that an unconstrained fit produced kinetic constants of $\alpha_u = 0.51$, $n = 3.0$, and $k = 0.12$ with an *SSE* of 0.14, which do not match the chemical kinetics values. This is not unexpected since chemical conversion is a direct measure of monomer polymerization whereas structural conversion reflects the change in phonon dispersion. Therefore, the conversion values do not have the same physical meaning in structural kinetics as they do in chemical kinetics. However, as shown in Figure 3c, there is a scaling factor $c = 1.39$ between the chemical and structural conversion curves of DA-2 with a mean square residual *MSR* of 0.0001. Over the course of 12 different DA-2 experiments (see Table 2) with light intensities ranging from 0.22 – 1.08 mW/cm^2 we found the scaling constant was robust with a value of $c = 1.40 \pm 0.02$. That is, while the kinetic constants appear to be significantly different, the curves only differ by a scaling factor due to the differences in what is being probed.

Table 2

Summary of Kinetic Fit Results for DA-2 Resin System

Light Intensity (mW/cm²)	Chemical				Structural				c	MSR
	α_u	k	n	SSE	α_u	k	n	SSE		
1.02	0.79	0.20	4.24	0.58	0.51	0.26	3.00	0.75	1.41	0.0002
1.02	0.81	0.13	4.40	0.45	0.51	0.16	3.00	0.11	1.43	0.0002
1.08	0.80	0.12	4.30	0.92	0.50	0.16	2.90	0.14	1.43	0.0003
0.76	0.79	0.09	4.30	0.59	0.51	0.12	3.00	0.14	1.39	0.0001
0.76	0.79	0.12	4.25	0.70	0.51	0.18	3.10	0.13	1.41	0.0002
0.76	0.77	0.09	3.96	0.67	0.50	0.13	2.90	0.15	1.40	0.0002
0.50	0.75	0.08	3.70	0.68	0.50	0.09	2.80	0.18	1.40	0.0001
0.50	0.76	0.08	3.90	0.83	0.50	0.09	2.80	0.20	1.39	0.0001
0.50	0.76	0.08	3.90	0.64	0.51	0.12	3.10	0.17	1.40	0.0001
0.22	0.70	0.04	3.00	1.05	0.49	0.05	2.60	0.32	1.39	0.0002
0.22	0.69	0.04	2.94	1.00	0.49	0.05	2.60	0.32	1.38	0.0001
0.23	0.69	0.03	3.00	1.66	0.48	0.04	2.50	0.39	1.36	0.0002

3.4.2 Thermally Cured Epoxy-Amine Resin

Next, we investigated the EPON 828 thermally cured at 180 °C. Results shown in Figure 4 clearly demonstrate the ability to generate both chemical and structural conversion curves. Unconstrained fitting produced kinetic constants of $\alpha_u = 0.88$, $k = 0.002$, and $n = 1.2$ for the chemical conversion, and $\alpha_u = 0.58$, $k = 0.01$, and $n = 2.1$ for the structural conversion. Due to the combination of low Raman scattering efficiency and the broad overlapping shape of peaks in this region, the chemical conversion is inherently noisy (Figure 29a) with a large *SSE* of 24.11. By contrast, the noise in the structural conversion data (Figure 29b) is comparable to that of the data of the UV-cured resin system. Figure 4c gives $c = 1.57$ for the two curves with an *MSR* of 0.0025,

further demonstrating the self-consistency between the chemical and structural kinetics. It should be noted that, unlike the DA-2 resin where the proportionality constant settled in under 1 min, the EPON 828 took nearly 15 min before the proportionality constant stabilized. Over the course of 10 different experiments (see Table 3) with the EPON 828 system with ~180 °C cure temperature, the average proportionality constant was $c = 1.71 \pm 0.26$.

Table 3

Summary of Kinetic Fit Results for EPON 828 Resin System

Temperature (ºC)	Chemical				Structural				c	MSR
	α_u	k	n	SSE	α_u	k	n	SSE		
185.80	0.82	0.00143	1.08	46.22	0.48	0.00752	1.00	3.50	1.59	0.0225
181.20	0.82	0.00173	1.30	85.35	0.53	0.00720	2.08	0.44	1.56	0.0132
180.50	0.85	0.00297	1.24	72.44	0.62	0.00601	1.42	0.60	1.32	0.0110
180.80	0.88	0.00229	1.17	10.76	0.44	0.00455	1.47	0.16	1.99	0.0019
175.30	0.86	0.00215	1.07	5.65	0.40	0.01252	1.79	0.50	2.13	0.0381
175.10	0.90	0.00328	1.44	7.12	0.46	0.00691	1.64	0.07	1.95	0.0013
180.50	0.86	0.00415	1.45	42.86	0.59	0.03279	2.46	0.09	1.49	0.0131
176.80	0.90	0.00316	1.53	3.05	0.45	0.00750	1.46	0.40	1.90	0.0031
174.50	0.90	0.00280	1.29	15.56	0.54	0.00623	1.68	0.07	1.66	0.0023
180.00	0.88	0.00224	1.29	24.35	0.57	0.00667	1.79	0.08	1.55	0.0040
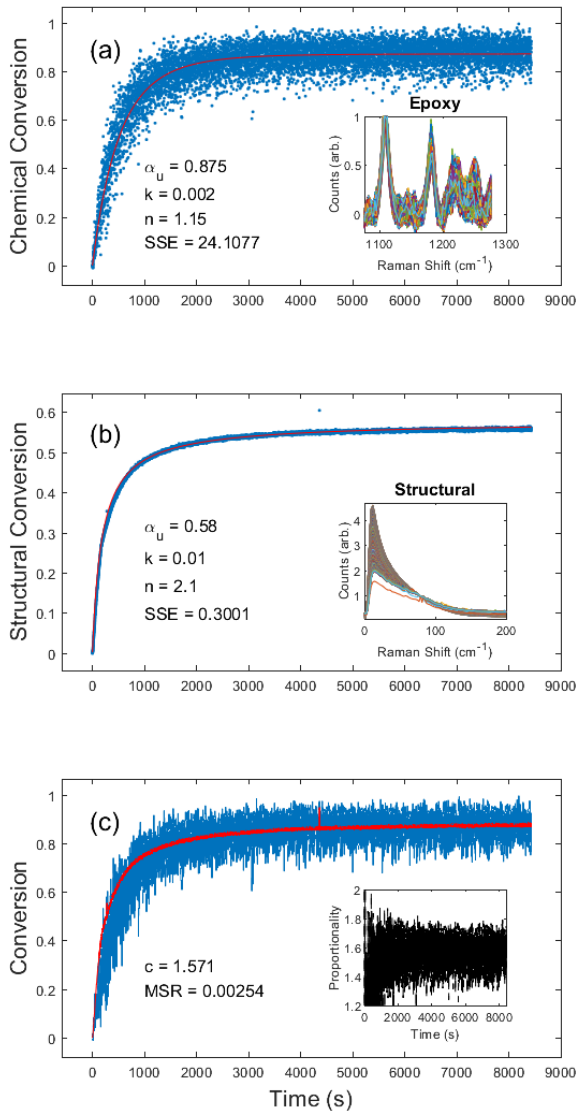
Figure 29. EPON 828 thermal cure kinetics obtained from (a) the chemical region of the Raman spectrum with inset showing the epoxide (variable) and phenyl (reference) peaks; (b) the structural region with inset showing the normalized disorder band; and (c) an overlay of the chemical conversion kinetics and the structural kinetics scaled by $c = 1.57$, with the inset showing the proportionality across the entire cure. In (a) and (b) the blue dots represent measured values and the red line the fitted curve. In (c) the blue line represents the methacrylate chemical conversion, and the red line represents the proportionality corrected structural conversion.

During many of the EPON 828 cure kinetics experiments, there was an initial dip in the structural conversion region, which was not reflected in the chemical conversion kinetics. We hypothesize that this is due to an initial drop in viscosity (modulus) when the sample was rapidly heated from room temperature to 180 °C. Further rheological studies are needed to test this hypothesis (see Chapter 4). To accurately calculate the proportionality constant c when necessary, the kinetics data were truncated to remove the initial dip. Figure 30 shows a representative example of the workflow for an EPON 828 resin thermally cured at 180 °C. Figure 30a shows the chemical and structural conversion when the initial data points are used, with Figure 30b showing a zoomed-in view of the dip with the black line indicating the truncation point at 80 s. All truncation points were determined by visual inspection and typically ranged from ~60 s – ~100 s. Figure 30c shows the overlays of the recalculated conversion data post-truncation, and figure 30d shows the overlays after the structural data was scaled by $c = 1.68$.
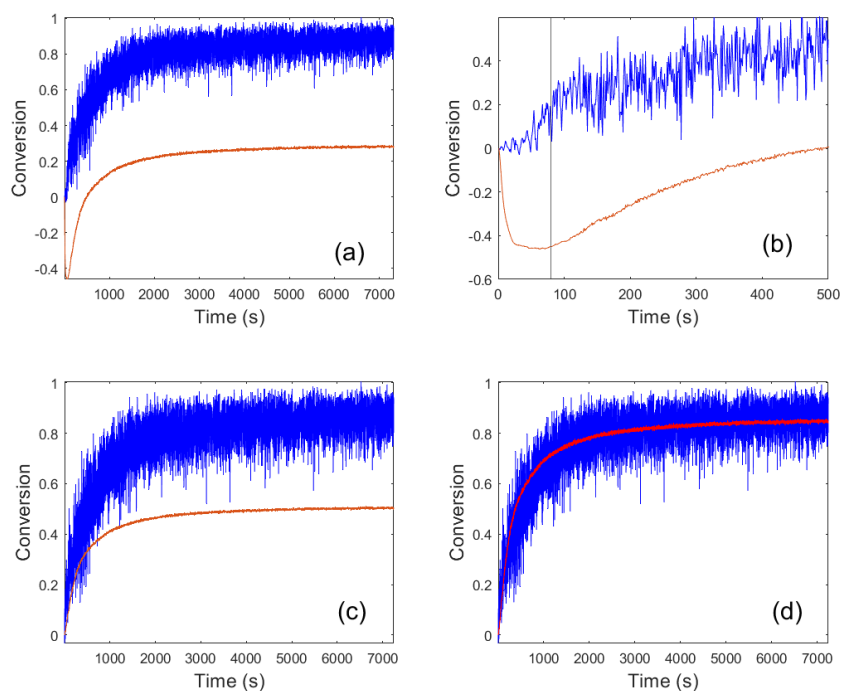
Figure 30. Chemical (blue) and structural (red) conversion kinetics of an EPON 828 resin thermally cured at 180 °C. (a) Complete kinetic profiles, (b) first 500 s of the cure with the vertical black line indicating the inflection point in structural kinetics, (c) recalculated conversion profiles after truncation, and (d) an overlay of the chemical conversion kinetics and the structural kinetics scaled by $c = 1.68$.

Upon peak fitting, we determined the relative contributions to the disorder band from the quasi-elastic Rayleigh scattering, Boson peak, and normal mode dominated by the van Hove peak [67, 154]. Figure 31 shows the fitted results at the end of the cure for both resin formulations, clearly demonstrating the simultaneous blueshift and decrease in the Boson peak after cure. It is important to note that EPON 828 is softer than the DA-2, with the two polymers having reported storage moduli of 2.1 GPa and 3.0 GPa, respectively [18, 156] ,and EPON 828 is cured at elevated temperatures, further softening

it which accounts for the difference in the final Boson peak locations: 12 cm^{-1} for EPON 828 and 16 cm^{-1} for DA-2. Nonetheless, these differences in the phonon dispersion have no noticeable impact on the applicability of this method to measure the polymerization of the two resin systems, but the difference in moduli likely contributes to the difference in the c values between the two resin systems.
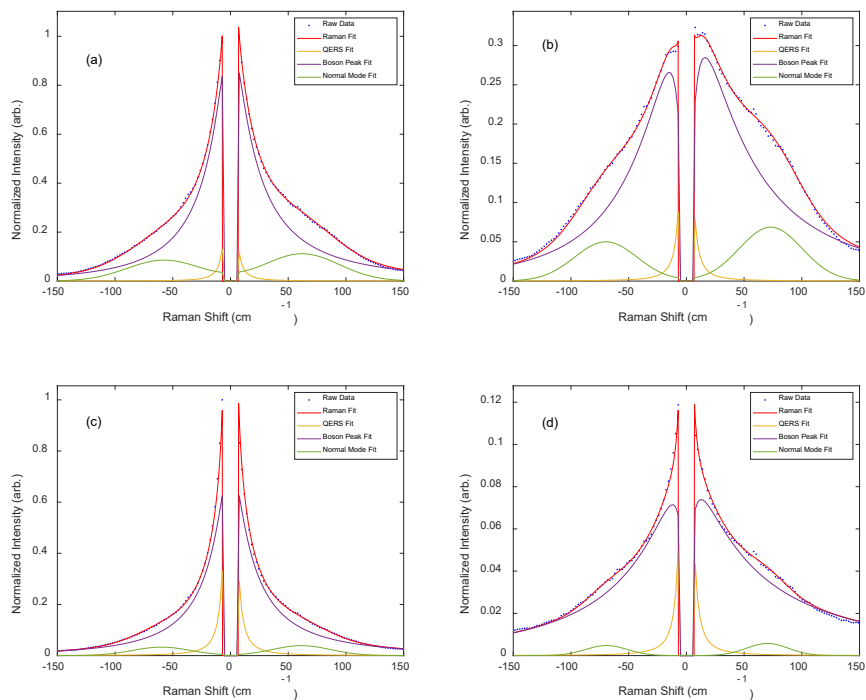
Figure 31. Intensity corrected Raman spectra (blue) fitted to the total intensity (red) as well as the associated QERS (yellow), Boson peak (purple), and normal mode (green) contributions for DA-2 pre (a) and post cure (b) and EPON 828 pre (c) and post cure (d).

3.4.3 Dual-Cure IPN Resin

Lastly, to investigate the universality of the method, we analyzed the PBE dual-functional IPN resin system. Figure 32 shows the results of both the methacrylate, epoxy,

and structural conversions at room temperature over a 1-h exposure to 365-nm light with an intensity of 1.01 mW/cm^2. Using the same methodology as the previous resin, we were able to measure both chemical (methacrylate and epoxy) and structural conversion. Unconstrained fitting produced kinetic constants of $\alpha_u = 0.76$, $k = 0.01$, and $n = 1.8$ for the methacrylate chemical conversion, and $\alpha_u = 0.40$, $k = 0.02$, and $n = 2.0$ for the structural conversion. As expected, there was no observable epoxy chemical conversion (Figure 32b). Both the methacrylate chemical and structural conversion fits had a relatively low *SSE* of 1.92 and 0.24, respectively. However, upon visual inspection of Figures 32a and 32c, it is obvious that below 500 s, the fit is not as good as those in the other two resin systems, resulting from the relatively long inhibition time (higher activation energy) of the PBE resin. Both fits could have been improved by accounting for inhibition, but that was beyond the scope of this chapter.
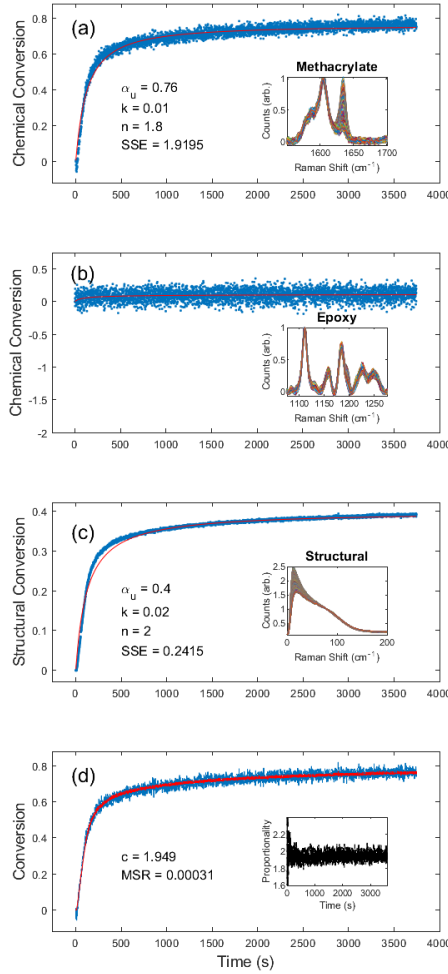
Figure 32. PBE photocure kinetics obtained using (a) the methacrylate chemical region of the Raman spectrum with inset showing the methacrylate (variable) and phenyl (reference) peaks; (b) the epoxy chemical region of the Raman spectrum with inset showing the epoxied (variable) and phenyl (reference) peaks; (c) the structural region with inset showing the normalized disorder band; and (d) an overlay of the chemical conversion kinetics and the structural kinetics scaled by $c = 1.95$, with the inset showing the proportionality across the entire cure. In (a), (b), and (c) the blue dots represent measured values and the red line the fitted curve. In (d) the blue line represents the methacrylate chemical conversion, and the red line represents the proportionality corrected structural conversion.

88

Figure 32d shows that for the methacrylate fingerprint and structural conversion curves $c = 1.95$ with an *MSR* of 0.0003. Over the course of 14 different PBE experiments (see Table 4) with light intensities ranging from $0.21 – 1.03$ mW/cm^2, we found $c = 1.98 \pm 0.02$. In addition to further validating the self-consistency between the chemical and structural conversions, this is also in accord with our hypotheses regarding the correlation between the modulus and the proportionality constant. Since the PBE resin was not thermally post-cured, the epoxy-amine network was not able to form, resulting in a significantly softer material and, therefore, a higher proportionality constant. Upon peak fitting, the final Boson peak position of the photocured PBE resin was determined to be 16 cm^{-1}, which is identical to the results of the fully methacrylate DA-2 resin.

Table 4

Summary of Kinetic Fit Results for PBE Resin System

Light Intensity (mW/cm^2)	Chemical				Structural				c	MSR
	α_u	k	n	SSE	α_u	k	n	SSE		
1.01	0.76	0.01	1.80	1.92	0.40	0.02	2.00	0.24	1.95	0.0003
1.04	0.78	0.01	1.60	2.54	0.39	0.02	1.70	0.29	2.01	0.0004
1.00	0.83	0.02	2.40	2.11	0.40	0.03	2.00	0.34	2.01	0.0003
0.73	0.77	0.01	1.90	2.11	0.38	0.01	1.50	0.30	1.97	0.0004
0.74	0.79	0.01	1.80	2.82	0.40	0.02	1.90	0.40	1.98	0.0004
0.75	0.78	0.01	1.70	2.76	0.39	0.01	1.40	0.36	1.97	0.0004
0.48	0.77	0.01	1.80	4.47	0.39	0.02	1.90	0.38	1.98	0.0009
0.50	0.79	0.01	2.00	3.19	0.39	0.01	1.60	0.46	2.01	0.0004
0.49	0.80	0.01	2.10	3.70	0.39	0.01	1.30	0.50	1.97	0.0004
0.49	0.80	0.01	2.20	4.86	0.39	0.01	1.60	0.48	1.94	0.0005
0.53	0.78	0.01	1.65	2.48	0.39	0.01	1.40	0.44	1.98	0.0003
0.22	0.80	0.01	3.00	12.21	0.44	0.01	2.40	1.55	1.94	0.0007
0.21	0.83	0.01	2.54	8.37	0.40	0.01	1.80	1.10	1.99	0.0003
0.21	0.82	0.01	2.90	15.46	0.41	0.01	2.10	1.72	1.96	0.0005

Lastly, we evaluated the PBE resin through the entire dual cure process. First it was photocured with an illumination intensity of 1.02 mW/cm² for 1 h, at which time the UV lamp was turned off, and data collection was paused. The sample was removed while the stage was heated to 180 °C. The sample was then placed back on the temperature stage, and data collection was resumed for 2 h, simulating a traditional post-cure in a preheated oven. Figure 33 shows the change in the spectral weight of the disorder band, which reflect the kinetics of both the UV and thermal cures. The sizeable negative step discontinuity in the data is due primarily to the temperature dependence of the low-frequency Raman signal, as shown in Figure 33. However, there may also be additional contributions due to uncertainty in sample placement during the thermal cure.
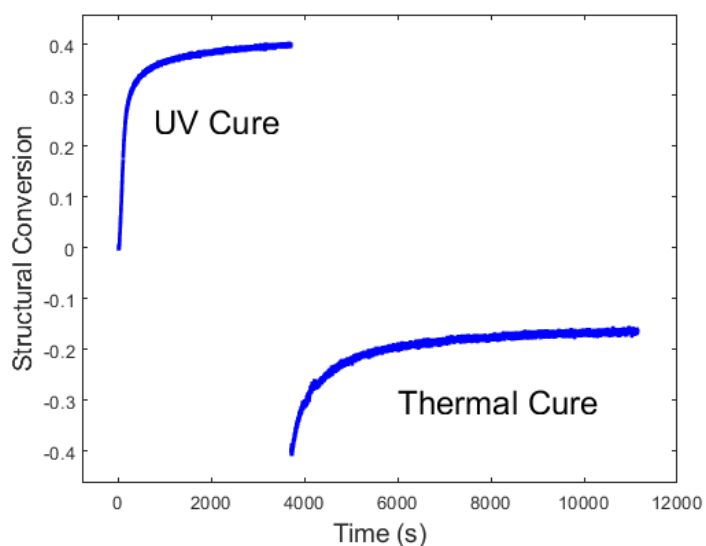
Figure 33. PBE dual UV-thermal cure kinetics obtained from the structural region.

We independently analyzed the UV and thermal cure regions to gain a deeper insight into the cure kinetics. During the photocure, no measurable conversion was

present from the epoxy. The kinetic constants from the methacrylate chemical conversion were $\alpha_u = 0.79$, $k = 0.010$, and $n = 1.83$ with an *SSE* of 1.72, and the kinetic constants from the structural conversion were $\alpha_u = 0.39$, $k = 0.010$, and $n = 1.4$ with an *SSE* of 0.34. We also determined that the methacrylate-to-structural proportionality constant was $c = 1.97$. As expected, these results are extremely close to those shown in Figure 32.

The thermal cure kinetics unveiled several interesting kinetic processes beyond simple epoxy-amine polymerization. One interesting observation is additional methacrylate polymerization during the first 500 s of the thermal cure (Figure 34a). We believe this may result from increased chain mobility above the glass transition temperature and increased internal energy allowing the release of trapped free radicals from dissolved oxygen. We were able to determine kinetic constants for the additional methacrylate conversion of $\alpha_u = 0.3$, $k = 0.010$, and $n = 1.35$; although it should be noted that the data were quite noisy, resulting in an *SSE* of 81.6048. Still, an additional cure of 0.3 indicates a 30% increase over the photocure, which had an ultimate cure of 0.79, implying complete methacrylate conversion after thermal processing.

During the thermal cure, the epoxy chemical conversion was given by kinetic constants $\alpha_u = 0.89$, $k = 0.010$, and $n = 2$ with an *SSE* of 25.99 (Figure 34b), and the kinetic constants from the structural conversion were $\alpha_u = 0.17$, $k = 0.010$, and $n = 2$ with an *SSE* of 0.07 (Figure 8c). As illustrated in Figure 34d, the structural conversion appears to lag the chemical conversion for the first half hour of the thermal cure. We hypothesize this is an indication that during the initial polymerization of the secondary network (epoxy-amine), the modulus is still dominated by the primary network (methacrylate), resulting in slower structural kinetics. However, since both curves tend

to overlap after approximately 70% conversion, it seems that once the secondary network

has sufficiently percolated through the primary network, the epoxy polymerization

eventually begins to correlate directly with changes in the modulus.
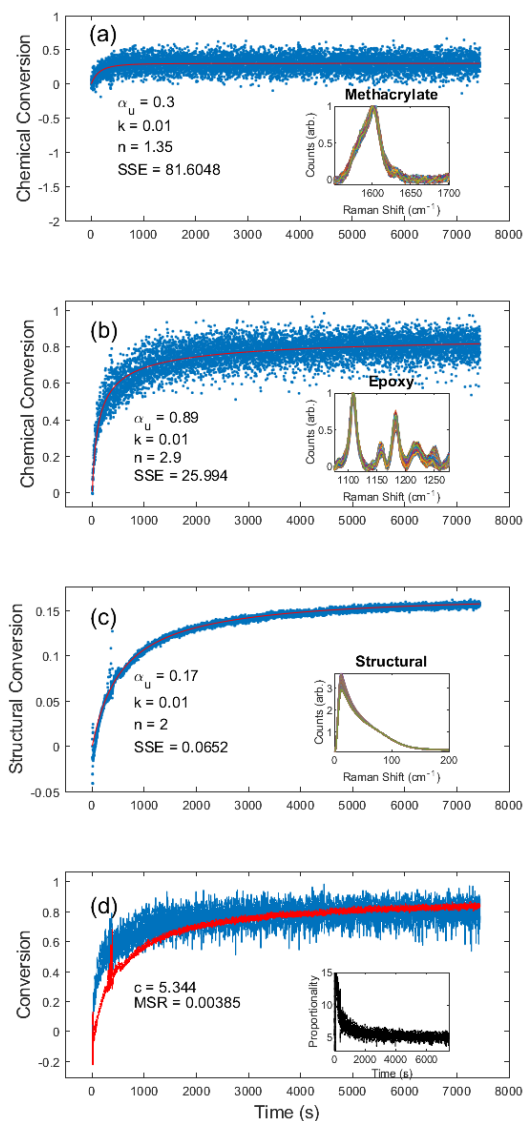
Figure 34. PBE thermal (secondary) cure kinetics obtained from (a) the methacrylate

chemical region of the Raman spectrum with inset showing the methacrylate (variable)

and phenyl (reference) peaks; (b) the epoxy chemical region of the Raman spectrum with

inset showing the epoxied (variable) and phenyl (reference) peaks; (c) the structural

region with inset showing the normalized disorder band; and (d) an overlay of the chemical conversion kinetics and the structural kinetics scaled by $c = 5.34$, with the inset showing the proportionality across the entire cure. In (a), (b), and (c) the blue dots represent measured values and the red line the fitted curve. In (d) the blue line represents the methacrylate chemical conversion, and the red line represents the proportionality corrected structural conversion.

3.5 Conclusions

These results demonstrate the applicability of utilizing the disorder band present in the low-frequency region of the Raman spectra as a measure of the polymer extent of cure. This band is a universal feature of amorphous materials, providing a noncontact and chemically agnostic methodology for determining polymerization kinetics. With the structural-to-chemical proportionality constant, we have demonstrated the ability to correlate the decrease in the overall disorder of the material and the reduction in the bond concentration of polymerization reactive functional groups. The large Raman scattering efficiency in the low-frequency provides a noticeable improvement in the signal-to-noise ratio. Although the effects of curing at elevated temperature (e.g., changes in viscosity and low-frequency Raman scattering intensity) require additional exploration, the improved signal-to-noise and chemically agnostic nature of structural cure kinetics is particularly promising for epoxy systems which have been historically difficult to measure with traditional vibrational spectroscopy [157]. Analysis of a dual-cure IPN has shown a discrepancy between the structural and chemical conversion kinetics, indicating a different relationship between polymerization and modulus as the secondary network

forms in the presence of the primary network. Further rheological studies are needed to test this hypothesis.

Chapter 4

Influence of Rheological Modifications on Primary Network Chemical and Structural Cure Kinetics for an Interpenetrating Polymer Network Resin

Texts and figures are reproduced and adapted with permission from R. V. Chimenti *et al*., "Influence of Rheological Modifications on Primary Network Chemical and Structural Cure Kinetics for an Interpenetrating Polymer Network Resin," Manuscript submitted for publication.

4.1 Abstract

We have previously shown that low-frequency Raman spectroscopy is a viable method for assessing resin structural cure kinetics and complements the traditional chemical conversion determined from the fingerprint region of the spectrum. In this work we further evaluate the relationship between the structural and chemical conversion by investigating two chemically identical yet rheologically different interpenetrating polymer network resin formulations. Rheological analysis demonstrates a correlation between structural conversion and storage modulus, which is not present in chemical conversion. We show that one can produce master cure kinetics curves with comparable kinetic constants using both the chemical and structural conversion methodologies. Parametric analysis of the structural conversion, chemical conversion, and photorheological conversion was combined with a model for the shear modulus as a function of extent of cure.

4.2 Introduction

Both structural and chemical kinetics are critical for understanding the structure–property–processing relationships in polymer science. While many experimental

techniques are available for investigating polymer kinetics, including DSC [4, 5, 10], rheology [135], and FTIR spectroscopy [7, 18, 144], none of these methodologies is particularly well suited for *in situ* studies. On the other hand, Raman spectroscopy is ideal for *in situ* analysis since it is a non-contact, laser-based measurement. However, it has historically been of limited utility in applied polymer science due to its relatively low sensitivity, especially for epoxy/amine polymers due to the low polarizability of those functional groups. In the previous chapters, we demonstrated an alternative approach using the low-frequency region of the Raman spectrum to probe the overall structural changes in polymers, which vastly improved the signal-to-noise ratio of the measurement [154, 158].

Traditionally, Raman-based kinetics studies have focused on the modes in the chemical fingerprint region, whereby changes in peak height are related to the bond concentration [136, 151-153] and changes in peak width or position correlate to steric effects associated with structural changes [88]. Raman scattering is also sensitive to acoustic phonon modes which result from long-range cooperative vibrations across the entire material. In glassy and liquid phase materials, the phonon density of states $g(v)$, v being the phonon frequency, is a broad continuous function dominated by two main features – the Boson and van Hove peaks [63, 99, 108, 109, 114, 117, 154]. The Boson peak is defined as the maximum of the normalized phonon density of states $\frac{g(v)}{v^2}$ and is extremely sensitive to the sound velocity. The van Hove peak originates from singularities at the edge of the Brillouin zone and is therefore far less affected by physical changes [63].

The intensity of the Stokes-shifted Raman scattering $I_R(v)$ is given by Equation 35 [42, 99, 116, 117, 154]. The continuous spectrum of low-energy phonons results from the random arrangement of microdomains through the amorphous macrostructure, making it a universal feature directly related to the overall disorder of the material. Since entropy is related to the phonon population distribution, normalizing this disorder band by the shoulder and integrating over the peak provides a chemically agnostic method for quantitating changes in conformational entropy.

In addition to $I_R(v)$, there is also an additional contribution in the measured Raman spectrum due to quasi-elastic Rayleigh scattering, which arises from the translational energy associated with the molecules in the sample. This results in a broadening of the Rayleigh band. These two spectral contributions, combined with the Rayleigh filter cut-on associated with the collection optics, result in a broad (~150 cm^{-1} wide) disorder band in polymers with an apparent peak near 15 cm^{-1} and a well-defined shoulder dominated by the Boson and van Hove peaks, respectively. Even though the observed disorder band contains these additional contributions, we have previously demonstrated that normalizing the spectrum to the shoulder and integrating over the apparent peak can be used to monitor the structural changes in polymers [154].

In the previous chapter, we demonstrated the ability to utilize this method to monitor the extent of cure for a variety of different chemistries, including a photo-curable methacrylate resin, a thermally curable epoxy/amine resin, and a sequential photo-thermal curable methacrylate-epoxy interpenetrating polymer network (IPN) resin system [158]. In all three resin systems, we demonstrated that the relationship between the chemical and structural cure kinetics can be described by a proportionality constant *c*

particular to each system; however, two instances deviated from this behavior. In one case, there was an apparent initial dip in the structural conversion of the thermally cured epoxy/amine resin system, likely due to a transient-temperature-induced softening of the material before polymerization. In the other, we noticed a lag between the chemical and structural conversion when curing the secondary network of the IPN resin system, indicating a different relationship between polymerization and modulus as the secondary network forms in the presence of the primary network. In both cases, the assumption is that the observed behavior reflects the sensitivity of the Boson peak to the speed of sound and therefore the material's modulus. This work presents a follow-up study with two chemically identical but rheologically distinct IPN resin systems to further investigate the relationship between the chemical, structural, and rheological conversion throughout the curing process. We purposefully limited our scope to the primary network formation of these two IPN resins, eliminating any changes in $g(\nu)$ and $I_R(\nu)$ associated with the non-isothermal nature of the secondary network formation.

4.3 Experimental Methods and Procedures

4.3.1 Resin Formulation

For this study, we chose to use a dual-cure methacrylate-epoxy IPN resin, which was prepared by combining commercially available methacrylate and epoxy/amine resin components. The epoxy/amine component was prepared from a diglycidyl ether of bisphenol A resin (EPON 828, Hexion) and a diethylmethylbenzenediamine resin (Epikure W, Hexion). The epoxy equivalent weight (EEW) for EPON 828 was 186.1 g/eq and the amine hydrogen equivalent weight (AHEW) of Epikure W was 44.6 g/eq. These components were formulated with 1:1 equivalents of epoxide to amine hydrogen. Phenyl

methacrylate (inhibited with 100 ppm of hydroquinone, Scientific Polymer Products), bisphenol A glycerolate dimethacrylate (BisGMA, Esstech), and the epoxy/amine were formulated based on 1:0.5:0.5 molar equivalents, respectively. Diphenyl(2,4,6-trimethylbenzoyl)phosphine oxide (TPO, >98 %, TCI America) was added as the photoinitiator at 2 wt% based on the total resin, see Figure 35. This resin formulation is denoted as PBE-unfilled. A second formulation was produced based on the procedure originally developed for direct ink write printability by Lehman-Chong with the addition of 4 wt% carboxyl terminated butadiene nitrile rubber (CTBN, 10 % acrylonitrile, 2.47 % carboxyl, approx. MW 19,000 g/mol, Scientific Polymer Products Inc.) and 7 wt% fumed silica (Aerosil 200, Spectrum Chemical Mfg Corp.) [159]. This resin formulation is denoted as PBE-filled. All resin formulations were mixed with an ARE-310 planetary mixer (Thinky) programmed for 10 min at 2000 rpm to mix and 5 min at 2200 rpm to defoam. This mixing cycle was repeated until all components were fully dispersed homogenously (2-3 cycles).
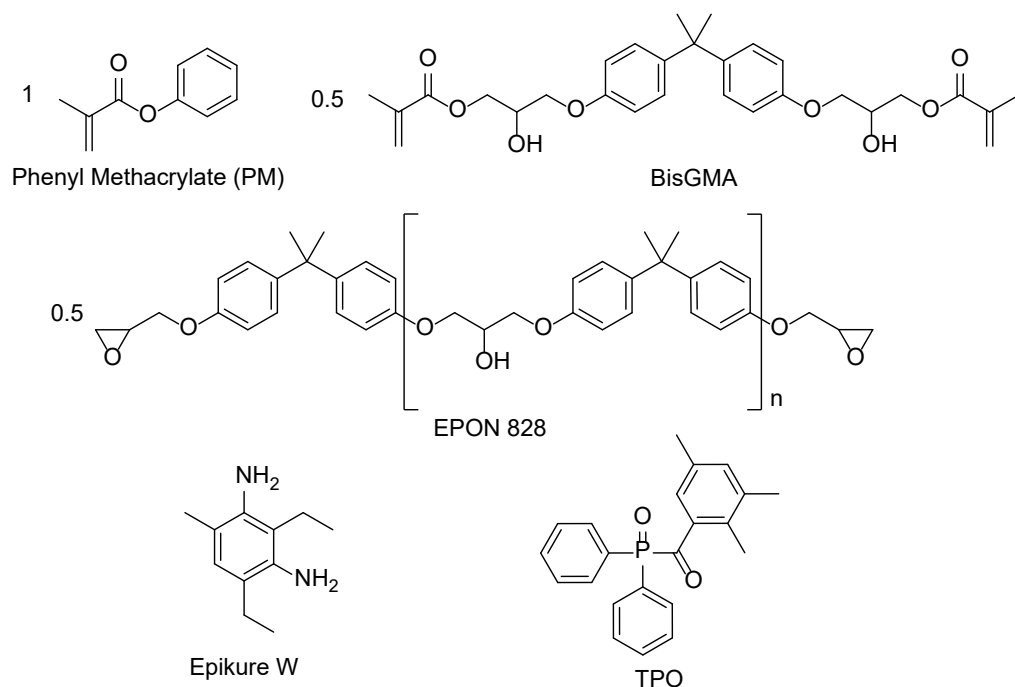
Figure 35. Components of PBE resin formulation.

4.3.2 Raman Measurements

After mixing, the resin was applied onto a $4 \times 6 \times 0.020$ in^3 steel test panel and spread with an adjustable film coater set to a thickness of 500 μm for PBE-unfilled and 300 μm for PBE-filled. The layer thicknesses were chosen to not exceed the penetration depth of the illumination source. A $25 \times 25 \times 0.15$ mm^3 glass cover slip was then placed on top of the resin to mitigate oxygen inhibition at the surface, and the excess resin was removed. Light from an Omnicure Series 2000 high-power mercury vapor source (Excelitas Technologies) was passed through a 365-nm bandpass filter, fiber-coupled to a large core "light pipe," and then collimated directly above the sample platform to allow for relatively uniform illumination of the resins. The Raman scattering measurements were done with a 785-nm CleanLine laser and TR-PROBE from Coherent Inc. with a

37.5-mm focal length aspheric lens for both excitation and collection. The scattered light was then fiber-coupled directly into an EAGLE Raman-S (Ibsen Photonics) high-throughput transmission (f/1.6) spectrograph. Raman scattered light was collected with a deep depleted back-illuminated thermoelectrically cooled (-60 ºC) CCD camera (Andor Instruments) with a 950-ms integration time. The UV illumination intensity was controlled by a combination of lamp settings and adjustments to the height between the collimating lens and the sample platform, and the light intensities were measured with a Thorlabs power meter.

4.3.3 Photorheology Measurements

Photorheology was performed with a TA Instruments Discovery Hybrid Rheometer (Discovery HR-2) and the same 365-nm filtered fiber-coupled Omnicure S2000 light source. A geometry consisting of a disposable 20-mm diameter aluminum top plate and 20-mm diameter acrylic bottom plate was used. The light intensity was calibrated with a CON-TROL-CURE® Silver Line radiometer (UV Process Supply, Inc.). Experiments were conditioned with axial force adjustment and conducted isothermally at 25 °C. Unless otherwise stated in the results and discussion, an oscillation method in fast sampling mode was used with a 0.3 % strain, 1.0 Hz frequency, and 10.0 μN·m torque, and the geometry gap was set to 100 μm. For each experiment, the sample first oscillated without UV irradiation, and then the lamp was turned on at 30 s to irradiate the sample for the remainder of the experiment.

4.4 Results and Discussion

4.4.1 Initial Rheological Verification

To verify the rheological differences between the two resin formulations we measured the initial loss and storage shear moduli, G'' and G', respectively, of ten different samples of each formulation (Figure S1). The averaged value of $\frac{G''}{G'}$ was determined to be 92.2 ± 30.6 for the PBE-unfilled samples and 0.3 ± 0.1 for PBE-filled samples. Viscosity as a function of shear rate was also measured for PBE-unfilled and PBE-filled samples with a 1° 20-mm cone and plate geometry with a 30-μm gap at 25 °C. The shear rate was increased logarithmically from 0.001 to 1000 Hz and then decreased from 1000 to 0.001 Hz. As shown in Figure 36, the PBE-unfilled resin displayed Newtonian behavior between 0.1 and 1000 Hz with an average viscosity of 1.3 ± 0.1 Pa·s, while the PBE-filled resin displayed non-Newtonian shear thinning with average viscosities of 4.4 kPa·s at 0.1 Hz and 4.8 Pa·s at 1000 Hz. The rheological behavior of both resins is consistent with expectations based on the previous reports for a similar resin formulation [159].
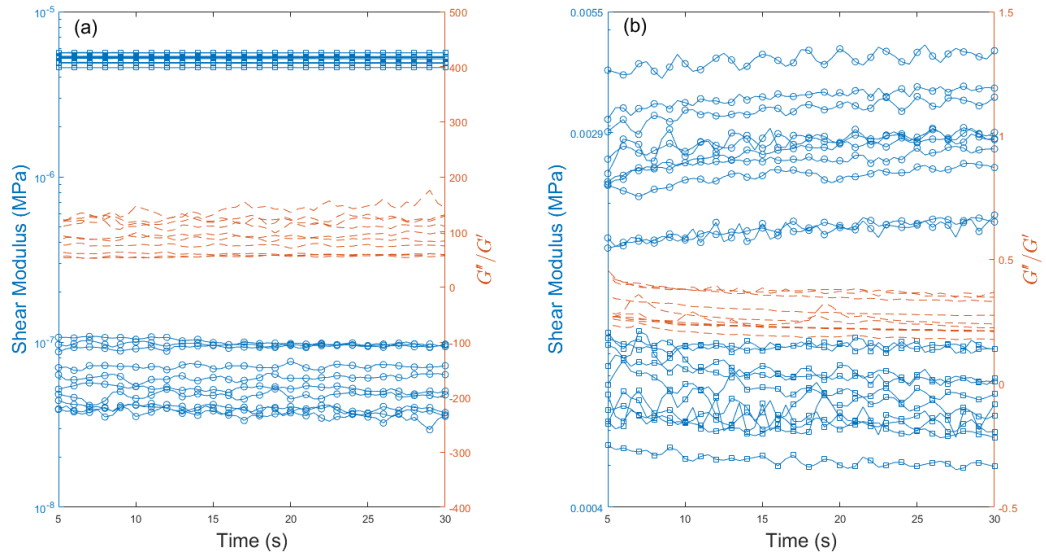
Figure 36. Storage modulus G' (blue circles), loss modulus G'' (blue squares), and $\frac{G''}{G'}$ (orange dashes) for ten different measurements of (a) PBE-unfilled and (b) PBE-filled.
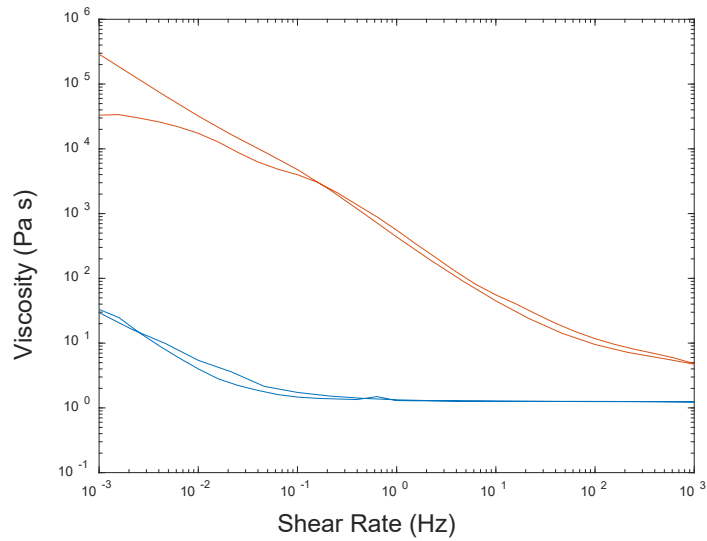
Figure 37. Viscosity as a function of shear rate for PBE-unfilled (blue) and PBE-filled (orange).

4.4.2 Raman Cure Kinetics

Raman measurements were performed in triplicate for each resin system during 1-h cures at four different illumination intensities. All Raman spectra were analyzed with custom MATLAB code which included an adaptive, iteratively reweighted, Penalized Least Squares algorithm for baseline correction for data in the chemical fingerprint region. No baseline correction was utilized in the structural region. Anomalous spikes in the spectra due to cosmic rays were removed with a custom 6-sigma algorithm.

The conversion α was calculated from Equation 39. For structural "conversion", $\alpha = \alpha_s$ and the variable and reference peaks selected were the peak (~14 cm^{-1}) and shoulder (~85 cm^{-1}) of the disorder band, respectively [158]. For chemical kinetics, $\alpha = \alpha_c$ and the variable and reference peaks were the aromatic CCH quadrant stretch (~1605 cm^{-1}) and the C=C stretch (~1637 cm^{-1}), respectively [90]. All integrated intensities were determined with bounds of ±7 cm^{-1} of the line center. Example spectra are shown in Figure 38.
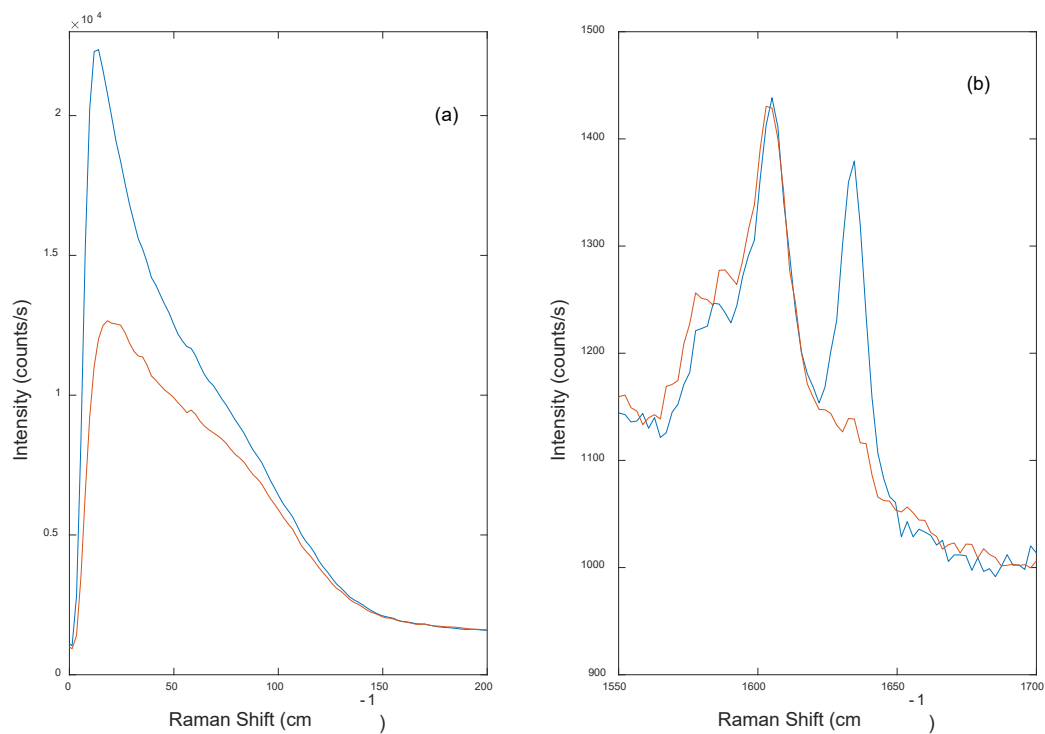
Figure 38. Representative Raman spectra of PBE-unfilled pre (blue) and post (orange) UV cure, with (a) showing the low-frequency structural region, and (b) showing the chemical fingerprint region.

The averaged conversion curves for each illumination intensity are shown in Figure 39. The chemical-to-structural proportionality constant c, defined as the mean of $\frac{\alpha_c}{\alpha_s}$ from 100 s to 3600 s, is tabulated for all eight measurements in Table 5. For the PBE-unfilled resin system, c was relatively stable regardless of illumination intensity and is consistent with the previously reported value $c = 1.98 \pm 0.02$ [158]. For the PBE-filled resin system, c ranged from 2.40 to 2.60 trending upward as the illumination intensity was decreased. The overall increase in c is likely due to the addition of the non-reactive fillers which serve to reduce the impact of the primary network formation on the overall

105

modulus of the material. Additionally, while α_s and α_c are proportional to each other during most of the cure, there is a noticeable decrease in α_s during the initial inhibition time of the PBE-filled resin (Figure 2d). This deviation, which was similarly reported I the previous chapter for thermally cured epoxy resin systems [158], is not present in α_c for the PBE-filled resin nor in α_s and α_c of the PBE-unfilled resin.
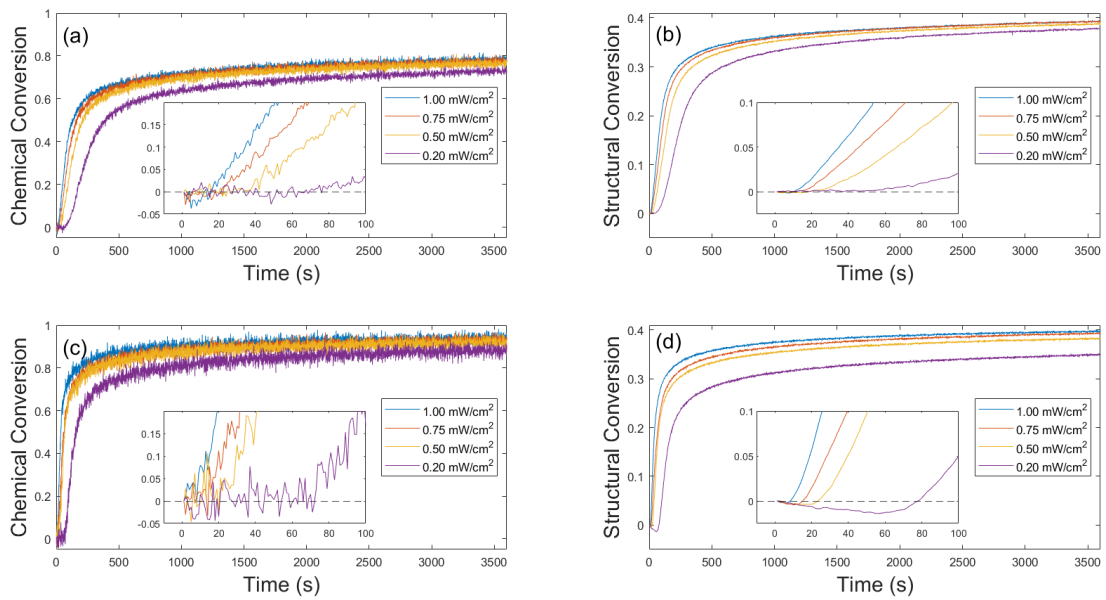
Figure 39. PBE-unfilled (a) chemical and (b) structural conversion kinetics. PBE-filled (c) chemical and (d) structural conversion kinetics. Insets show the first 100 s of the cure.

Table 5

Chemical to Structural Conversion Proportionality Constant c for PBE-Unfilled and PBE-Filled at Various Illumination Intensities

Intensity (mW/cm^2)	1.00	0.75	0.50	0.20
PBE-unfilled	1.99 ± 0.03	1.97 ± 0.03	1.98 ± 0.04	1.94 ± 0.05
PBE-filled	2.40 ± 0.06	2.40 ± 0.06	2.45 ± 0.07	2.60 ± 0.14

4.4.3 Photorheological Analysis

We performed photorheology on both resin systems at each illumination intensity for 1 h (Figures 40 and 41). Figure 41c shows that G' remains constant prior to activation for the PBE-unfilled resin, whereas Figure 41d shows a dip in G' of the PBE-filled resin prior to activation for all four measurements. These results correlate with the magnitude of the normalized disorder band observed in the low-frequency Raman spectrum and confirm our hypothesis about softening. We attribute this softening to additional absorbance of the illumination lamp by the fillers, which in return warms the sample prior to the activation of the polymerization process.
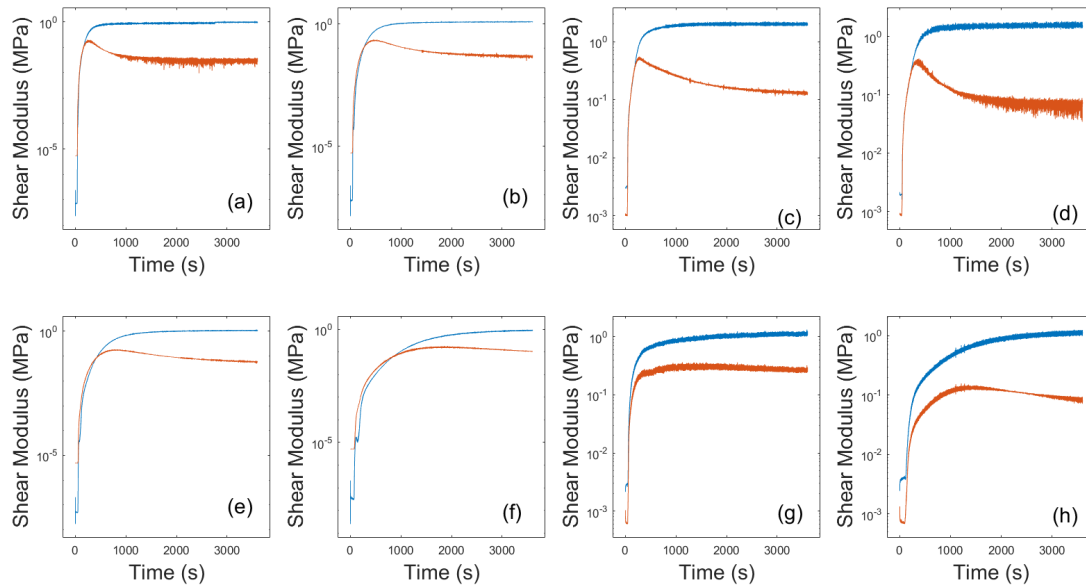
Figure 40. Storage modulus G' (blue), loss modulus G'' (orange) for PBE-unfilled at 1.00 mW/cm^2 (a), 0.75 mW/cm^2 (b), 0.50 mW/cm^2 (e), and 0.20 mW/cm^2 (d), and PBE-filled at 1.00 mW/cm^2 (e), 0.75 mW/cm^2 (f), 0.50 mW/cm^2 (g), and 0.20 mW/cm^2 (h).
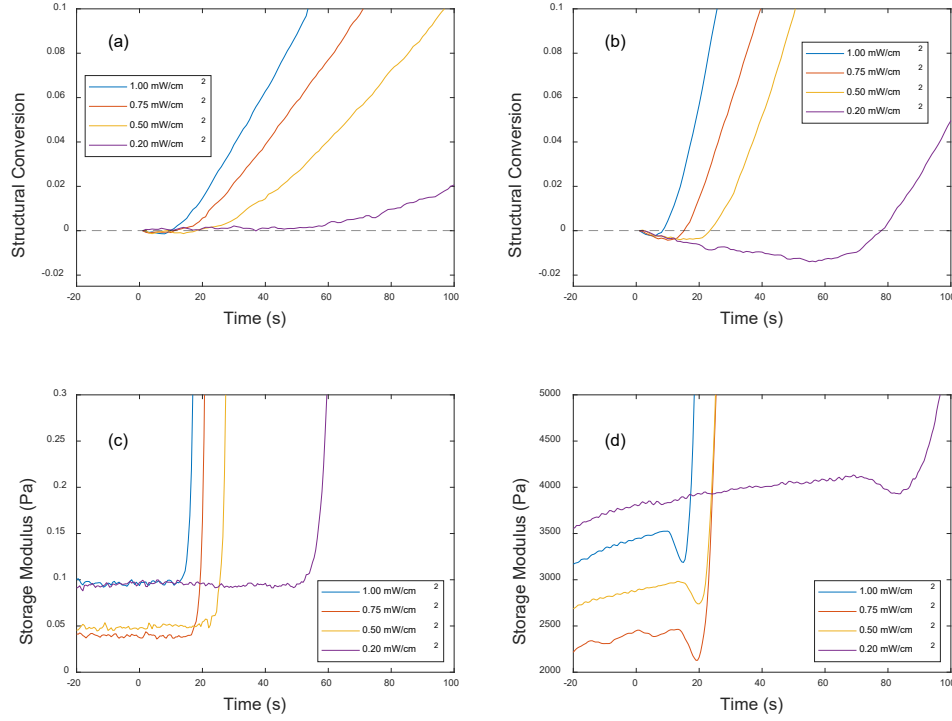
Figure 41. Structural conversion kinetics α_s for (a) PBE-unfilled and (b) PBE-filled during the first 100-s of cure. Storage modulus G' for (c) PBE-unfilled and (d) PBE-filled during the first 100 s of cure.

4.4.4 Cure Kinetics Master Curves

Next, we utilized the methodology previously developed by Tu *et al*. [131] to generate a master cure kinetics curve for each resin system. We used a phenomenological free radical polymerization reaction rate equation

$$\frac{d\alpha}{dt} = I_E^{\omega} k(\alpha_u - \alpha)^n \tag{42}$$

where I_E is the illumination intensity, k the reaction rate constant, n the reaction order, and α_u the ultimate conversion. The exponential factor ω is known as the dose rate

109

dependency, which relates to the radical termination mechanism with $\omega = 0.5$ correlating to bimolecular termination and $\omega = 1$ correlating to unimolecular termination [146].

To determine ω we used the logarithmic form of Equation 42,

$$\ln R_p = \omega \ln I + \ln \kappa \tag{43}$$

where $R_p = \frac{d\alpha}{dt}$ and $\kappa = k(\alpha_u - \alpha)^n$. The kinetic constants for each illumination intensity were determined by first removing the initial oxygen inhibition time from each conversion curve and fitting to the integrated form of Equation 3 with linear least squares regression independent of dose rate. For the chemical kinetics $\alpha = \alpha_c$ and for the structural kinetics $\alpha = c\,\alpha_s$. The data were also fit to a rational polynomial with the default nonlinear least squares method in the MATLAB curve fitting toolbox and symbolically differentiated to determine R_p. The rational fit for both resins systems used a 5th order numerator with a 5th order or 4th order denominator for PBE-unfilled and PBE-filled resins, respectively. R_p was then plotted against α and fit with a spline function to enable the determination of ω as a function of α. The mean value of ω was then used to rescale conversion as a function of effective dose $I^\omega t$. This allows for all conversion curves from each light intensity to be superimposed onto one master curve, which can then be fitted to Equation 43 to determine the kinetic constants for the master curve. The results of this procedure are shown in Figures 42 and 43 for PBE-unfilled chemical and structural kinetics, respectively, and Figures 44 and 45 for PBE-filled chemical and structural kinetics, respectively. It should be noted that in the case of PBE-filled structural kinetics, the initial dip in the structural conversion leads to an ambiguity in

defining the end of the inhibition time. We chose to use the zero crossing to avoid

negative conversion values and to maintain consistency with the other curves.
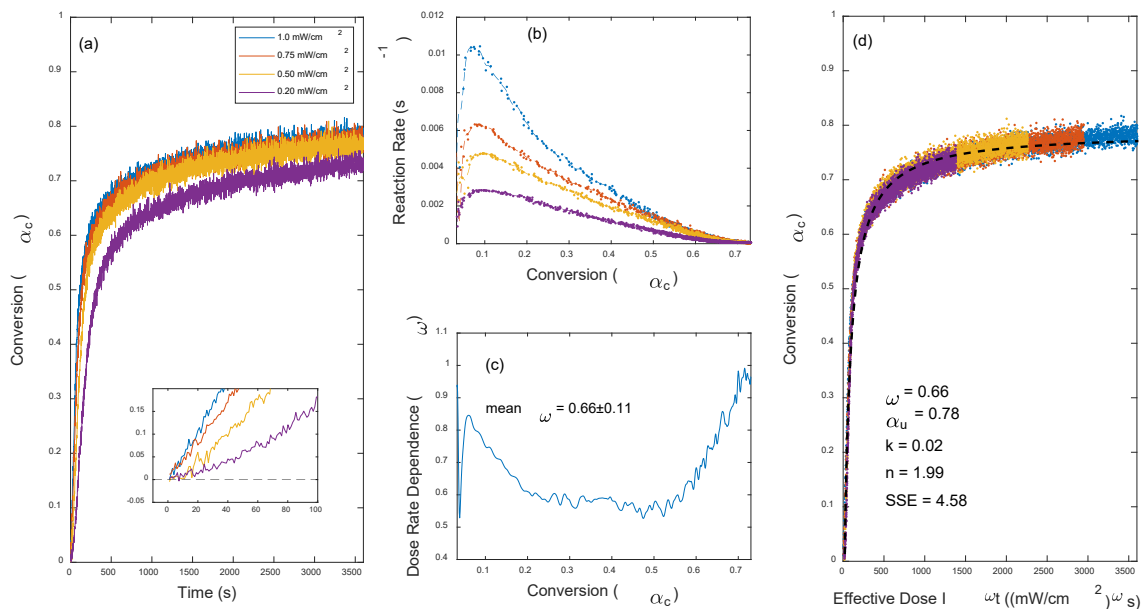
Figure 42. (a) PBE-unfilled α_c shifted to remove inhibition time with inset showing the

first 100 s of the reaction, (b) R_p as a function of α_c, (c) calculated ω as a function of α_c,

and (d) master curve with fit parameters.
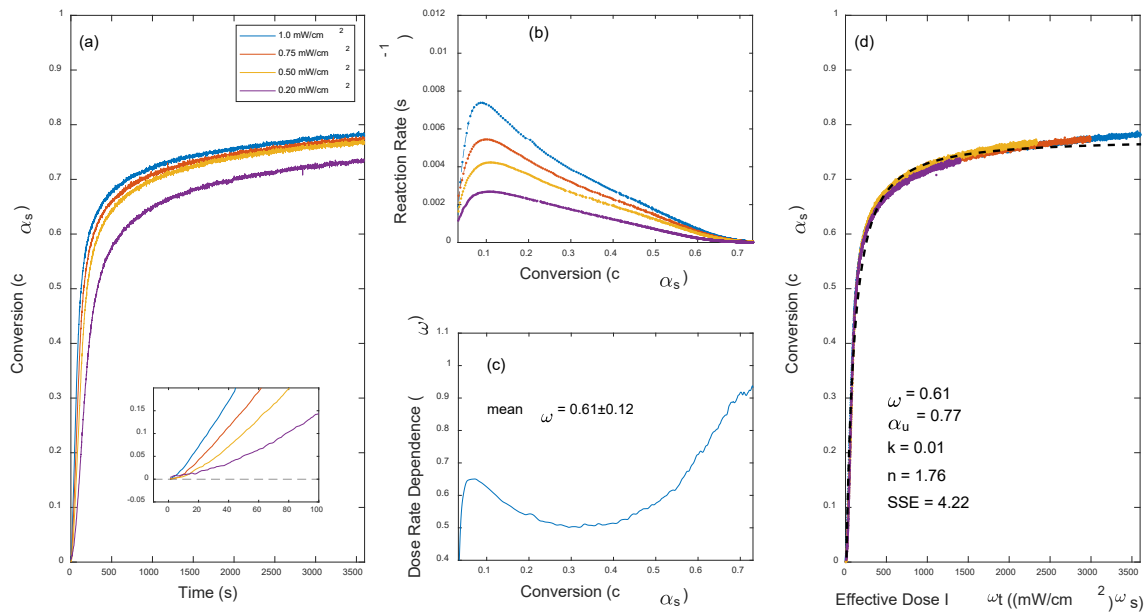
Figure 43. (a) PBE-unfilled c α_s shifted to remove inhibition time with inset showing the first 100 s of the reaction, (b) R_p as a function of α_c, (c) calculated ω as a function of α_c, and (d) master curve with fit parameters and sum square error, *SSE*.
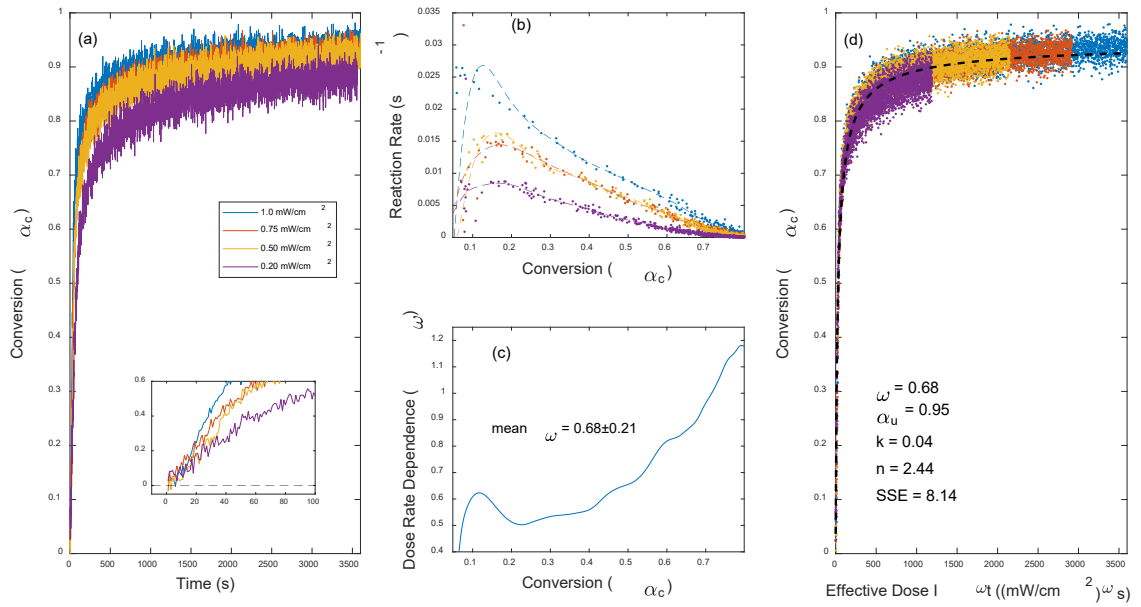
Figure 44. (a) PBE-filled α_c shifted to remove inhibition time with inset showing the first 100 s of the reaction, (b) R_p as a function of α_c, (c) calculated ω as a function of α_c, and (d) master curve with fit parameters.
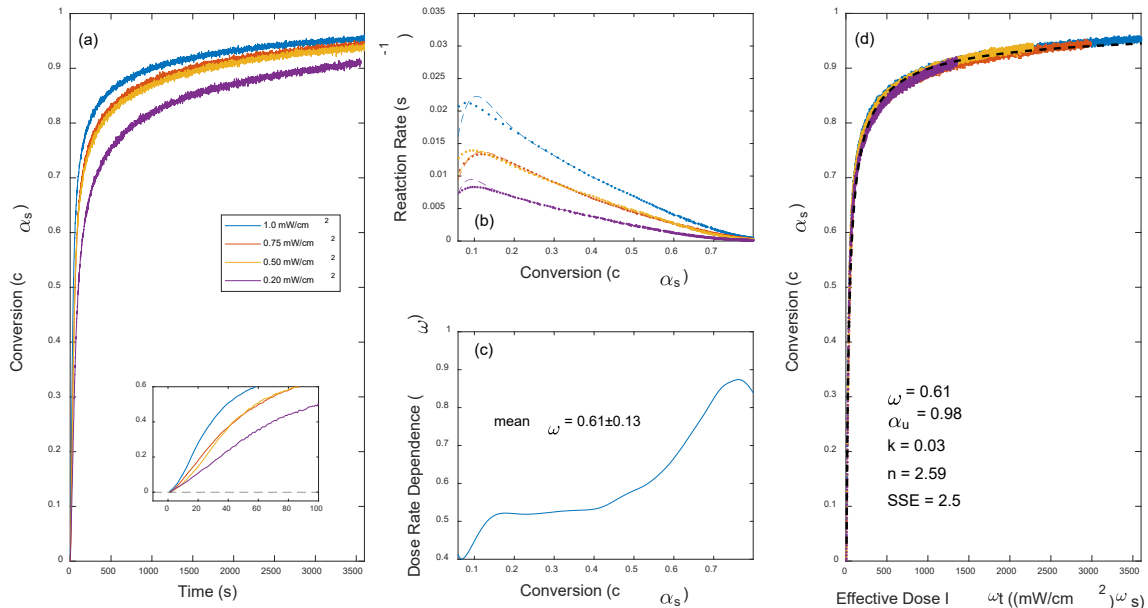
Figure 45. (a) PBE-filled c α_s shifted to remove inhibition time with inset showing the first 100 s of the reaction, (b) R_p as a function of α_c, (c) calculated ω as a function of α_c, and (d) master curve with fit parameters.

For the PBE-unfilled and PBE-filled resin systems, the chemical and structural conversion master curves resulted in self-consistent kinetic constants as shown in Table 6. For the PBE-unfilled resin system the uncertainty in ω and the *SSE* for the fit were similar for both the chemical and structural kinetics. There was a noticeable decrease in signal-to-noise for the kinetics of the PBE-filled resin, resulting from a combination of increased fluorescence background in the Raman spectra from the fumed silica and CTBN fillers and the reduced volume fraction of methacrylate and phenyl functional groups. While both the chemical and structural kinetics demonstrated an increase in

noise, it was far more pronounced in the chemical region which propagated more error into the R_p, increasing the uncertainty in ω and the *SSE* for the chemical kinetics fit.

Table 6

Master Curve Fit Parameters for PBE-Unfilled and PBE-Filled Resins

Resin	Kinetics Type	ω	α_u	k	n	SSE
PBE-unfilled	Chemical	0.66±0.11	0.78	0.02	1.99	4.58
	Structural	0.61±0.12	0.77	0.01	1.76	4.22
PBE-filled	Chemical	0.68±0.21	0.95	0.04	2.44	8.07
	Structural	0.61±0.13	0.98	0.03	2.59	2.50

In general, ω trended upward throughout the cure process (see Figures 42c, 43c, 44c, and 45c). This is consistent with a high degree of bimolecular termination in the early stages of cure due to the low viscosity and high chain mobility, switching to unimolecular termination as the material vitrifies into a glassy state, reducing the likelihood of unterminated chains finding each other. The PBE-filled resin system exhibits a roughly 2.5× increase in R_p when compared to that of the PBE-unfilled resin system (see Figures 42b, 43b, 44b, and 45b) which is reflected in the accompanying

115

increase in both k and n. It should be noted that there is no apparent shift in the gel point

(maximum of R_p). This is consistent with the percolation threshold definition of gel point

which is purely dependent on monomer functionality [22]. The increased reaction rate of

the PBE-filled resin system also correlates with a stark increase in α_u by 17% according

to the chemical kinetics and 21% according to the structural kinetics, suggesting that the

fumed silica and CTBN fillers are plasticizing the resin and delaying vitrification of the

glassy network which allows for higher monomer diffusion.

4.4.4 Parametric Analysis of Modulus vs. Conversion

Lastly, we analyzed the modulus as a function of α to better understand the

parametric relationship between α_c, α_s, and G'. The impact of extent of cure on

viscoelastic properties has been of great interest in recent years, and models have been

developed for modulus as a function of α based on both observations and first principles

[20, 26, 145, 160-164]. Aldridge *et al*. used simultaneous stimulated Brillouin scattering

and chemical fingerprint Raman spectroscopy to develop a comprehensive rate equation

for longitudinal storage modulus M' as a function of both α and $\frac{d\alpha}{dt}$ [160]. O'Brien *et al.*

took a first principles approach by using a Prony series expansion of the Kohlrausch-

Williams-Watts function to develop a model for both G and Young's modulus E as a

function of extent of cure, experimentally verifying their results for an epoxy resin

system using a combination of DSC, rheology, and dynamic mechanical analysis [20].

More recently, Wang *et al*. have built on the work of O'Brien *et al*. by demonstrating that

E can be modeled as a simple exponential function of α for a photopolymerizable

acrylate resin system [162].

Patil *et al.* recently published a methodology for using molecular dynamics to predict mechanical properties of a resin as a function of α [164]. In their work they took the relatively simplistic approach of observing that the storage modulus varied sigmoidally as a function of α. O'Brien *et al.* utilized a similar approach when they empirically defined the first term in their Prony series model for the equilibrium shear modulus using a similar sigmoidal function [20]. For this study, we used the empirical approach of modeling G' as a sigmoidal function, where the step change occurs as the resin vitrifies into the glassy state. However, we did observe that a pure sigmoid was insufficient to properly fit the measured data, particularly at higher illumination intensities. We determined that the addition of a rate dependency term, $G'_\varrho = \Upsilon \alpha^\varrho$, was needed where Υ is the rate constant and ϱ is the rate order. For our current dataset we saw minimal improvements in the *SSE* values for fits with $\varrho > 1$, therefore deciding on the following model

$$G'(\alpha) = a\mathcal{L}\left(\frac{\alpha - \alpha_g}{b}\right) + \Upsilon\alpha + G'_0 \tag{44}$$

where G'_0 is the initial storage modulus, α_g is the extent of cure at which glass transition occurs, b relates to the sharpness of the transition with α, a relates to the ultimate storage modulus, and $\mathcal{L}(x)$ the logistic sigmoid function defined as $\mathcal{L}(x) = (1 + e^{-x})^{-1}$.

Photorheology and cure kinetics data were corrected to remove oxygen inhibition and then fitted to Equation 47 with the default nonlinear least squares method in the MATLAB curve fitting toolbox. Figure 46 shows G' versus α_c for the PBE-unfilled resin at all four illumination intensities. In each case, Equation 44 provided fits with self-consistent and physically realistic values for α_g ranging from 0.62 to 0.68 and a ranging

from 0.92 to 1.18 MPa. Interestingly, α_g appears to be negatively correlated to I indicating that a faster cure rate results in a transition to the glassy state at a lower degree of polymerization, but this may be related to the kinetics of the polymerization versus timescale of the measurement. Figure 47 shows G' versus α_s for the PBE-unfilled at all four illumination intensities, which also fits well to Equation 44 and provides values of α_g between 0.31 and 0.36 similarly decreasing in value as I increases, and values of a between 0.91 and 1.18 MPa. The ratios of the values of α_g for the chemical kinetics to those of the structural kinetics results in 1.94 ± 0.04, consistent with the values of c in both previously published results [158] and Table 5. The values for b and Υ appear to remain relatively consistent regardless of illumination intensity across both chemical and structural kinetics.
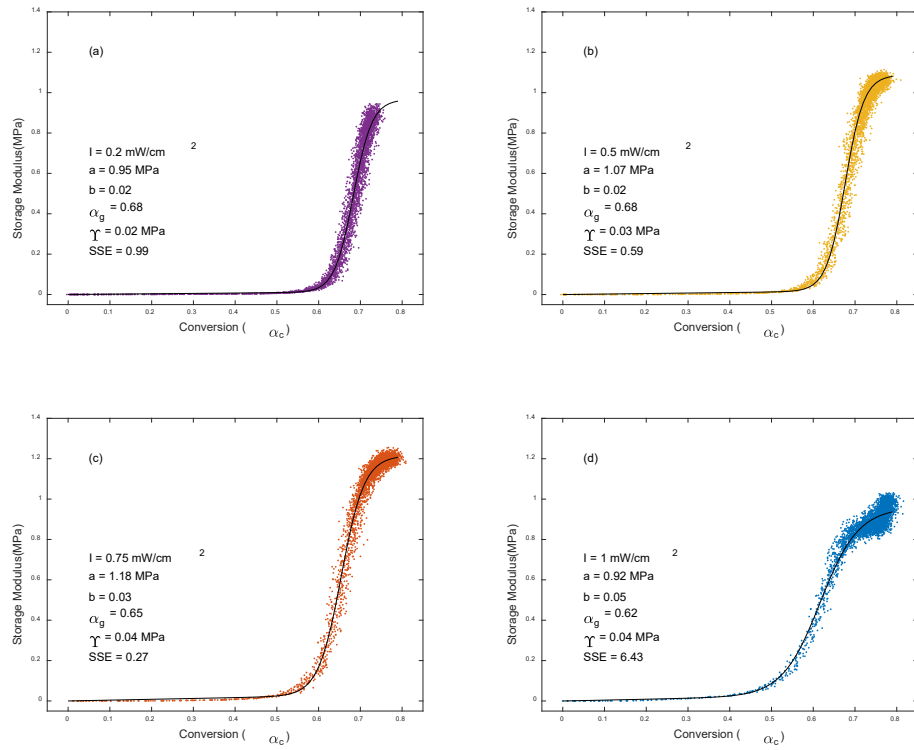
Figure 46. Shear modulus G' vs chemical conversion α_c for PBE-unfilled at (a) 0.2 mW/cm^2, (b) 0.5 mW/cm^2, (c) 0.75 mW/cm^2, and (d) 1 mW/cm^2 illumination intensities.
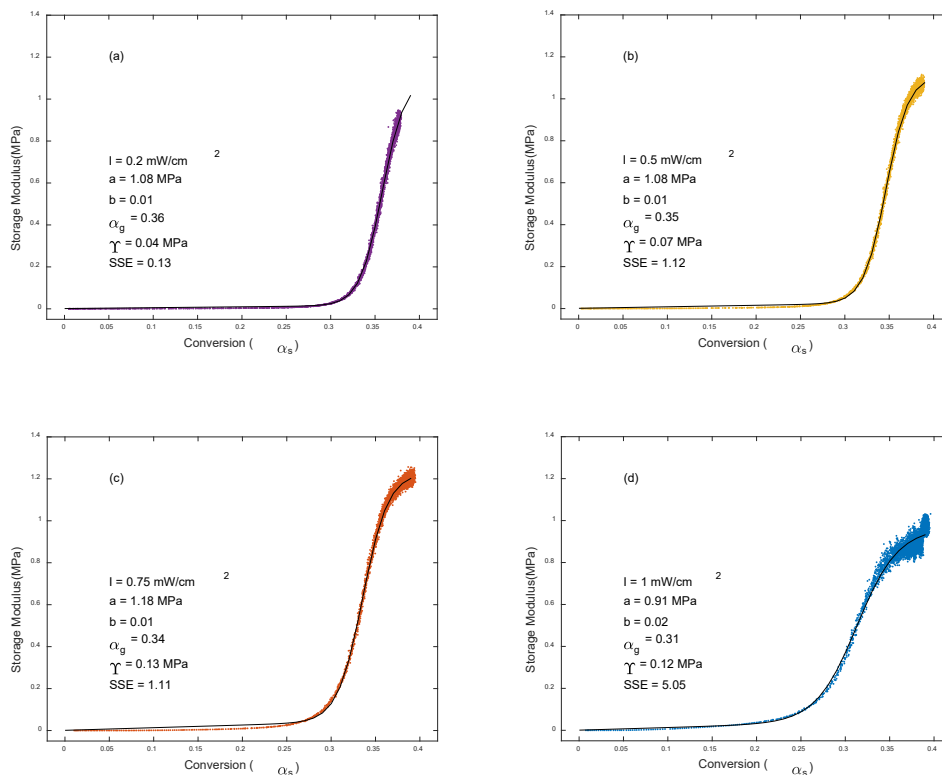
Figure 47. Shear modulus G' vs chemical structural α_s for PBE-unfilled at (a) 0.2 mW/cm^2, (b) 0.5 mW/cm^2, (c) 0.75 mW/cm^2, and (d) 1 mW/cm^2 illumination intensities.

Figures 48 and 49 show the results for the PBE-filled for G' versus α_c and α_s, respectively. Again, in each case, Equation 47 provided fits with self-consistent and physically realistic values. However, as seen in Figure 48, the PBE-filled chemical kinetics showed a far more stable α_g ranging from 0.81 to 0.83 and wider ranging values of a from 0.95 to 1.82 MPa. Figure 49 shows G' versus α_s for the PBE-filled at all four illumination intensities, which also fits well to Equation 47. These results provide values of α_g between 0.33 and 0.36 that similarly decrease in value as I increases, and values of a between 1.23 and 1.89 MPa. The ratios of the values of α_g for the chemical kinetics to

those of the structural kinetics results in 2.41 ± 0.08, consistent with the c values in Table 1. The values for b are fairly consistent with those of the unfilled resin systems, but the values of Y show a stark increase when compared to those of the PBE-unfilled resin. This is likely due to the non-Newtonian nature of the filled resin system, which could affect the evolution of the Poisson ratio throughout the cure, and therefore increase the deviation from the simple sigmoidal approximation. Interestingly, α_g for the PBE-filled resin chemical conversion was significantly greater than α_g for the PBE-unfilled, consistent with resin plasticization by the fillers. However, there does not appear to be a significant change in α_g for the structural conversion. This appears to be because the final G' values are relatively consistent (within 1 MPa of each other) for both PBE-filled and PBE-unfilled as shown in Table 7. This further supports the theory that α_s is a measure of the change in modulus, similar to how α_c is a measure of the change in bond concentration.
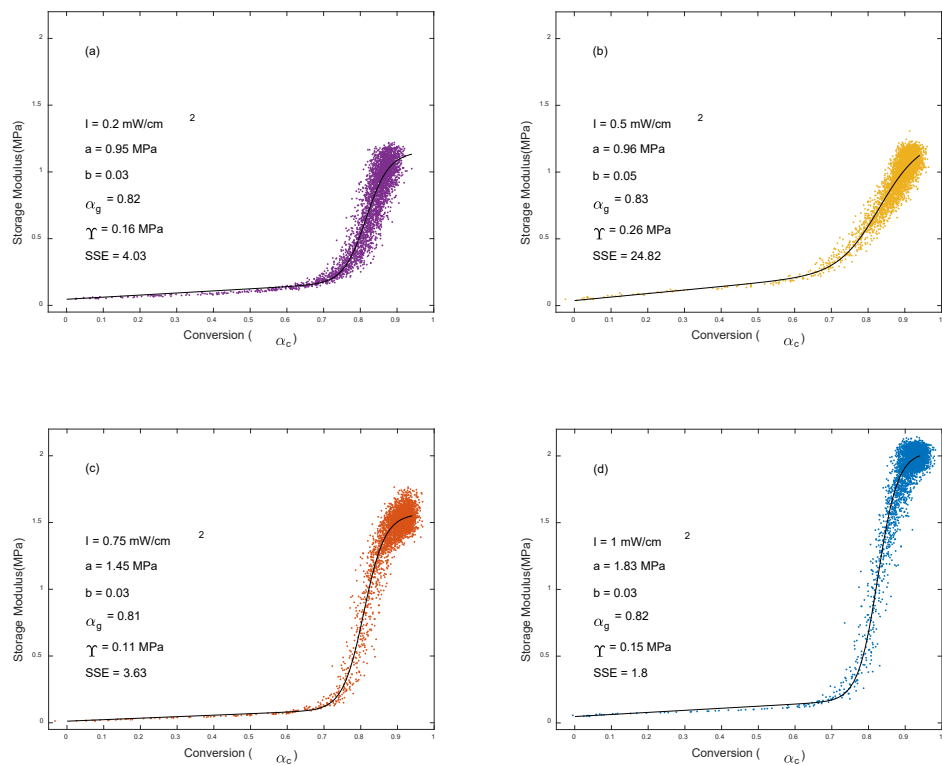
Figure 48. Shear modulus G' vs chemical conversion α_c for PBE-filled at (a) 0.2 mW/cm^2, (b) 0.5 mW/cm^2, (c) 0.75 mW/cm^2, and (d) 1 mW/cm^2 illumination intensities.
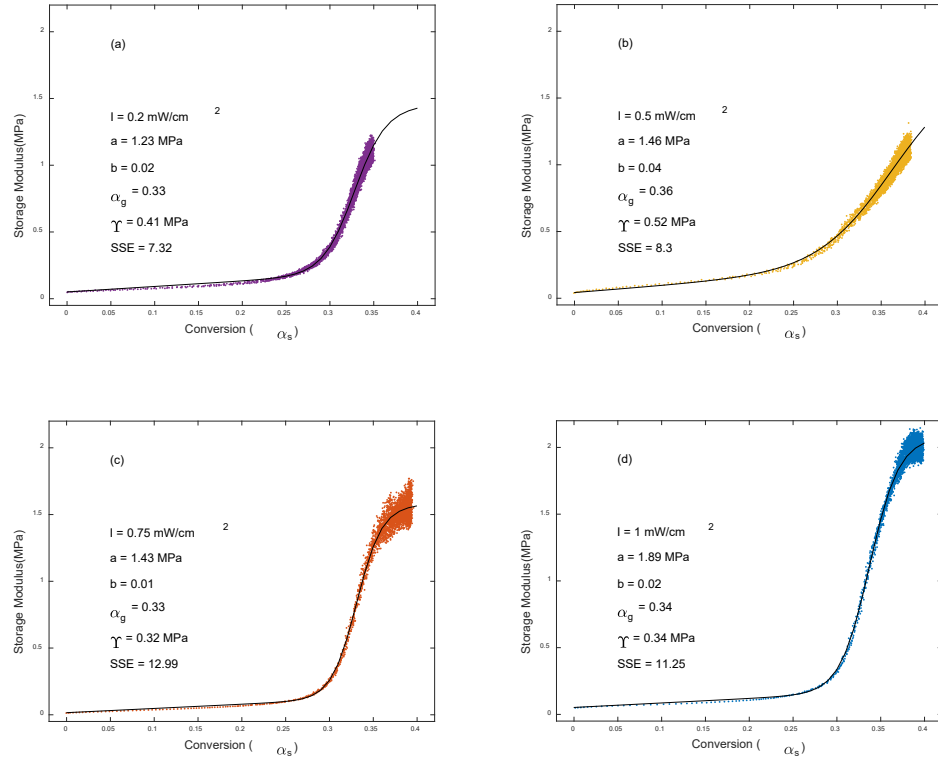
Figure 49. Shear modulus G' vs chemical structural α_s for PBE-filled at (a) 0.2 mW/cm^2, (b) 0.5 mW/cm^2, (c) 0.75 mW/cm^2, and (d) 1 mW/cm^2 illumination intensities.

Table 7

Final Shear Modulus G' for PBE-Unfilled and PBE-Filled at Various Illumination Intensities

Intensity (mW/cm^2)	1.00	0.75	0.50	0.20
PBE-unfilled | G' (MPa)	0.98 ± 0.04	1.21 ± 0.02	1.07 ± 0.03	0.90 ± 0.03
PBE-filled | G' (MPa)	2.00 ± 0.07	1.57 ± 0.11	1.12 ± 0.07	1.12 ± 0.07

4.5 Conclusions

By comparing two rheologically distinct but chemically similar resin formulations, we have been able to demonstrate a direct correlation between the structural conversion kinetics as determined by the normalized disorder band in the low-frequency Raman spectrum and the change in modulus throughout the cure process. Not only does this serve to elucidate the cause of previously observed discrepancies between the structural and chemical conversion profiles, but through the development of a relatively simplistic model for modulus as a function of α we have shown that both α_s and α_c are related to G'. Additionally, we have demonstrated that despite the rheological differences between the two resin systems we were able to create conversion master curves as a function of effective dose providing self-consistent kinetic constants across both chemical ($\alpha = \alpha_c$) and structural ($\alpha = c\,\alpha_s$) conversion measurements. Although, it is important to note that if there is a transient dip in viscosity prior to activation, the resultant dip in α_s can lead to a slight ambiguity in the determined oxygen inhibition time. However, other than a slight variance in α_u, this does not appear to affect the resultant master curve. The chemically agnostic nature and high signal-to-noise ratio already makes α_s extremely desirable as a method of determining cure kinetics behavior of resins. The additional insight of the direct relationship between α_s and the rheological properties not only illustrates the underlying physical phenomena behind the technique but has the potential to expand its usefulness for better understanding the structure-property-processing relationships of a resin throughout its cure.

Chapter 5

Conclusions and Recommendations for Future Work

5.1 Conclusions

The aim of this work was to explore the possibilities for using a dual-VBG-based low-frequency Raman probe for *in situ* monitoring of structural kinetics in polymetric materials. As discussed in Chapter 1, the low-frequency Raman spectra of amorphous materials is directly related to the phonon density of states $g(v)$. In disordered solids and liquids $g(v)$ is dominated by two main features – the Boson peak which depends on the speed of sound and the van Hove peak which is related to the size of the first Brillioun zone [63]. Therefore, we hypothesized that by normalizing the low-frequency Raman spectra of a polymer (which we named the disorder band) to its shoulder (van Hove peak) we could directly observe changes in confirmational entropy.

In Chapter 2 we demonstrated the efficacy of this approach by measuring the glass transition temperature T_g of three different polymers – polystyrene, PMMA, and PLA. In that chapter, we also developed a first-principles-based peak-fitting model which allowed us to differentiate the quasi-elastic Rayleigh scattering QERS from the Raman scatter. Using this model, we were able to isolate $\frac{g(v)}{v^2}$ for polystyrene and verify that the Boson peak position below T_g was in agreement with previously reported values [99] and that the Boson peak blue shifted and increased in intensity above T_g.

In Chapter 3 we demonstrated the ability to use the same technique to monitor polymerization extent of cure for a photocurable methacrylate resin, a thermally curable epoxy-amine resin, and a dual photo-thermal curable methacrylate/epoxy IPN resin. Using the normalized disorder band, we were able to produce "structural" conversion α_s

kinetic curves which were fitted to a phenomenological kinetics rate equation. We also

used bands in the chemical fingerprint region of the spectra to generate chemical

conversion α_c kinetic curves and demonstrate that the two curves were linearly correlated

by a proportionality constant c. We did however notice two discrepancies where the

relationship between the chemical and structural conversion deviated. The first appears to

be related to a transient softening of the epoxy-amine system prior to polymerization. The

second was during the curing of the secondary network of the methacrylate/epoxy IPN,

which we attributed to a delay between the onset of secondary network polymerization

and increase in overall modulus of the material.

In Chapter 4 we further investigated the relationship between α_s and shear

modulus G by examining two chemically identical yet rheologically distinct resin

formulations. We demonstrated that the rheologically modified resin systems which

contained fumed silica and CTBN fillers experienced a transient dip in storage modulus

G' prior to polymerization, which was also detected in α_s but not in α_c. However, we

demonstrated that regardless of this initial softening of the material we could still

generate master cure kinetics curves with comparable kinetic constants using both the

chemical and structural conversion methodologies. Additionally, we developed a semi-

empirical model for $G'(\alpha)$ through parametric analysis of α_s, α_c, and G' during

photopolymerization which has the potential to facilitate non-contact modulus

characterization.

The work of this dissertation clearly demonstrates the ability to use low-frequency

Raman spectroscopy to monitor structural kinetics of polymers. As we will discuss in the

next section, this methodology has the potential to expand the field of polymer science

and engineering through judicious use of confocal low-frequency Raman spectroscopy. Furthermore, since Raman spectroscopy is a laser-based technique, the methodologies demonstrated here have the potential to be integrated directly into polymer processing facilities as well as 3D printers to provide real time structural information.

5.2 Recommendations for Future Work

5.2.1 2D and 3D Mapping of Heterogeneous Materials

The ability to utilize Raman spectroscopy to measure T_g not only allows for non-contact *in situ* analysis of materials as described in this dissertation, it also opens the door towards high-resolution mapping of T_g in heterogeneous materials. Traditional methods for determining T_g, such as DMA and DSC, are bulk analysis techniques providing an average value for the whole material. In recent years, atomic force microscopy (AFM) has emerged as an excellent tool for producing nanoscale maps of viscoelastic properties. [165-169] However, there does not appear to be any literature regarding micron resolution mapping of T_g. While we exclusively focused on the use of a fiber optic Raman probe in this work, the same dual-VBG-based optical design can easily be incorporated into a Raman microscope as well. The lateral resolution of a microscope can be approximated by the Rayleigh criterion, $R \approx \frac{0.61\lambda}{NA}$, where NA is the numerical aperture of the objective lens [170]. Therefore, one can easily produce hyperspectral Raman maps of a material with a resolution below 1 μm. Furthermore, with a confocal pinhole, the depth of focus can similarly be reduced to ~1 μm allowing for 3D hyperspectral Raman imaging of optically transparent materials.

By combining the methodology developed in Chapter 2 with a confocal Raman microscope equipped with dual-VBG-based filtration, we should be able to produce 2D and 3D T_g maps to help explore the nano-to-meso-to-macroscale evolution of T_g in heterogeneous materials. We may also be able to test the twinkling fractal theory of glass transition which hypothesizes that at T_g various microdomains throughout the material rapidly fluctuate between the glassy and rubbery phases [171-173]. This high spatial resolution approach for measuring T_g could also be particularly interesting for the analysis of micro- and nanofibers as well as polymer films, which are extremely difficult, if not impossible, to measure with traditional thermal characterization tools.

5.2.2 Correlation of Structural Conversion and Viscoelasticity

As discussed in Chapter 1 and demonstrated in Chapters 3 and 4, there is a direct link between the Boson peak and G (transverse sound velocity). The semi-empirical model presented in Chapter 4 represents the first steps towards quantitatively exploring the relationship between α_s and G. However, there is still considerable work to be done before *ab initio* viscoelastic analysis can be performed directly from low-frequency Raman spectra. There are several potential pathways that we envision for gaining a better understanding of the correlation between α_s and viscoelasticity. The first is a traditional chemometrics approach whereby large numbers of Raman spectra with associated rheological values are fed into a cluster analysis or regression algorithm to develop a "black box" model for predicting viscoelasticity from a given spectral measurement. The second approach would be to further explore the fundamental physics underpinning α_s, α_c, and G to develop a first principles model with greater predictive power than the semi-

empirical model developed in this work. One particularly interesting avenue for better understanding the linear relationship between α_s and α_c is through the use of two-dimensional correlation spectroscopy (2D-CORS). While 2D-CORS is most commonly used in nuclear magnetic resonance (NMR) spectroscopy, it has also been generalized by Noda *et al.* for use in vibrational spectroscopy [174]. This methodology would allow for both synchronous and asynchronous analysis of relationship of the peak and shoulder of the disorder band to the various chemical bands of interest. A third approach would be to explore the use of supervised, physics-informed machine learning; a methodology which effectively hybridizes the first two approaches. As discussed by Fujinuma *et al.* this approach allows for connecting machine learning directly with experiment rapidly improving the pace of discovery and reducing the overall data requirements for predictive models [175].

5.2.3 Investigation of Anomalous anti-Stokes Behavior During Epoxy Cure

As discussed in Chapter 1, at thermal equilibrium the intensity of the Stokes scattered light should always be greater than that of the anti-Stokes scattered light. However, during our investigation of epoxy polymerization kinetics (see Chapter 3), we observed anomalous anti-Stokes Raman (AASR) behavior. Figure 50 shows a representative example of AASR while curing EPON 828 for 3 hours at 180 °C. To date, AASR has been observed as a result of coherent anti-Stokes Raman scattering (CARS) [176] as well as from phononic resonance [177], but to our knowledge there is no discussion in the literature regarding AASR during polymerization. We do not believe the observed AASR is due to CARS because of our collection geometry. Additionally,

CARS-induced AASR has been shown to be extremely sensitive to laser intensity, and based on our initial observations, the AASR does not appear to be correlated with laser power. Phononic resonance due to an imbalance between bond breaking (phonon annihilation) and bond formation (phonon creation) may be responsible for vibrational energy level population inversion, which could explain the increased likelihood of anti-Stokes scattering during polymerization. This initial hypothesis is supported by the fact that as seen in Figure 50b, the AASR is largest during the start of the cure, decreases rapidly after gelation, and eventually disappears after the material has vitrified into the glassy state.
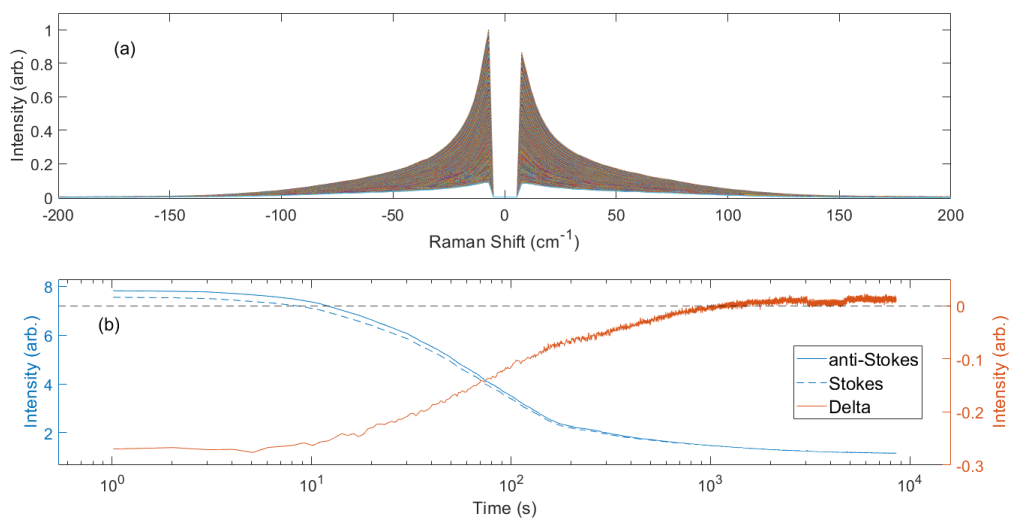
Figure 50. (a) Normalized low-frequency Raman spectra of EPON 828 cured at 180 °C for 3-hours. (b) Integrated intensity of the anti-Stokes (solid blue) and Stokes (dashed blue) Raman scattering as a function of time during the cure, along with the difference between the two intensities (orange).

Alternatively, the observed AASR could also be explained from a purely entropic perspective whereby the entropy S of the sample is decreasing as the internal energy U is increasing. Assuming Boltzmann entropy where the number of states is defined on a phase-space hypersurface [178] and the entropy-energy-temperature relationship, $\frac{\partial S}{\partial U} = \frac{1}{T}$, a rapid decrease in S and increase U would result in a negative absolute temperature (NAT). Combining the NAT hypothesis with Equation 25 would result in $\frac{I_S}{I_{AS}} < 1$ which is consistent with our preliminary observations. It is important to note that the phononic resonance and NAT hypotheses are not mutually exclusive and in fact may both represent two different ways of explaining the same phenomena.

To test these hypotheses, we propose to first systematically evaluate the effects of varying both laser power and collection geometry to rule out CARS. We also propose to evaluate the effects of varying the cure temperature and therefore the reaction rate, as we would expect the AASR to be proportional to cure rate. Lastly, we would like to perform isothermal differential scanning calorimetry (iso-DSC) to determine the heat released during the cure. Since the heat flux in an insulator is directly related to the net phonon flux, we anticipate a direct correlation between the iso-DSC heat flow and the magnitude of the AASR.

References

[1] J. Pellegrino, T. Makila, S. McQueen, and E. Taylor, "Measurement science roadmap for polymer-based additive manufacturing," 2016.

[2] M. Lang, S. Hirner, F. Wiesbrock, and P. Fuchs, "A Review on Modeling Cure Kinetics and Mechanisms of Photopolymerization," *Polymers,* vol. 14, no. 10, p. 2074, 2022, doi: 10.3390/polym14102074.

[3] O. Konuray, J. M. Salla, J. M. Morancho, X. Fernández-Francos, M. García-Alvarez, and X. Ramis, "Curing kinetics of acrylate-based and 3D printable IPNs," *Thermochimica Acta,* vol. 692, p. 178754, 2020, doi: 10.1016/j.tca.2020.178754.

[4] J. W. Kopatz, J. Unangst, A. W. Cook, and L. N. Appelhans, "Compositional effects on cure kinetics, mechanical properties and printability of dual-cure epoxy/acrylate resins for DIW additive manufacturing," *Additive Manufacturing,* vol. 46, p. 102159, 2021/10/01/ 2021, doi: https://doi.org/10.1016/j.addma.2021.102159.

[5] F. Jiang and D. Drummer, "Curing Kinetic Analysis of Acrylate Photopolymer for Additive Manufacturing by Photo-DSC," *Polymers,* vol. 12, no. 5, p. 1080, 2020, doi: 10.3390/polym12051080.

[6] "A review of DSC kinetics methods," in *TA Instruments* vol. 73, ed, 2010.

[7] F. Wu, X. Zhou, and X. Yu, "Reaction mechanism, cure behavior and properties of a multifunctional epoxy resin, TGDDM, with latent curing agent dicyandiamide," *RSC advances,* vol. 8, no. 15, pp. 8248-8258, 2018.

[8] K. Mphahlele, S. S. Ray, and A. Kolesnikov, "Cure kinetics, morphology development, and rheology of a high-performance carbon-fiber-reinforced epoxy composite," *Composites Part B: Engineering,* vol. 176, p. 107300, 2019/11/01/ 2019, doi: https://doi.org/10.1016/j.compositesb.2019.107300.

[9] A. E698-18, "Standard test method for kinetic parameters for thermally unstable materials using differential scanning calorimetry and the Flynn/Wall/Ozawa method," ed: ASTM International West Conshohocken, PA, 2018.

[10] G. Mashouf Roudsari, A. K. Mohanty, and M. Misra, "Study of the Curing Kinetics of Epoxy Resins with Biobased Hardener and Epoxidized Soybean Oil," *ACS Sustainable Chemistry & Engineering,* vol. 2, no. 9, pp. 2111-2116, 2014, doi: 10.1021/sc500176z.

[11] M. Wagner, *Thermal Analysis in Practice: Collected Applications*. Schwerzenbach, Switzerland: Mettler-Toledo, 2017, p. 349.

[12] R. Zallen, *The Physics of Amorphous Solids*. John Wiley & Sons, Inc., 1983.

[13] P. C. Hiemenz and T. Lodge, *Polymer chemistry*, 2nd ed. Boca Raton: CRC Press, 2007, pp. xvii, 587 p.

[14] J. C. Mauro, *Materials Kinetics*. Elsevier, 2021.

[15] C. A. Angell, "Structural instability and relaxation in liquid and glassy phases near the fragile liquid limit," *Journal of Non-Crystalline Solids,* vol. 102, no. 1, pp. 205-221, 1988/06/01/ 1988, doi: https://doi.org/10.1016/0022-3093(88)90133-0.

[16]   C. Dalle-Ferrier *et al.*, "Why many polymers are so fragile: A new perspective," *The Journal of Chemical Physics,* vol. 145, no. 15, p. 154901, 2016, doi: 10.1063/1.4964362.

[17]   J. Mauro, *Materials kinetics*. Waltham: Elsevier, 2021, p. 525.

[18]   J. Tu, K. Makarian, N. J. Alvarez, and G. R. Palmese, "Formulation of a Model Resin System for Benchmarking Processing-Property Relationships in High-Performance Photo 3D Printing Applications," *Materials,* vol. 13, no. 18, p. 4109, 2020, doi: 10.3390/ma13184109.

[19]   R. V. Chimenti *et al.*, "Method for determining resin cure kinetics with low-frequency Raman spectroscopy," *The Analyst,* vol. 148, no. 22, pp. 5698-5706, 2023, doi: 10.1039/d3an01099f.

[20]   D. J. O'Brien, P. T. Mather, and S. R. White, "Viscoelastic Properties of an Epoxy Resin during Cure," *Journal of Composite Materials,* vol. 35, no. 10, pp. 883-904, 2001, doi: 10.1177/a037323.

[21]   J. A. Calzonetti and C. J. Laursen, "PATENTS OF CHARLES GOODYEAR: HIS INTERNATIONAL CONTRIBUTIONS TO THE RUBBER INDUSTRY," *Rubber Chemistry and Technology,* vol. 83, no. 3, pp. 303-321, 2010, doi: 10.5254/1.3525687.

[22]   M. Rubinstein and R. H. Colby, *Polymer Physics*. Oxford University Press 2003.

[23]   R. J. Young and P. A. Lovell, *Introduction to polymers*. CRC press, 2011.

[24]   H. H. Winter and F. Chambon, "Analysis of linear viscoelasticity of a crosslinking polymer at the gel point," *Journal of rheology,* vol. 30, no. 2, pp. 367-382, 1986.

[25]   B.-S. Chiou, S. R. Raghavan, and S. A. Khan, "Effect of Colloidal Fillers on the Cross-Linking of a UV-Curable Polymer: Gel Point Rheology and the Winter−Chambon Criterion," *Macromolecules,* vol. 34, no. 13, pp. 4526-4533, 2001, doi: 10.1021/ma010281a.

[26]   M. Péron, V. Sobotka, N. Boyard, and S. Le Corre, "Bulk modulus evolution of thermoset resins during crosslinking: Is a direct and accurate measurement possible?," *Journal of Composite Materials,* vol. 51, no. 4, pp. 463-477, 2017, doi: 10.1177/0021998316647119.

[27]   M. Ivankovic, L. Incarnato, J. M. Kenny, and L. Nicolais, "Curing Kinetics and Chemorheology of Epoxy/Anhydride System," *Journal of Applied Polymer Science,* vol. 90, pp. 3012–3019, 2003, doi: 10.1002/app.12976.

[28]   C. V. Raman, "A new radiation," *Indian Journal of physics,* vol. 2, pp. 387-398, 1928.

[29]   C. Raman and K. Krishnan, "A new class of spectra due to secondary radiation. Part I," 1928.

[30]   NobelPrize.org. " Award ceremony speech." https://www.nobelprize.org/prizes/physics/1930/ceremony-speech/ (accessed Fri. 5 Jan 2024.

[31]   T. H. Maiman, "Stimulated optical radiation in ruby," 1960.

[32]   R. V. Chimenti, "Excitation source parameters dictate Raman spectroscopy outcomes," *Laser Focus World* vol. 53, no. 1, pp. 76-79, 2017.

[33]   E. Siegler Jr and C. Hinman, "A LASER-RAMAN SPECTROMETER," 1964.

[34] I. R. Lewis and H. Edwards, *Handbook of Raman spectroscopy: from the research laboratory to the process line*. CRC press, 2001.

[35] W. H. Weber and R. Merlin, *Raman scattering in materials science*. Springer Science & Business Media, 2000.

[36] D. J. Griffiths and D. F. Schroeter, *Introduction to quantum mechanics*. Cambridge university press, 2018.

[37] C. Pasquini, "Near infrared spectroscopy: fundamentals, practical aspects and analytical applications," *Journal of the Brazilian chemical society,* vol. 14, pp. 198-219, 2003.

[38] M. Somoza. "Morse-potential.png." Wikipedia. https://en.wikipedia.org/wiki/Morse_potential#/media/File:Morse-potential.png (accessed January 6, 2024).

[39] D. J. Griffiths, "Introduction to electrodynamics," ed: American Association of Physics Teachers, 2005.

[40] C. Coll and C. Melius, "Theoretical calculation of Raman scattering cross sections for use in flame analysis," Sandia National Lab.(SNL-CA), Livermore, CA (United States), 1976.

[41] R. V. Chimenti, J. Daley, J. Sack, J. Necsutu, and N. Whiting, "Reconversion of Parahydrogen Gas in Surfactant-Coated Glass NMR Tubes," *Molecules,* vol. 28, no. 5, p. 2329, 2023, doi: 10.3390/molecules28052329.

[42] R. Shuker and R. W. Gammon, "Raman-Scattering Selection-Rule Breaking and the Density of States in Amorphous Materials," *Physical Review Letters,* vol. 25, no. 4, pp. 222-225, 1970, doi: 10.1103/physrevlett.25.222.

[43] R. C. Powell, *Symmetry, group theory, and the physical properties of crystals*. Springer, 2010.

[44] D. A. McQuarrie and J. D. Simon, *Physical chemistry: a molecular approach*. University science books Sausalito, CA, 1997.

[45] A. Inc., "RAMAN VS INFRARED SPECTROSCOPY MEASUREMENT OF OCTASULFUR."

[46] M. Becucci, R. Bini, E. Castellucci, B. Eckert, and H. Jodl, "Mode assignment of sulfur α-S8 by polarized Raman and FTIR studies at low temperatures," *The Journal of Physical Chemistry B,* vol. 101, no. 12, pp. 2132-2137, 1997.

[47] C. Kittel, *Introduction to solid state physics*. John Wiley & sons, inc, 2005.

[48] G. Chen, *Nanoscale energy transport and conversion: a parallel treatment of electrons, molecules, phonons, and photons*. Oxford university press, 2005.

[49] C. Adessi, S. Pecorario, S. Thébaud, and G. Bouzerar, "First principle investigation of the influence of sulfur vacancies on thermoelectric properties of single layered MoS_2," *Physical Chemistry Chemical Physics,* vol. 22, no. 26, pp. 15048-15057, 2020, doi: 10.1039/d0cp01193b.

[50] R. Chimenti, T. Thompson, and D. Yang, "Raman Analysis of Si Crystallinity," *Application Notebook,* 2011.

[51] J. Schossig *et al.*, "CO2 to Value-Added Chemicals: Synthesis and Performance of Mono- and Bimetallic Nickel–Cobalt Nanofiber Catalysts," *Catalysts,* vol. 13, no. 6, p. 1017, 2023, doi: 10.3390/catal13061017.

[52]   Y. M. Beltukov, C. Fusco, D. A. Parshin, and A. Tanguy, "Boson peak and Ioffe-Regel criterion in amorphous siliconlike materials: The effect of bond directionality," *Physical Review E,* vol. 93, no. 2, 2016, doi: 10.1103/physreve.93.023006.

[53]   V. Malinovsky, V. Novikov, P. Parshin, A. Sokolov, and M. Zemlyanov, "Universal form of the low-energy (2 to 10 meV) vibrational spectrum of glasses," *Europhysics Letters,* vol. 11, no. 1, p. 43, 1990.

[54]   V. K. Malinovsky and A. P. Sokolov, "The nature of boson peak in Raman scattering in glasses," *Solid state communications,* vol. 57, no. 9, pp. 757-761, 1986.

[55]   A. Sokolov, A. Kisliuk, M. Soltwisch, and D. Quitmann, "Medium-range order in glasses: Comparison of Raman and diffraction measurements," *Physical Review Letters,* vol. 69, no. 10, p. 1540, 1992.

[56]   A. Brodin, L. Börjesson, D. Engberg, L. Torell, and A. Sokolov, "Relaxational and vibrational dynamics in the glass-transition range of a strong glass former B 2 O 3," *Physical Review B,* vol. 53, no. 17, p. 11511, 1996.

[57]   G. Caliskan *et al.*, "Protein and solvent dynamics: how strongly are they coupled?," *The Journal of chemical physics,* vol. 121, no. 4, pp. 1978-1983, 2004.

[58]   S. Perticaroli, J. D. Nickels, G. Ehlers, and A. P. Sokolov, "Rigidity, secondary structure, and the universality of the boson peak in proteins," *Biophysical journal,* vol. 106, no. 12, pp. 2667-2674, 2014.

[59]   J. H. Roh *et al.*, "Influence of Hydration on the Dynamics of Lysozyme," *Biophysical Journal,* vol. 91, no. 7, pp. 2573-2588, 2006, doi: 10.1529/biophysj.106.082214.

[60]   R. Zorn, "The boson peak demystified?," *Physics,* vol. 4, 2011, doi: 10.1103/Physics.4.44.

[61]   E. Duval, A. Boukenter, and B. Champagnon, "Vibration eigenmodes and size of microcrystallites in glass: Observation by very-low-frequency Raman scattering," *Physical Review Letters,* vol. 56, no. 19, p. 2052, 1986.

[62]   W. Schirmacher, T. Scopigno, and G. Ruocco, "Theory of vibrational anomalies in glasses," *Journal of Non-Crystalline Solids,* vol. 407, pp. 133-140, 2015.

[63]   M. Baggioli and A. Zaccone, "Unified theory of vibrational spectra in hard amorphous materials," *Physical Review Research,* vol. 2, no. 1, 2020, doi: 10.1103/PhysRevResearch.2.013267.

[64]   A. I. Chumakov *et al.*, "Role of Disorder in the Thermodynamics and Atomic Dynamics of Glasses," *Physical Review Letters,* vol. 112, no. 2, 2014, doi: 10.1103/physrevlett.112.025502.

[65]   W. A. Kamitakahara, C. M. Soukoulis, H. R. Shanks, U. Buchenau, and G. S. Grest, "Vibrational spectrum of amorphous silicon: Experiment and computer simulation," *Physical Review B,* vol. 36, no. 12, pp. 6539-6542, 10/15/ 1987, doi: 10.1103/PhysRevB.36.6539.

[66]   A. P. Sokolov, U. Buchenau, W. Steffen, B. Frick, and A. Wischnewski, "Comparison of Raman- and neutron-scattering data for glass-forming systems," *Phys Rev B Condens Matter,* vol. 52, no. 14, pp. R9815-R9818, Oct 1 1995, doi: 10.1103/physrevb.52.r9815.

[67] T. A. Lima *et al.*, "An inelastic neutron scattering, Raman, far-infrared, and molecular dynamics study of the intermolecular dynamics of two ionic liquids," *Phys Chem Chem Phys,* vol. 22, no. 16, pp. 9074-9085, Apr 29 2020, doi: 10.1039/d0cp00374c.

[68] R. A. Crocombe, "Portable Spectroscopy," *Applied Spectroscopy,* vol. 72, no. 12, pp. 1701-1751, 2018, doi: 10.1177/0003702818809719.

[69] I. Latka, S. Dochow, C. Krafft, B. Dietzek, and J. Popp, "Fiber optic probes for linear and nonlinear Raman applications – Current trends and future development," *Laser & Photonics Reviews,* vol. 7, no. 5, pp. 698-731, 2013, doi: https://doi.org/10.1002/lpor.201200049.

[70] G. Turrell and J. Corset, *Raman microscopy: developments and applications*. Academic Press, 1996.

[71] T. Hard, "Laser wavelength selection and output coupling by a grating," *Applied Optics,* vol. 9, no. 8, pp. 1825-1830, 1970.

[72] M. G. Littman and H. J. Metcalf, "Spectrally narrow pulsed dye laser without beam expander," *Applied optics,* vol. 17, no. 14, pp. 2224-2227, 1978.

[73] M. Fukuda, *Optical semiconductor devices*. John Wiley & Sons, 1998.

[74] O. M. Efimov, L. B. Glebov, L. N. Glebova, K. C. Richardson, and V. I. Smirnov, "High-efficiency Bragg gratings in photothermorefractive glass," *Applied Optics,* vol. 38, no. 4, pp. 619-627, 1999/02/01 1999, doi: 10.1364/AO.38.000619.

[75] C. Moser and G. J. Steckman, "Output coupler for external cavity laser," ed: Google Patents, 2009.

[76] S. X. Wang and X. J. Zhou, "Spectroscopic apparatus using spectrum narrowed and stabilized laser with Bragg grating," ed: Google Patents, 2007.

[77] B. L. Volodin and V. S. Ban, "Use of volume Bragg gratings for the conditioning of laser emission characteristics," ed: Google Patents, 2007.

[78] J. M. Geary, *Introduction to lens design: with practical ZEMAX examples*. Willmann-Bell Richmond, 2002.

[79] M. M. Carrabba and R. D. Rauh, "Apparatus for measuring Raman spectra over optical fibers," ed: Google Patents, 1992.

[80] S. L. Rudder, J. B. Gannon, R. V. Chimenti, B. L. Carlin, and J. C. Connolly, "Dual wavelength Raman probe with spectral concatenation of data," ed: Google Patents, 2019.

[81] S. M. Angel and S. K. Sharma, "Fiber optic apparatus for detecting molecular species by surface enhanced Raman spectroscopy," ed: Google Patents, 1988.

[82] R. D. McLachlan, G. L. Jewett, and J. C. Evans, "Fiber-optic probe for sensitive Raman analysis," ed: Google Patents, 1986.

[83] J. Carriere, L. Ho, F. Havermeyer, E. Maye, and R. Heyler, "Identification and analysis of materials and molecular structures," ed: Google Patents, 2017.

[84] R. A. Heyler, J. T. A. Carriere, and F. Havermeyer, "THz-Raman: accessing molecular structure with Raman spectroscopy for enhanced chemical identification, analysis, and monitoring," presented at the Next-Generation Spectroscopic Technologies VI, 2013.

[85] A. L. Glebov, O. Mokhun, A. Rapaport, S. Vergnole, V. Smirnov, and L. B. Glebov, "Volume Bragg gratings as ultra-narrow and multiband optical filters," in *Micro-Optics 2012*, 2012, vol. 8428: SPIE, pp. 42-52.

[86] I. Noda, A. E. Dowrey, and C. Marcott, "Glass transition of atactic polystyrene probed at the submolecular level by dynamic infrared linear dichroism (DIRLD) spectroscopy," *Vibrational Spectroscopy,* vol. 51, no. 1, pp. 22-27, 2009, doi: 10.1016/j.vibspec.2008.09.009.

[87] N. Brun, P. Bourson, S. Margueron, and M. Duc, "Study of the thermal behavior of syndiotactic and atactic polystyrene by Raman spectroscopy," presented at the XXXVII JEEP – 37th Conference on Phase Equilibria, 2011.

[88] D. Bertoldo Menezes, A. Reyer, A. Benisek, E. Dachs, C. Pruner, and M. Musso, "Raman spectroscopic insights into the glass transition of poly(methyl methacrylate)," *Phys Chem Chem Phys,* vol. 23, no. 2, pp. 1649-1665, Jan 21 2021, doi: 10.1039/d0cp05627h.

[89] T. A. Lima, L. F. O. Faria, V. H. Paschoal, and M. C. C. Ribeiro, "Communication: Glass transition and melting lines of an ionic liquid," *J Chem Phys,* vol. 148, no. 17, p. 171101, May 7 2018, doi: 10.1063/1.5030083.

[90] D. B. Menezes, A. Reyer, A. Marletta, and M. Musso, "Glass transition of polystyrene (PS) studied by Raman spectroscopic investigation of its phenyl functional groups," *Materials Research Express,* vol. 4, no. 1, p. 015303, 2017/01/16 2017, doi: 10.1088/2053-1591/4/1/015303.

[91] E. D. A. Wypych, G. Boiteux , J. Ulanski, L. David, G. Seytre ,A. Mermet, I. Stevenson, M. Kozanecki, L. Okrasa, "Physical aging of atactic polystyrene as seen by dielectric relaxational and low-frequency vibrational Raman spectroscopies," *Journal of Non-Crystalline Solids,* vol. 351, pp. 2593–2598, 2005.

[92] V. N. Novikov, A. P. Sokolov, B. Strube, N. V. Surovtsev, E. Duval, and a. A. Mermet, "Connection between quasielastic Raman scattering and free volume in polymeric glasses and supercooled liquids," *J. Chem. Phys.,* vol. 107, no. 4, pp. 1057-1065, 22 July 1997 1997.

[93] S. C. K. L. Ngai, D. Prevosto, and Li-Min Wang, "Coupling of Caged Molecule Dynamics to JG β-Relaxation II: Polymers," *J. Phys. Chem. B,* vol. 119, no. 38, pp. 12502-12518, 2015 2015, doi: https://doi.org/10.1021/acs.jpcb.5b07293.

[94] M. Inoue, H. Hisada, T. Koide, J. Carriere, R. Heyler, and T. Fukami, "In Situ Monitoring of Crystalline Transformation of Carbamazepine Using Probe-Type Low-Frequency Raman Spectroscopy," *Organic Process Research & Development,* vol. 21, no. 2, pp. 262-265, 2017, doi: 10.1021/acs.oprd.6b00329.

[95] T. Koide *et al.*, "Identification of Pseudopolymorphism of Magnesium Stearate by Using Low-Frequency Raman Spectroscopy," *Organic Process Research & Development,* vol. 20, no. 11, pp. 1906-1910, 2016, doi: 10.1021/acs.oprd.6b00199.

[96] V. A. Ryzhov, "Low-energy vibrational excitations in polymethylmetacrylate with IR and RAMAN spectroscopy," *Physics & Astronomy International Journal,* vol. 3, no. 3, pp. 123-127, 2019, doi: 10.15406/paij.2019.03.00169.

[97] M. Baggioli and A. Zaccone, "Low-energy optical phonons induce glassy-like vibrational and thermal anomalies in ordered crystals," *Journal of Physics: Materials,* vol. 3, no. 1, 2019, doi: 10.1088/2515-7639/ab4758.

[98] M. v. d. Voort, "DYNAMICS OF VIBRATIONS IN AMORPHOUS SILICON," PhD, Utrecht University, 1999.

[99] N. V. Surovtsev and A. P. Sokolov, "Frequency behavior of Raman coupling coefficient in glasses," *Physical Review B,* vol. 66, no. 5, 2002, doi: 10.1103/physrevb.66.054205.

[100] B. H. Stuart, "Polymer crystallinity studied using Raman spectroscopy," *Vibrational Spectroscopy* vol. 10, no. 2, 1996.

[101] A. Y. Sosorev, D. R. Maslennikov, O. G. Kharlanov, I. Y. Chernyshov, V. V. Bruevich, and D. Y. Paraschuk, "Impact of Low-Frequency Vibrations on Charge Transport in High-Mobility Organic Semiconductors," *physica status solidi (RRL) – Rapid Research Letters,* 2018, doi: 10.1002/pssr.201800485.

[102] J. D. Savage, Y. K. Wang, H. D. Stidham, M. Corbett, and S. L. Hsu, "Analysis of Raman-Active Low-Frequency Bands Observed for Syndiotactic Polystyrene," *ACS Applied Polymer Materials,* no. 25, 1992.

[103] I. Noda, A. Roy, J. Carriere, B. J. Sobieski, D. B. Chase, and J. F. Rabolt, "Two-Dimensional Raman Correlation Spectroscopy Study of Poly[(R)-3-hydroxybutyrate- co-(R)-3-hydroxyhexanoate] Copolymers," *Appl Spectrosc,* vol. 71, no. 7, pp. 1427-1431, Jul 2017, doi: 10.1177/0003702817707219.

[104] P. J. Larkin, M. Dabros, B. Sarsfield, E. Chan, J. T. Carriere, and B. C. Smith, "Polymorph characterization of active pharmaceutical ingredients (APIs) using low-frequency Raman spectroscopy," *Appl Spectrosc,* vol. 68, no. 7, pp. 758-76, 2014, doi: 10.1366/13-07329.

[105] B. S. Kalanoor, M. Ronen, Z. Oren, D. Gerber, and Y. R. Tischler, "New Method to Study the Vibrational Modes of Biomolecules in the Terahertz Range Based on a Single-Stage Raman Spectrometer," *ACS Omega,* vol. 2, no. 3, pp. 1232-1240, Mar 31 2017, doi: 10.1021/acsomega.6b00547.

[106] D. Marlina, H. Hoshina, Y. Ozaki, and H. Sato, "Crystallization and crystalline dynamics of poly(3-hydroxybutyrate) / poly(4-vinylphenol) polymer blends studied by low-frequency vibrational spectroscopy," *Polymer,* vol. 181, p. 121790, 2019/10/24/ 2019, doi: https://doi.org/10.1016/j.polymer.2019.121790.

[107] P. J. Larkin, J. Wasylyk, and M. Raglione, "Application of low-and mid-frequency Raman spectroscopy to characterize the amorphous-crystalline transformation of indomethacin," *Applied Spectroscopy,* vol. 69, no. 11, pp. 1217-1228, 2015.

[108] S. A. Kirillov and O. F. Nielsen, "Boson peak in the low-frequency Raman spectra of an ordinary liquid," *Journal of Molecular Structure,* vol. 526, no. 1, pp. 317-321, 2000/08/10/ 2000, doi: https://doi.org/10.1016/S0022-2860(00)00525-1.

[109] S. A. Kirillov and T. M. Kolomiyets, "Disorder in Binary Polymer Systems near Their Critical Region Studied by Low-Frequency Raman Spectroscopy," *The Journal of Physical Chemistry B,* vol. 105, no. 16, pp. 3168-3173, 2001, doi: 10.1021/jp0016941.

[110] K. Gato, M. Y. Fujii, H. Hisada, J. Carriere, T. Koide, and T. Fukami, "Molecular state evaluation of active pharmaceutical ingredients in adhesive patches for transdermal drug delivery," *Journal of Drug Delivery Science and Technology,* vol. 58, p. 101800, 2020/08/01/ 2020, doi: https://doi.org/10.1016/j.jddst.2020.101800.

[111] J. El Haddad, B. Bousquet, L. Canioni, and P. Mounaix, "Review in terahertz spectral analysis," *TrAC Trends in Analytical Chemistry,* vol. 44, pp. 98-105, 2013, doi: 10.1016/j.trac.2012.11.009.

[112] P. Chen, C. Holbrook, P. Boolchand, D. G. Georgiev, K. A. Jackson, and M. Micoulaut, "Intermediate phase, network demixing, boson and floppy modes, and compositional trends in glass transition temperatures of binary<mml:math xmlns:mml="http://www.w3.org/1998/Math/MathML" display="inline"><mml:mrow><mml:msub><mml:mrow><mml:mtext>As</mml:mte," *Physical Review B,* vol. 78, no. 22, 2008, doi: 10.1103/physrevb.78.224208.

[113] L. Casella, M. Baggioli, T. Mori, and A. Zaccone, "Physics of phonon-polaritons in amorphous materials," *The Journal of Chemical Physics,* vol. 154, no. 1, p. 014501, 2021, doi: 10.1063/5.0033371.

[114] M. Grimsditch, A. Polian, and R. Vogelgesang, "The phonon density of states in amorphous materials," *Journal of Physics: Condensed Matter,* vol. 15, no. 31, p. S2335, 2003/07/23 2003, doi: 10.1088/0953-8984/15/31/309.

[115] B. Hehlen, E. Courtens, R. Vacher, A. Yamanaka, M. Kataoka, and K. Inoue, "Hyper-Raman Scattering Observation of the Boson Peak in Vitreous Silica," *Physical Review Letters,* vol. 84, no. 23, pp. 5355-5358, 2000, doi: 10.1103/physrevlett.84.5355.

[116] M. F. Ando *et al.*, "Boson peak, heterogeneity and intermediate-range order in binary SiO2-Al2O3 glasses," *Scientific Reports,* vol. 8, no. 1, 2018, doi: 10.1038/s41598-018-23574-1.

[117] A. P. Sokolov, U. Buchenau, W. Steffen, B. Frick, and A. Wischnewski, "Comparison of Raman- and neutron-scattering data for glass-forming systems," *Physical Review B,* vol. 52, no. 14, pp. R9815-R9818, 1995, doi: 10.1103/physrevb.52.r9815.

[118] N. Tomoshige, H. Mizuno, T. Mori, K. Kim, and N. Matubayasi, "Boson peak, elasticity, and glass transition temperature in polymer glasses: Effects of the rigidity of chain bending," *Sci Rep,* vol. 9, no. 1, p. 19514, Dec 20 2019, doi: 10.1038/s41598-019-55564-2.

[119] N. Tomoshige, S. Goto, H. Mizuno, T. Mori, K. Kim, and N. Matubayasi, "Understanding the scaling of boson peak through insensitivity of elastic heterogeneity to bending rigidity in polymer glasses," *Journal of Physics: Condensed Matter,* vol. 33, 2021, doi: 10.1088/1361-648X/abfd51.

[120] B. Ruzicka *et al.*, "Evidence of anomalous dispersion of the generalized sound velocity in glasses," *Physical Review B,* vol. 69, no. 10, 2004, doi: 10.1103/PhysRevB.69.100201.

[121] F. Finkemeier and W. von Niessen, "Boson peak in amorphous silicon: A numerical study," *Physical Review B,* vol. 63, no. 23, 2001, doi: 10.1103/PhysRevB.63.235204.

[122] A. I. Chumakov *et al.*, "Role of disorder in the thermodynamics and atomic dynamics of glasses," *Phys Rev Lett,* vol. 112, no. 2, p. 025502, Jan 17 2014, doi: 10.1103/PhysRevLett.112.025502.

[123] G. Baldi, V. M. Giordano, B. Ruta, R. Dal Maschio, A. Fontana, and G. Monaco, "Anharmonic damping of terahertz acoustic waves in a network glass and its effect on the density of vibrational states," *Phys Rev Lett,* vol. 112, no. 12, p. 125502, Mar 28 2014, doi: 10.1103/PhysRevLett.112.125502.

[124] M. B. Garcia, "BOSON PEAK IN TRANSITIONALLY ORDERED AND ORIENTATIONALLY DISORDERED PHASES," Engineering Physics, Tsukuba University, 2020.

[125] A. I. Chumakov *et al.*, "Equivalence of the boson peak in glasses to the transverse acoustic van Hove singularity in crystals," *Phys Rev Lett,* vol. 106, no. 22, p. 225501, Jun 3 2011, doi: 10.1103/PhysRevLett.106.225501.

[126] S. A. Kirillov and S. N. Yannopoulos, "Charge-current contribution to low-frequency Raman scattering from glass-forming ionic liquids," *Physical Review B,* vol. 61, no. 17, pp. 11391-11399, 05/01/ 2000, doi: 10.1103/PhysRevB.61.11391.

[127] D. Tuschel, "Raman Thermometry," *Spectroscopy* vol. 31, no. 12, pp. 8-13, 2016.

[128] S. Sourour and M. Kamal, "Differential scanning calorimetry of epoxy cure: isothermal cure kinetics," *Thermochimica Acta,* vol. 14, no. 1-2, pp. 41-59, 1976.

[129] N. Davidenko, O. García, and R. Sastre, "Photopolymerization kinetics of dimethacrylate-based light-cured dental resins," *Journal of Applied Polymer Science,* vol. 97, no. 3, pp. 1016-1023, 2005, doi: 10.1002/app.21828.

[130] R. Hardis, J. L. P. Jessop, F. E. Peters, and M. R. Kessler, "Cure kinetics characterization and monitoring of an epoxy resin using DSC, Raman spectroscopy, and DEA," *Composites Part A: Applied Science and Manufacturing,* vol. 49, pp. 100-108, 2013, doi: 10.1016/j.compositesa.2013.01.021.

[131] J. Tu, Y. Kashcooli, N. J. Alvarez, and G. R. Palmese, "A practical framework for predicting conversion profiles in vat photopolymerizations," *Additive Manufacturing,* vol. 59, p. 103102, 2022/11/01/ 2022, doi: https://doi.org/10.1016/j.addma.2022.103102.

[132] P. Huang, Y. Lin, Y. Bai, Z. Ni, S. Xie, and B. Dong, "Simultaneous measurement of depth-resolved refractive index field and deformation field inside polymers during the curing process," *Measurement,* vol. 205, p. 112184, 2022/12/01/ 2022, doi: https://doi.org/10.1016/j.measurement.2022.112184.

[133] B. Dong and B. Pan, "Visualizing curing process inside polymers," *Applied Physics Letters,* vol. 116, no. 5, 2020, doi: 10.1063/1.5141827.

[134] A. Cusano, G. Breglio, M. Giordano, A. Calabrò, A. Cutolo, and L. Nicolais, "An optoelectronic sensor for cure monitoring in thermoset-based composites," *Sensors and Actuators A: Physical,* vol. 84, no. 3, pp. 270-275, 2000/09/01/ 2000, doi: https://doi.org/10.1016/S0924-4247(00)00361-7.

[135] M. H. Karami *et al.*, "Curing Kinetics Modeling of Epoxy Modified by Fully Vulcanized Elastomer Nanoparticles Using Rheometry Method," *Molecules,* vol. 27, no. 9, p. 2870, 2022, doi: 10.3390/molecules27092870.

[136] S. K. Romberg and A. P. Kotula, "Simultaneous rheology and cure kinetics dictate thermal post-curing of thermoset composite resins for material extrusion," *Additive Manufacturing,* vol. 71, p. 103589, 2023/06/05/ 2023, doi: https://doi.org/10.1016/j.addma.2023.103589.

[137] Z. Wu, Q. Chen, D. Liu, J. Fan, Q. Zhang, and W. Chen, "In situ monitoring of epoxy resin curing process: Using glass transition as a bridge," *Polymer Testing,* vol. 117, p. 107871, 2023/01/01/ 2023, doi: https://doi.org/10.1016/j.polymertesting.2022.107871.

[138] U. Müller, C. Pretschuh, R. Mitter, and S. Knappe, "Dielectric analysis as a cure monitoring system for UF particle boards," *International Journal of Adhesion and Adhesives,* vol. 73, pp. 45-50, 2017/03/01/ 2017, doi: https://doi.org/10.1016/j.ijadhadh.2016.07.016.

[139] D. G. Lee and H. G. Kim, "Non-Isothermal in Situ Dielectric Cure Monitoring for Thermosetting Matrix Composites," *Journal of Composite Materials,* vol. 38, no. 12, pp. 977-993, 2004/06/01 2004, doi: 10.1177/0021998304040563.

[140] J. Bachmann, E. Gleis, S. Schmölzer, G. Fruhmann, and O. Hinrichsen, "Photo-DSC method for liquid samples used in vat photopolymerization," *Analytica Chimica Acta,* vol. 1153, p. 338268, 2021/04/08/ 2021, doi: https://doi.org/10.1016/j.aca.2021.338268.

[141] T. Chartier *et al.*, "Influence of irradiation parameters on the polymerization of ceramic reactive suspensions for stereolithography," *Journal of the European Ceramic Society,* vol. 37, no. 15, pp. 4431-4436, 2017, doi: 10.1016/j.jeurceramsoc.2017.05.050.

[142] J. Wu *et al.*, "Evolution of material properties during free radical photopolymerization," *Journal of the Mechanics and Physics of Solids,* vol. 112, pp. 25-49, 2018/03/01/ 2018, doi: https://doi.org/10.1016/j.jmps.2017.11.018.

[143] L. H. J. Jeewantha, K. D. C. Emmanuel, H. M. C. M. Herath, J. A. Epaarachchi, M. M. Islam, and J. Leng, "Investigation of curing kinetics and internal strains to enhance performances of bisphenol A based shape memory polymers," *Materialia,* vol. 21, p. 101264, 2022/03/01/ 2022, doi: https://doi.org/10.1016/j.mtla.2021.101264.

[144] T. Ishida *et al.*, "In-situ infrared cure monitoring combined with two-trace two-dimensional (2T2D) correlation analysis to elucidate the matrix–filler interaction of nanocomposites: Case of thermosetting urethane/silica nanospheres," *Polymer Testing,* vol. 112, p. 107587, 2022/08/01/ 2022, doi: https://doi.org/10.1016/j.polymertesting.2022.107587.

[145] A. C. Uzcategui *et al.*, "Microscale Photopatterning of Through-Thickness Modulus in a Monolithic and Functionally Graded 3D-Printed Part," *Small Science,* vol. 1, no. 3, p. 2000017, 2021, doi: 10.1002/smsc.202000017.

[146] Y. Zhang, D. E. Kranbuehl, H. Sautereau, G. Seytre, and J. Dupuy, "Study of UV Cure Kinetics Resulting from a Changing Concentration of Mobile and Trapped Radicals," *Macromolecules,* vol. 41, no. 3, pp. 708-715, 2008/02/01 2008, doi: 10.1021/ma702117e.

[147] A. P. Nowak *et al.*, "Visually and Infrared Transparent Poly(oxalamide) Films with Mechanical Toughness," *ACS Applied Polymer Materials,* vol. 4, no. 7, pp. 5027-5034, 2022, doi: 10.1021/acsapm.2c00571.

[148] E. Matušková, J. Vinklárek, and J. Honzíček, "Effect of Accelerators on the Curing of Unsaturated Polyester Resins: Kinetic Model for Room Temperature Curing," *Industrial & Engineering Chemistry Research,* vol. 60, no. 39, pp. 14143-14153, 2021, doi: 10.1021/acs.iecr.1c02963.

[149] J. C. Bart, E. Gucciardi, and S. Cavallaro, *Biolubricants: science and technology*. Elsevier, 2012.

[150] N. Heigl *et al.*, "Simultaneous Determination of the Micro-, Meso-, and Macropore Size Fractions of Porous Polymers by a Combined Use of Fourier Transform Near-Infrared Diffuse Reflection Spectroscopy and Multivariate Techniques," *Analytical Chemistry,* vol. 80, no. 22, pp. 8493-8500, 2008, doi: 10.1021/ac8013059.

[151] L. Feng and K. Y. S. Ng, "In situ kinetic studies of microemulsion polymerizations of styrene and methyl methacrylate by Raman spectroscopy," *Macromolecules,* vol. 23, no. 4, pp. 1048-1053, 1990, doi: 10.1021/ma00206a023.

[152] B. Martin, J. Puentes, L. Wruck, and T. A. Osswald, "Degree of cure of epoxy/acrylic photopolymers: Characterization with raman spectroscopy and a modified phenomenological model," *Polymer Engineering & Science,* vol. 58, no. 2, pp. 228-237, 2018, doi: 10.1002/pen.24550.

[153] A. P. Kotula, J. W. Woodcock, J. W. Gilman, and G. A. Holmes, "A cure kinetics investigation of amine-cured epoxy by Rheo-Raman spectroscopy," *Polymer,* vol. 278, p. 125967, 2023/06/13/ 2023, doi: https://doi.org/10.1016/j.polymer.2023.125967.

[154] R. V. Chimenti, J. T. Carriere, D. M. D'Ascoli, and J. D. Engelhardt, "Toward a practical method for measuring glass transition in polymers with low-frequency Raman spectroscopy," *Applied Physics Letters,* vol. 122, 26 June 2023 2023, doi: doi: 10.1063/5.0155631.

[155] J. A. Ramos, N. Pagani, C. C. Riccardi, J. Borrajo, S. N. Goyanes, and I. Mondragon, "Cure kinetics and shrinkage model for epoxy-amine systems," *Polymer,* vol. 46, no. 10, pp. 3323-3328, 2005/04/25/ 2005, doi: https://doi.org/10.1016/j.polymer.2005.02.069.

[156] K. M. Hambleton and J. F. Stanzione, "Synthesis and Characterization of a Low-Molecular-Weight Novolac Epoxy Derived from Lignin-Inspired Phenolics," *ACS Omega,* vol. 6, no. 37, pp. 23855-23861, 2021, doi: 10.1021/acsomega.1c02799.

[157] M. C. Celina, N. H. Giron, and A. Quintana, "Cure Chemistry Kinetics in Epoxy Materials," Sandia National Lab.(SNL-NM), Albuquerque, NM (United States), 2015.

[158] R. V. Chimenti *et al.*, "Method for determining resin cure kinetics with low-frequency Raman spectroscopy," *Analyst,* 10.1039/D3AN01099F vol. 148, no. 22, pp. 5698-5706, 2023, doi: 10.1039/D3AN01099F.

[159] A. M. Lehman-Chong, "ADVANCING POLYMER SUSTAINABILITY THROUGH CUSTOM INTERPENETRATING POLYMER NETWORK SYNTHESIS, PROCESSING, AND DESIGN," Doctor of Philosophy Dissertation, Department of Chemical Engineering, Rowan University, 2023.

[160] M. Aldridge, A. Wineman, A. Waas, and J. Kieffer, "In Situ Analysis of the Relationship between Cure Kinetics and the Mechanical Modulus of an Epoxy Resin," *Macromolecules,* vol. 47, no. 23, pp. 8368-8376, 2014/12/09 2014, doi: 10.1021/ma501441c.

[161] S. Saseendran, M. Wysocki, and J. Varna, "Cure-state dependent viscoelastic Poisson's ratio of LY5052 epoxy resin," *Advanced Manufacturing: Polymer & Composites Science,* vol. 3, no. 3, pp. 92-100, 2017/07/03 2017, doi: 10.1080/20550340.2017.1348002.

[162] J. Wang, X. Mu, D. Li, C. Yu, X. Cheng, and N. Dai, "Modeling and Application of Planar-to-3D Structures via Optically Programmed Frontal Photopolymerization," *Advanced Engineering Materials,* vol. 21, no. 5, 2019, doi: 10.1002/adem.201801279.

[163] M. Müller-Pabel, J. A. Rodríguez Agudo, and M. Gude, "Measuring and understanding cure-dependent viscoelastic properties of epoxy resin: A review," *Polymer Testing,* vol. 114, p. 107701, 2022/10/01 2022, doi: https://doi.org/10.1016/j.polymertesting.2022.107701.

[164] S. U. Patil *et al.*, "Simple and convenient mapping of molecular dynamics mechanical property predictions of bisphenol-F epoxy for strain rate, temperature, and degree of cure," *Soft Matter,* 10.1039/D3SM00697B vol. 19, no. 35, pp. 6731-6742, 2023, doi: 10.1039/D3SM00697B.

[165] D. W. Collinson, R. J. Sheridan, M. J. Palmeri, and L. C. Brinson, "Best practices and recommendations for accurate nanomechanical characterization of heterogeneous polymer systems with atomic force microscopy," *Progress in Polymer Science,* vol. 119, p. 101420, 2021/08/01 2021, doi: https://doi.org/10.1016/j.progpolymsci.2021.101420.

[166] H. Gojzewski, B. Imre, C. Check, R. Chartoff, and J. Vancso, "Mechanical mapping and morphology across the length scales unveil structure–property relationships in polycaprolactone based polyurethanes," *Journal of Polymer Science Part B: Polymer Physics,* vol. 54, no. 22, pp. 2298-2310, 2016, doi: https://doi.org/10.1002/polb.24140.

[167] H. Gojzewski, M. Sadej, E. Andrzejewska, and M. Kokowska, "Nanoscale Young's modulus and surface morphology in photocurable polyacrylate/nanosilica composites," *European Polymer Journal,* vol. 88, pp. 205-220, 2017/03/01 2017, doi: https://doi.org/10.1016/j.eurpolymj.2017.01.022.

[168] B. Pittenger, S. Osechinskiy, D. Yablon, and T. Mueller, "Nanoscale DMA with the Atomic Force Microscope: A New Method for Measuring Viscoelastic Properties of Nanostructured Polymer Materials," *JOM,* vol. 71, no. 10, pp. 3390-3398, 2019, doi: 10.1007/s11837-019-03698-z.

[169] H. K. Nguyen *et al.*, "Insights into Mechanical Dynamics of Nanoscale Interfaces in Epoxy Composites Using Nanorheology Atomic Force Microscopy," *ACS Applied Materials & Interfaces,* vol. 15, no. 31, pp. 38029-38038, 2023/08/09 2023, doi: 10.1021/acsami.3c06123.

[170] W. J. Smith, *Modern optical engineering: the design of optical systems*. McGraw-Hill Education, 2008.

[171] R. P. Wool, "Twinkling fractal theory of the glass transition," *Journal of Polymer Science Part B: Polymer Physics,* vol. 46, no. 24, pp. 2765-2778, 2008, doi: 10.1002/polb.21596.

[172] R. P. Wool and A. Campanella, "Twinkling fractal theory of the glass transition: Rate dependence and time-temperature superposition," *Journal of Polymer Science Part B: Polymer Physics,* vol. 47, no. 24, pp. 2578-2590, 2009, doi: 10.1002/polb.21882.

[173] J. F. Stanzione, K. E. Strawhecker, and R. P. Wool, "Observing the twinkling fractal nature of the glass transition," *Journal of Non-Crystalline Solids,* vol. 357, no. 2, pp. 311-319, 2011, doi: 10.1016/j.jnoncrysol.2010.06.041.

[174] I. Noda, A. Dowrey, C. Marcott, G. Story, and Y. Ozaki, "Generalized two-dimensional correlation spectroscopy," *Applied Spectroscopy,* vol. 54, no. 7, pp. 236A-248A, 2000.

[175] N. Fujinuma, B. DeCost, J. Hattrick-Simpers, and S. E. Lofland, "Why big data and compute are not necessarily the path to big materials science," *Communications Materials,* vol. 3, no. 1, p. 59, 2022/08/30 2022, doi: 10.1038/s43246-022-00283-x.

[176] I. Baltog, M. Baibarac, I. Smaranda, and S. Lefrant, "Abnormal anti-Stokes Raman emission as a coherent anti-Stokes Raman scattering-like process in disordered media," *Journal of Physics B: Atomic, Molecular and Optical Physics,* vol. 44, no. 9, p. 095401, 2011, doi: 10.1088/0953-4075/44/9/095401.

[177] T. Goldstein, S.-Y. Chen, J. Tong, D. Xiao, A. Ramasubramaniam, and J. Yan, "Raman scattering and anomalous Stokes–anti-Stokes ratio in MoTe2 atomic layers," *Scientific Reports,* vol. 6, no. 1, p. 28024, 2016, doi: 10.1038/srep28024.

[178] M. Baldovin, S. Iubini, R. Livi, and A. Vulpiani, "Statistical mechanics of systems with negative temperature," *Physics Reports,* vol. 923, pp. 1-50, 2021, doi: 10.1016/j.physrep.2021.03.007.

Appendix

Copyright Permissions

Chapter 2 Text, Figures, & Tables
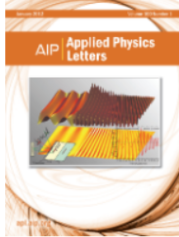
Toward a practical method for measuring glass transition in polymers with low-frequency Raman spectroscopy

Author: Chimenti, Robert V.; Carriere, James T.

Publication: Applied Physics Letters

Publisher: AIP Publishing

Date: Jun 26, 2023

Rights managed by AIP Publishing.

Method for determining resin cure kinetics with low-frequency Raman spectroscopy

R. V. Chimenti, A. M. Lehman-Chong, A. M. Sepcic, J. D. Engelhardt, J. T. Carriere, K. A. Bensley, A. Markashevsky, J. Tu, J. F. Stanzione and S. E. Lofland, *Analyst*, 2023, **148**, 5698 **DOI:** 10.1039/D3AN01099F